CHALMERS
UNIVERSITY OF TECHNOLOGY

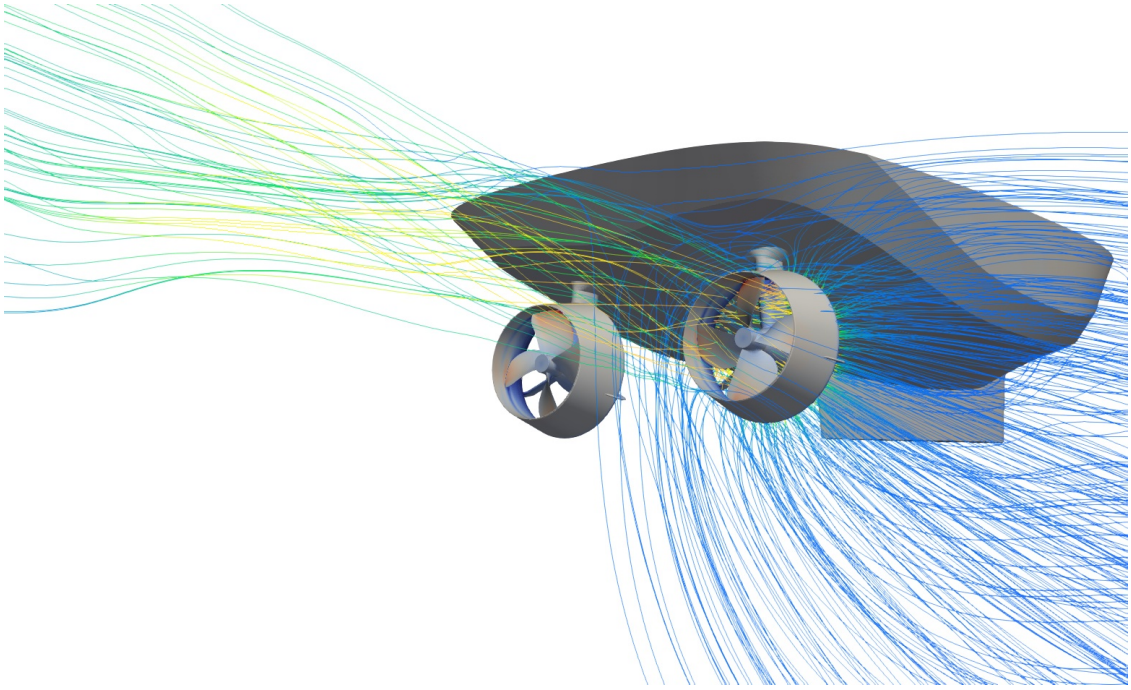

Investigation of Thrust Deduction on Azimuth Thrusters in Bollard Pull Condition using CFD

Master of science thesis in Naval Architecture and Ocean Engineering

FOIVOS LEMONAKIS

Division of Marine Technology
Department of Mechanics and Maritime Sciences
CHALMERS UNIVERSITY OF TECHNOLOGY
Gothenburg, Sweden 2019

MASTER OF SCIENCE THESIS IN
NAVAL ARCHITECTURE AND OCEAN ENGINEERING

Investigation of Thrust Deduction on Azimuth Thrusters in Bollard Pull Condition using CFD

FOIVOS LEMONAKIS

CHALMERS
UNIVERSITY OF TECHNOLOGY

Division of Marine Technology
Department of Mechanics and Maritime Sciences
Chalmers University of Technology
Gothenburg, Sweden 2019

Investigation of Thrust Deduction on Azimuth Thrusters in Bollard Pull Condition using CFD

Examiner: Rickard Bensow, Chalmers University of Technology
Supervisors: Tobias Huuva, Caterpillar Propulsion AB
Simon Törnros, Caterpillar Propulsion AB

Report No.: 2019:28
Department of Mechanics and Maritime Sciences
Division of Marine Technology
Chalmers University of Technology
SE-412 96 Gothenburg
Telephone +46 31 772 1000

Cover: Visualization constructed in ParaView v.5.6.0 of the pressure distribution acting on a ducted azimuth thruster and a harbour tug boat, along with the streamlines of the magnitude of the velocity vector field.
©

Typeset in LaTeX
Printed by Chalmers Reproservice
Gothenburg, Sweden 2019

Investigation of Thrust Deduction on Azimuth Thrusters in Bollard Pull Condition using CFD

FOIVOS LEMONAKIS
Department of Mechanics and Maritime Sciences
Chalmers University of Technology

Abstract

This report is result of a master's thesis project performed together with *Caterpillar Propulsion AB*, which is a revisit of an older master's thesis with title "Hydrodynamics of Conventional Propeller and Azimuth Thruster in Behind Condition" (Matin, 2011). In the previous master's thesis, the thrust deduction factors of open shaft propellers and ducted azimuth thrusters, installed on an offshore vessel, are studied. However, during the recent years the ducted azimuth thrusters have become more and more common and especially for vessels such as tug boats, drilling vessels etc. For such vessels, the bollard pull condition is really important, which indicates high power operation with high loading (Funeno, 2009). Thus, the purpose of the current master's thesis is the investigation of thrust deduction on ducted azimuth thrusters in bollard pull condition using Computational Fluid Dynamics (CFD).

In order achieve this type of study, a harbour tug boat with twin ducted azimuth thrusters and a combination of steady state Multiple Reference Frame (MRF) and transient Sliding Mesh Interface (SMI) modelling methodologies have been used. MRF has been proven to be inaccurate in behind condition and at low or high advance coefficients, as it usually results in relatively strange flow fields in the vicinity of the propeller while SMI has shown higher accuracy. However, SMI is a much more computationally demanding methodology (Gullberg & Sengupta, 2011). Thus, SMI has been used for critical regions and MRF for regions of lower interest.

Outcome of this study is that during the bollard pull condition the contribution of the nozzle is higher than the propeller in terms of thrust and the contribution of the gear case housing is higher than the hull in terms of resistance. The highest thrust deduction appears on the gear case housing with 8.92% while the highest merit deduction, which shows a lower performance, appears when placing the whole propulsion unit behind the hull with 9.09%. Furthermore, the measured bollard pull force of the open water case is about 8.23% higher than the one of the Wageningen CD Series. However, this high difference is not realistic and the reason has to be identified. Finally, by comparing the MRF and SMI methodologies, it is concluded that the MRF approach gives appropriate results for initialization and quite reasonable results for medium advance coefficients at low computational cost while the SMI approach is needed for the critical regions of low and high advance coefficients.

Keywords: Propulsion, Hydrodynamics, Thruster, Thrust deduction, Bollard pull, CFD, Multiple Reference Frame (MRF), Sliding Mesh Interface (SMI).

Acknowledgements

This master's thesis is part of the Naval Architecture and Ocean Engineering master's programme, which is part of the Department of Mechanics and Maritime Sciences, Chalmers University of Technology.

The author of this thesis would like to thank and acknowledge the help and contribution of the following:

- Professor Rickard E. Bensow, examiner of this master's thesis and Head of Research in Hydrodynamics at the Department of Mechanics and Maritime Sciences at Chalmers University of Technology.
- Caterpillar Propulsion AB for providing the resources of this study project.
- Tobias Huuva, supervisor of this master's thesis and Engineering Manager at the Department of Hydrodynamics at Caterpillar Propulsion AB.
- Simon Törnros, supervisor of this master's thesis and Hydrodynamics Specialist at the Department of Hydrodynamics at Caterpillar Propulsion AB.
- Family and friends for their support during the two intensive years of this master's programme.

Foivos Lemonakis, Gothenburg, June 2019

Contents

List of Abbreviations

Abbreviation	Description
2D	Two-Dimensional space
3D	Three-Dimensional space
AHTS	Anchor Handling/Tug/Supply
AMI	Arbitrary Mesh Interpolation
CAD	Computer Aided Design
CAE	Computer Aided Engineering
CFD	Computational Fluid Dynamics
DNS	Direct Numerical Simulation
EAR	Expanded Area Ratio
FPP	Fixed Pitch Propeller
HPC	High-Performance Computing
LES	Large Eddy Simulation
MRF	Multiple Reference Frame
PIMPLE	Pressure-Implicit Method for Pressure-Linked Equation
PISO	Pressure-Implicit with Splitting of Operators
QUICK	Quadratic Upstream Interpolation for Convective Kinematics
RANS	Reynolds-Averaged Navier Stokes
RPM	Revolutions Per Minute
RSM	Reynolds Stress equation Model
SIMPLE	Semi-Implicit Method for Pressure-Linked Equations
SIMPLEC	Semi-Implicit Method for Pressure Linked Equations - Consistent
SIMPLER	Semi-Implicit Method for Pressure-Linked Equations - Revised
SMI	Sliding Mesh Interface
SST	Shear Stress Transport
TDMA	Tri-Diagonal Matrix Algorithm

List of Variables

Variable	[Units]	Description
D	m	diameter
$D_e, D_w, D_n, D_s, D_t, D_b$		diffusion terms of the east, west, north, south, top, bottom faces in finite volume theory
dm	kg	mass of the element
dV	m^3	infinitesimal fluid element
e, w, n, s, t, b		east, west, north, south, top, bottom faces of the control volume in finite volume theory
$E(\kappa)$	m^3/s^2	spectral energy content of the large eddies in turbulence modelling
En	$-$	Euler number
F	N	force
$\overrightarrow{F}$	N	force vector derived from the total force acting on the volume element in finite volume theory
$\overline{F}$	N	mean force
$F_e, F_w, F_n, F_s, F_t, F_b$		convection terms of the east, west, north, south, top, bottom faces in finite volume theory
Fn	$-$	Froude number
g	m/s^2	acceleration of gravity
J	$-$	advance coefficient
k	m^2/s^2	turbulent kinetic energy in turbulence modelling
K_Q	$-$	non-dimensional torque coefficient, torque coefficient in behind condition
$\overline{K_Q}$	$-$	mean torque coefficient
K_{Q_o}	$-$	torque coefficient in open water condition
k_s	μm	surface roughness
K_T	$-$	non-dimensional thrust coefficient
$\overline{K_T}$	$-$	mean thrust coefficient
$K_{T,net}$	$-$	net sum of all the thrust coefficients
K_{Tn}	$-$	nozzle thrust coefficient
K_{Tp}	$-$	propeller thrust coefficient
$K_{T,R}$	$-$	sum of the thrust coefficients that are derived from the resistance components
$K_{T,T}$	$-$	sum of the thrust coefficients that are derived from the thrust components
L	m	reference length (i.e., characteristic linear dimension) that describes the travelled length of the fluid, obstacle width
ℓ	m	characteristic length of the larger scales in turbulence modelling
M	$N \cdot m$	moment
$\overline{M}$	$N \cdot m$	mean moment

Variable	[Units]	Description
m_c	$-$	merit coefficient
$m_{c,deduct}$	%	merit deduction
n	rpm	rotational speed
p	Pa	pressure, instantaneous pressure in turbulence modelling
P	Pa	steady mean value of the pressure component
P, E, W, N, S, T, B		central nodal point of the control volume and the east, west, north, south, top, bottom central nodal points of the neighboring volumes in finite volume theory
p'	Pa	fluctuating pressure component in turbulence modelling
P_B	W	brake power of main engine
p_d	Pa	downstream pressure
P_D	W	delivered power to the propeller via the shaft
p_{hd}	Pa	hydrodynamic pressure
p_u	Pa	upstream pressure
Q	$\mathrm{N \cdot m}$	torque
$\overline{Q}$	$\mathrm{N \cdot m}$	mean torque
R	N	resistance
$\overline{R}$	N	mean resistance
Rn	$-$	Reynolds number
Rn_{crit}	$-$	critical Reynolds number
S_M	$\mathrm{N/m^3}$	momentum source term
T	$^\circ\mathrm{C}, \mathrm{N}$	temperature, thrust
t	$\mathrm{s}, \mathrm{s}, \%$	time, characteristic time of the larger scales in turbulence modelling, thrust deduction fraction
$\overline{T}$	N	mean thrust
T_{BP}	ton	bollard pull force
$T_{BP,1995kw,CD}$	ton	bollard pull force at a fixed delivered power obtained from the Wageningen CD Series
$T_{BP,1995kw,CFD}$	ton	bollard pull force at a fixed delivered power obtained from CFD results
T_{net}	N	net sum of the total thrust
$T_{net,deduct}$	N	deduction of the net sum of the total thrust
T_p	N	propeller thrust
T_{tot}	N	total thrust of a vessel that operates in full power
U_∞	m/s	reference velocity, steady mean value of the velocity component in turbulence modelling
u	m/s	characteristic velocity of the Kolmogorov microscales in turbulence modelling
u, v, w	m/s	scalars representing the velocity in x, y and z-directions, instantaneous velocities in x, y and z-directions in turbulence modelling

Variable	[Units]	Description
$\overrightarrow{u}, \overrightarrow{v}, \overrightarrow{w}$	m/s	velocity vectors in x, y and z-directions
u'	m/s	fluctuating velocity component in turbulence modelling
u^+	−	non-dimensional velocity
u_τ	m/s	friction velocity
V_A	m/s	advance velocity
V_S	m/s	ship velocity
Wn	−	Weber number
w_T	−	effective Taylor's wake fraction
x, y, z	m, −	components of a vector in the x, y or z-directions, coordinates of global system
$\bar{x}, \bar{y}, \bar{z}, \bar{\zeta}, \bar{u}, \bar{v}, \bar{w}, \bar{p}, \bar{t}$	−	non-dimensional quantities in similarity equations
y^+	−	non-dimensional distance from the wall
z	m	distance of the upper part of the nozzle and the water surface
Z	−	number of blades
$\overrightarrow{\alpha}$	m/s^2	acceleration vector
Γ		generalized diffusion coefficient
γ	N/m	surface tension or over-speed ratio in channel
δ	m	boundary layer thickness
$\delta_{x_{WP}}$	m	distance between the nodes W and P in finite volume theory
ΔR	N	increase of the resistance
ε	m^2/s^3	dissipation rate of turbulent kinetic energy
ζ	m	wave elevation
η	m	characteristic length of the Kolmogorov microscales in turbulence modelling
η_0	−	open water efficiency
$\overline{\eta_0}$	−	mean open water efficiency
η_D	−	total propulsive efficiency
η_H	−	hull efficiency
η_R	−	relative rotative efficiency
η_S	−	shaft efficiency
ϑ	m/s	characteristic velocity of the larger scales in turbulence modelling
κ	1/m	wave number
μ	Pa · s	dynamic viscosity of the fluid
ν	m^2/s	kinematic viscosity of the fluid
ν_t	m^2/s	turbulent viscosity field
π	−	mathematical constant
ρ	kg/m^3	density
τ	Pa, s	shear stress, characteristic time of the Kolmogorov microscales in turbulence modelling
τ_w	Pa	wall shear stress
$\tau_{xx}, \tau_{yy}, \tau_{zz}$	Pa	Reynolds normal stresses in RANS equations

Variable	[Units]	Description
$\tau_{xy}, \tau_{yx}, \tau_{xz}, \tau_{zx}, \tau_{yz}, \tau_{zy}$	Pa	Reynolds shear stresses in RANS equations
ϕ	–	flow property in finite volume theory
ω	1/s	specific dissipation rate of turbulent energy in turbulence modelling

List of Figures

List of Tables

1
Introduction

In this chapter, a background of the propulsion systems; the propellers; the driving reasons of the continuous development; and finally the computational fluid dynamics is presented. In the rest of the chapter, it is described how this thesis contributes to the field by explaining the purpose, the importance and the scope of this topic.

1.1 Background

Transportation through the water is one of the oldest means of transport during humankind. Ships and boats are used for many different purposes such as trade, fishing, defense and leisure. Therefore, the need of some kind of propulsion system was already created since the ancient years of the stone age. For thousands of years, the oars were the main and probably the only type of propulsion while during the 7th century the sails were introduced. During the 16th century the number of propulsion systems were limited and the use of sails was at its peak. At the end of the 18th century the Industrial Revolution arrived, which brought a new era for the shipping industry as well as for many other industries. In the beginning of the 19th century, paddle wheels were the prevailing propulsion system for steam vessels while at the same time the screw propeller got invented, which was based on the Archimedes' screw.

Since then, propellers are the predominant marine propulsion system, which convert rotational motion into thrust power. A pressure difference is generated between the pressure side and the suction side of the propeller blades and as a result the fluid, which in this specific case is water, is accelerated and the vessel moves. The propulsion of a vessel though is not any more the main goal as this is already solved. However, there is a continuous development of the marine propulsion systems, which is mainly driven by the need of higher efficiency; both for environmental and economical reasons, noise reduction due to noise pollution and comfort reasons, operating security, safe performance and maneuverability. In order to achieve those, the understanding of the physical phenomena around the propulsion unit and the hull of the ship is vital. Hydrodynamics is the subject that is studying the flow of water and the forces applied on structures immersed in water.

An important tool for the study of hydrodynamic phenomena and designs is Computational Fluid Dynamics (CFD), which is the numerical analysis of fluid flow, heat transfer and associated phenomena such as chemical reactions. The methodology of

this kind of analysis is mostly used to run computer-based simulations by the use of computer software packages in order to aid various engineering tasks, something that makes CFD a part of the Computer Aided Engineering (CAE). CFD starts from the 1960s where the aerospace industry developed CFD techniques and integrated them into the design while from the 1990s a wider industrial usage starts (Versteeg & Malalasekera, 2007).

1.2 Importance of this topic

This report is result of a master's thesis project performed together with *Caterpillar Propulsion AB*, which is a revisit of an older master's thesis at Chalmers with title "Hydrodynamics of Conventional Propeller and Azimuth Thruster in Behind Condition" (Matin, 2011). In the previous master's thesis the thrust deduction factors of open shaft propellers and ducted azimuth thrusters, installed on an offshore vessel, are studied. However, during recent years the ducted azimuth thrusters have become a more and more common propulsion system on vessels such as harbour tug boats, Anchor Handling/Tug/Supply (AHTS) vessels, cable laying vessels, oceanographic research vessels and drilling vessels due to their good manoeuvrability. For such vessels, the bollard pull operating condition is really important, which indicates high power operation with high loading (Funeno, 2009). However, the performance of the azimuth thrusters is still questionable since they haven't been studied as much as the open shaft propulsion units. Moreover, model testing of azimuth thrusters is not that efficient due to the high viscous effects at model scale while the conventional open shaft thrusters have been validated with a huge amount of model tests by several research institutes.

1.3 Purpose

The purpose of the current thesis is the investigation of thrust deduction on ducted azimuth thrusters in bollard pull condition and in full-scale using CFD, in order to develop a better understanding of the physical phenomena around this type of geometry, understand where losses occur as well as understand which parts of those geometries are beneficial. In order to fulfil this purpose, there is the need to investigate the hydrodynamic interaction between the propeller, the nozzle, the gear case housing and the hull.

1.4 Scope

In order perform this type of study, a harbour tug boat with twin ducted azimuth thrusters and a combination of steady state Multiple Reference Frame (MRF) and transient Sliding Mesh Interface (SMI) modelling methodologies have been used. Steady state MRF has been proven to be inaccurate in behind condition and at

low or high advance coefficients, as it usually results in relatively strange flow fields in the vicinity of the propeller while transient SMI has shown higher accuracy. However, transient SMI is a much more expensive methodology in terms of computational cost (Gullberg & Sengupta, 2011). Thus, transient SMI has been used for critical regions such as for advance coefficients $J = 0.00$, that indicate bollard pull condition, and steady state MRF for regions of lower interest. Finally, a comparison with the Wageningen CD Series is done in order to develop an evaluation tool which can be used in the future in order to evaluate the early stages of a project.

1.4.1 Investigation cases

As already mentioned, the hydrodynamic interactions between the propeller, the nozzle, the gear case housing and the hull need to be investigated. Thus, CFD simulations of the following cases are carried out and investigated separately:

- The propeller and the nozzle in open water condition,
- The propeller, the nozzle and the gear case housing in open water condition,
- The propeller, the nozzle, the gear case housing and the hull in behind condition.

Note: The gear case housing is considered to be part of the propulsion unit and not part of the hull.

1.4.2 Software packages used

In order to solve the fluid flow problems with CFD, there is need of three main steps: pre-processing, solving and post-processing. The software packages that are used within this project in order to achieve these three steps are the following:

Pre-processor:	**Definition of the geometry and mesh generation** ANSA Pre-processor v.19.0.1 Developed by 'BETA CAE Systems S.A.'
Solver:	**Solving of the governing equations** OpenFOAM v1806 Open source software developed by 'OpenCFD Ltd'
Post-processors:	**Visualization of the simulation results** ParaView v.5.6.0 Open source software developed mainly by 'Kitware Inc.' and 'Los Alamos National Laboratory'

Process of the numerical results
MATLAB R2018b
Developed by 'The MathWorks, Inc.'

Comparison with the Wageningen CD Series
Microsoft Excel propCalcCD2.3.1 tool
Developed by 'Caterpillar Propulsion AB'

Rendering: **3D visualization of the geometry**
Blender 2.79
Open source software supported by 'Blender Foundation'

2

Theory

In this chapter, a thorough explanation of the background theory of this thesis is presented. The first sections of this chapter demonstrate a fundamental theory of CFD, governing equations, similarity between model and full-scale, propeller scaling, types of fluid flow and turbulence modelling. Thus, these sections could be skipped from a reader with basic knowledge in these topics. On the contrary, the last sections of this chapter indicate a more specific theory of open water characteristics, propulsive factors, bollard pull condition and modelling methodologies, which is directly related to the current study.

2.1 Introduction to Computational Fluid Dynamics

As mentioned before, CFD is the numerical analysis of fluid flow, heat transfer and associated phenomena such as chemical reactions around a system. In order to perform such an analysis, computer-based simulations by the use of a computer software are mainly used.

CFD codes and software packages are using numerical algorithms in order to solve fluid flow problems. All commercial CFD packages include input problem parameters and most of them also include tools for analyzing the results. Thus, all CFD packages include three main steps (Versteeg & Malalasekera, 2007):

- **Pre-processing**, which includes the input problem parameters and the conversion of the inputs into a form that the solver can use. Pre-processing can be divided into:
  - Definition of the computational domain
  - Grid generation
  - Identification of the physical and chemical phenomena that need to be modelled
  - Definition of the fluid properties
  - Definition of the boundary conditions
- **Solving** can be divided into various categories according to the numerical techniques that are being used. However, the finite volume method is the most widely used method among most of the CFD codes. Solving can be divided into:
  - Integration of the governing equations of the flow over the finite control volumes of the domain

  - Discretisation of the integrated equations into algebraic equations
  - Solving of the algebraic equations by the use of an iterative method
- **Post-processing**, which includes the visualization of the domain geometry, the mesh that is used in order to solve the algebraic equations and the simulation results as well as the process of the numerical results. Post-processing can be divided into:
  - Visualization of the simulation results
  - Process of the numerical results

In the following sections, the already mentioned main steps of CFD and their subcategories are presented in the same order as above.

2.1.1 Definition of the computational domain

A domain can be divided into an inner domain (i.e. geometries of interest) and outer domain (i.e. boundaries). The definition of the outer computational domain is dependent on each case and it has to be of a size to be able to provide results with precision while it should not be much bigger than needed so the simulation becomes too expensive.

2.1.2 Grid generation

The solving of the algebraic equations in order to determine flow variables such as velocity, pressure and temperature is defined at nodes inside each cell of the grid. Hence, the accuracy of a CFD problem is highly dependent on the number of cells with a higher number of cells giving higher accuracy. However, the higher the number of cells of a grid, the more expensive a simulation becomes in terms of computer hardware and calculation time. Thus, an optimal number of cells should be chosen without compromising the accuracy of the result. In order to achieve that, non-uniform meshes are widely used which imply finer mesh in areas where large geometrical or flow variations occur and coarser mesh in areas with smaller geometrical or flow variations. However, the quality of the mesh is really important, which implies elements with as simple geometries as possible. Thus, most of the commercial mesh generation software packages include mesh quality checks as well as automatic and manual correction mesh quality tools.

2.1.3 Identification of the physical and chemical phenomena that need to be modelled

Prior to a CFD simulation, the definition of the flow problem in terms of the physical and chemical phenomena is needed. The most usual decisions in order to define a flow problem follow:

- Model a problem in two-dimensional space (2D) or three-dimensional space (3D).
- Include or exclude the density variations due to ambient temperature or pressure variations.

- Treatment of the small-scale turbulence.

Always within CFD, many assumptions are made in order to simplify complex flow problems. However, it is really important to be always aware of all the assumptions that are made.

2.1.4 Definition of the fluid properties

All the fluid properties such as the density ρ, pressure p, velocity u and temperature T need to be defined. It should be mentioned that all the fluid properties are functions of space and time. Thus, those properties should be defined respectively as $\rho(x, y, z, t)$, $p(x, y, z, t)$, $u(x, y, z, t)$ and $T(x, y, z, t)$.

2.1.5 Definition of the boundary conditions

CFD problems are characterized by boundary conditions. The boundary conditions represent a condition that needs to be satisfied within the boundary region. Those boundary conditions enter a discretised system, either implicitly in the coefficient matrix or explicitly in the source term. The most common boundary conditions, within which a set of differential conditions are solved, are the following:

- Inlet
- Outlet
- Wall
- Symmetry
- Periodic/cyclic
- Prescribed pressure

2.1.6 Integration of the governing equations of the flow over the finite control volumes of the domain

Initial step of the solving part is the integration of the governing equations of the flow from face to face and over the finite control volumes of the domain in order to obtain a flow property ϕ at its nodal point P. During this step the conservation of various flow properties within each control volume is achieved by relating the numerical algorithm with the physical conservation principles. Within the finite control volume (see *Figure 2.1*) the conservation of a flow variable ϕ, such as velocity, pressure, temperature and density, needs to be fulfilled. Thus, this conservation can be expressed as a balance of a system (Versteeg & Malalasekera, 2007):

Rate of change of ϕ in the control volume with respect to time.	=	Net rate of increase of ϕ due to **convection** into the control volume.	+	Net rate of increase of ϕ due to **diffusion** into the control volume.	+	Net rate of **creation** of ϕ inside the control volume.

The integration of the governing equations of the flow over the finite control volumes is more thoroughly presented in Sections 2.2 and 2.3.

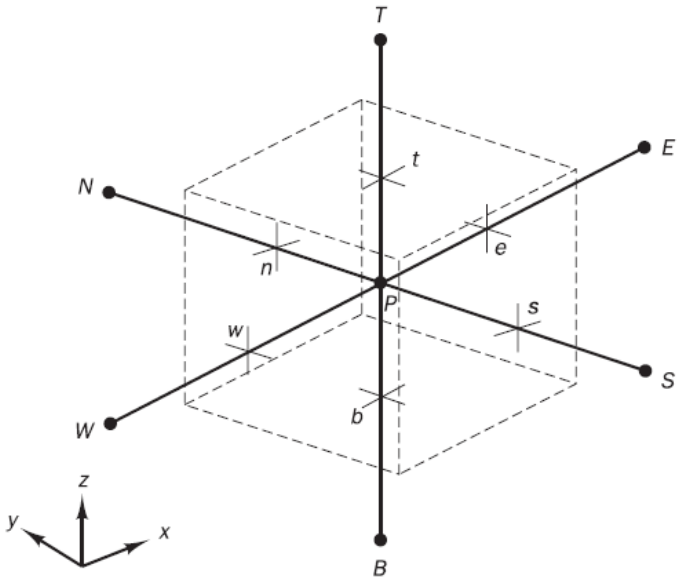

Figure 2.1: A finite control volume (cell) and its neighbouring nodes (Versteeg & Malalasekera, 2007).

2.1.7 Discretisation of the integrated equations into algebraic equations

The integrated governing equations need to be discretised (i.e. to go from a continuous differential equation to an algebraic discrete equation) in order to capture the transport phenomena, the source terms and the rate of change with respect to time. In order to do that, coefficients and gradients at the faces need to be calculated (Versteeg & Malalasekera, 2007). Gradients at the faces are approximated by calculating the distribution of the properties between two nodal points by the use of **discretisation schemes** such as Gaussian integration and **interpolation schemes** such as Central differencing, Upwind, Hybrid, Quadratic Upstream Interpolation for Convective Kinematics (QUICK) . In a similar way, divergence and time derivative terms at the faces are approximated by the use of discretisation and interpolation schemes (OpenCFD Ltd, 2018).

The transport phenomena include the convection part, which is the transport due to fluid flow, and the diffusion part, which is the transport due to variations of the flow variable ϕ from node to node (i.e. net movement from regions with high-concentration to regions with low-concentration). An example of a grid in 2D and its nodes (i.e. E, W, N, S) are presented in the following figure.

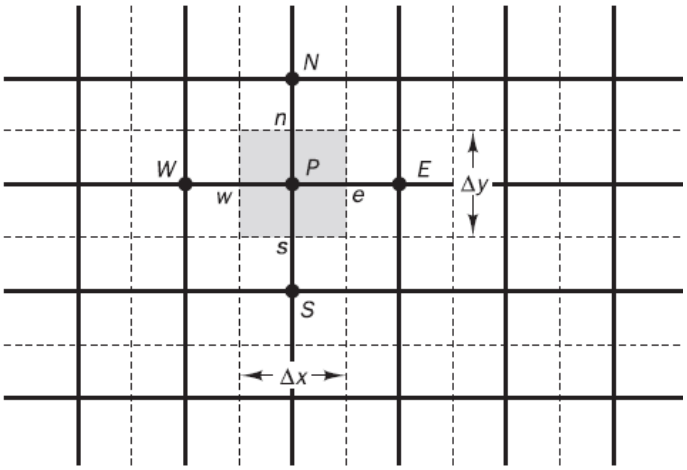

Figure 2.2: Part of the grid presented in 2D (Versteeg & Malalasekera, 2007).

Schemes can generally be split into different **orders of accuracy**. Schemes with lower order of accuracy have higher stability of the results with less accuracy (due to the high level of diffusion error). On the other hand, schemes with higher order of accuracy have lower stability (due to false oscillations when the Peclet number is high) with more accuracy. Peclet number is evaluated at the face of the control volume and is defined as follows (i.e. assuming a west face):

$$Pe_w = \frac{F_w}{D_w} = \frac{(\rho U)_w}{\Gamma/\delta_{x_{WP}}} \tag{2.1}$$

where:
F_w is the convection term of the west face,
D_w is the diffusion term of the west face,
Γ is the generalized diffusion coefficient,
$\delta_{x_{WP}}$ is the distance between the nodes W and P.

Thus, sometimes hybrid schemes can be ideal since they combine a wider range of problems (i.e. diffusion or convection dominated problems). Such an example is the hybrid differencing scheme which employs:

- Central differencing scheme (2nd order accurate) for Peclet numbers $Pe < 2$
- Upwind scheme (1st order accurate) by taking into account only the transportiveness (i.e. upwind for convection and setting the diffusion to zero) for Peclet numbers $Pe \geq 2$

Finally, the evaluation of the order of accuracy of a discretisation is done by the use of Taylor expansion.

2.1.8 Solving of the algebraic equations by the use of iterative method

Final step of the solving part is the iterative solving of the algebraic equations by the use of mathematical algorithms in order to establish a correct relationship between velocity and pressure. The governing equations are often solved separately and the continuity equation is rearranged in order to achieve a better solution, hence the use of some mathematical algorithms is needed. Examples of such mathematical algorithms are (Versteeg & Malalasekera, 2007):

- Semi-Implicit Method for Pressure-Linked Equations (SIMPLE)
- Semi-Implicit Method for Pressure Linked Equations - Consistent (SIMPLEC)
- Semi-Implicit Method for Pressure-Linked Equations - Revised (SIMPLER)
- Pressure-Implicit with Splitting of Operators (PISO)
- Pressure-Implicit Method for Pressure-Linked Equations (PIMPLE)

The mathematical algorithms are using point-iterative methods for computing points of iterated functions where a linear system of algebraic equations is solved (i.e. $Ax = b$ with unknown the x). Examples of such iterative linear solvers are:

- Gauss-Seidel
- Tri-Diagonal Matrix Algorithm (TDMA)

2.1.9 Visualization of the simulation results

There are many ways to process and present the simulation results. Usually, the domain geometry and its mesh is displayed through commercial software packages while various flow variables ϕ such as velocity u, pressure p, temperature T and density ρ, as well as turbulent quantities are also displayed around this domain geometry and within this mesh. Moreover, vector plots and 2D or 3D surface plots are used to present the convergence and residuals as well as a flow variable ϕ that may be of interest. All these tools are helping to get a better understanding of the simulation results in order to be able to yield to a conclusion.

2.1.10 Process of the numerical results

Even though the visualization of the results gives a really good understanding of the quality of the results and helps to draw conclusions, it is still really important to process the specific quantities that are important for the specific study. Thus, a series of calculations is needed in order to complete the whole picture with the numerical conclusions.

2.2 Governing equations

Changes in the mass, momentum and energy of a fluid due to the appearance of a source or multiple sources within the fluid element and during a flow along the boundaries lead to the fluid flow and heat transfer equations that govern the whole system. The governing equations of the conservative or divergence form of the

time-dependent 3D viscous flow of a Newtonian fluid are presented in the following sections. However, since the fluid is considered incompressible, which indicates that the density ρ is constant within the volume and through time, some rearrangements and simplifications are made.

2.2.1 The continuity equation

The continuity equation, also known as mass conservation, is derived from the volume, which is the infinitesimal fluid element dV, as shown in *Figure 2.3*. The net transport of mass out of the element should be zero in the case where there is not any mass source. Thus, the continuity equation is formed as:

$$\frac{\partial \rho}{\partial t} + div(\rho u) = 0 \tag{2.2}$$

which can also be written as:

$$\frac{\partial \rho}{\partial t} + \frac{\partial}{\partial x}\rho u \cdot dV + \frac{\partial}{\partial y}\rho v \cdot dV + \frac{\partial}{\partial z}\rho w \cdot dV = 0 \tag{2.3}$$

where:
$dV = dx \cdot dy \cdot dz$,
u is a scalar representing the velocity in x-direction,
v is a scalar representing the velocity in y-direction,
w is a scalar representing the velocity in z-direction.

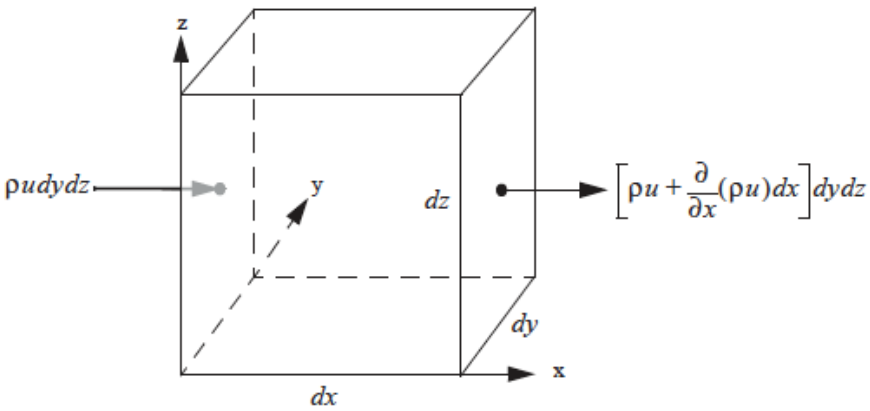

Figure 2.3: Mass flow in x-direction through the fluid element (Larsson & Raven, 2010).

However, since the fluid is considered as incompressible, the continuity equation can be re-written as:

$$\frac{\partial u}{\partial x} + \frac{\partial v}{\partial y} + \frac{\partial w}{\partial z} = 0 \tag{2.4}$$

2.2.2 The Navier-Stokes equations

The Navier-Stokes equations are derived through a long derivation by applying Newton's second law to the infinitesimal fluid element dV (Larsson & Raven, 2010):

$$d\overrightarrow{F} = dm \cdot \overrightarrow{\alpha} \tag{2.5}$$

where:
$\overrightarrow{F}$ is the force vector derived from the total force acting on the element (i.e. arrow represents vector),
dm is the mass of the element,
$\overrightarrow{\alpha}$ is the acceleration vector.

After the long derivation, the Navier-Stokes equations for incompressible flow are obtained, assuming that the gravity g is the only body force along the z-axis (Versteeg & Malalasekera, 2007):

x-momentum:

$$\frac{\partial(\rho u)}{\partial t} + div(\rho u u) = -\frac{\partial p}{\partial x} + div(\mu \text{ grad } u) + S_{Mx} \tag{2.6}$$

$$\rho\left(\frac{\partial u}{\partial t} + u\frac{\partial u}{\partial x} + v\frac{\partial u}{\partial y} + w\frac{\partial u}{\partial z}\right) = -\frac{\partial p}{\partial x} + \mu\left(\frac{\partial^2 u}{\partial x^2} + \frac{\partial^2 u}{\partial y^2} + \frac{\partial^2 u}{\partial z^2}\right) + S_{Mx}$$

Dividing by ρ, the following equation is obtained (Larsson & Raven, 2010):

$$\frac{\partial u}{\partial t} + u\frac{\partial u}{\partial x} + v\frac{\partial u}{\partial y} + w\frac{\partial u}{\partial z} = -\frac{1}{\rho}\frac{\partial p}{\partial x} + \nu\left(\frac{\partial^2 u}{\partial x^2} + \frac{\partial^2 u}{\partial y^2} + \frac{\partial^2 u}{\partial z^2}\right) + \frac{1}{\rho}S_{Mx} \tag{2.7}$$

In a similar way, the equations for the other two directions are obtained as follows:

y-momentum:

$$\frac{\partial v}{\partial t} + u\frac{\partial v}{\partial x} + v\frac{\partial v}{\partial y} + w\frac{\partial v}{\partial z} = -\frac{1}{\rho}\frac{\partial p}{\partial y} + \nu\left(\frac{\partial^2 v}{\partial x^2} + \frac{\partial^2 v}{\partial y^2} + \frac{\partial^2 v}{\partial z^2}\right) + \frac{1}{\rho}S_{My} \tag{2.8}$$

z-momentum:

$$\frac{\partial w}{\partial t} + u\frac{\partial w}{\partial x} + v\frac{\partial w}{\partial y} + w\frac{\partial w}{\partial z} = -\frac{1}{\rho}\frac{\partial p}{\partial z} + \nu\left(\frac{\partial^2 w}{\partial x^2} + \frac{\partial^2 w}{\partial y^2} + \frac{\partial^2 w}{\partial z^2}\right) + \frac{1}{\rho}S_{Mz} - g \tag{2.9}$$

where:
g is the gravity in z-direction,
S_M is the momentum source term.

By looking at *Eq.*(2.7), (2.8) and (2.9), the left-hand side of these equations represents the acceleration of the fluid element in the x, y and z-directions respectively, thus the convection terms. The right-hand side represents the forces due to pressure (i.e. pressure gradient), viscous (i.e. diffusion terms) and body (i.e. gravity).

2.3 Similarity between model and full-scale

When carrying out model tests, it should be kept in mind to keep some similarities to the full-scale. Those similarities can be divided into: geometric, which include the shape and roughness (i.e. roughness is included in the viscous resistance); kinematic, which means that all the velocities are scaled; and dynamic, which means that all the forces of the flow are scaled (Larsson & Raven, 2010).

In order to apply the similarity laws between the model and full-scale, the governing equations and the boundary conditions need to be independent of dimension. Thus, the following dimensionless quantities are introduced:

$$\bar{x} = \frac{x}{L}, \qquad \bar{y} = \frac{y}{L}, \qquad \bar{z} = \frac{z}{L}, \qquad \bar{\zeta} = \frac{\zeta}{L}$$

$$\bar{u} = \frac{u}{U_\infty}, \qquad \bar{v} = \frac{v}{U_\infty}, \qquad \bar{w} = \frac{w}{U_\infty}, \qquad \bar{p} = \frac{p_{hd}}{\rho U_\infty^2}, \qquad \bar{t} = \frac{tU_\infty}{L}$$

where:
x, y, z are components of a vector in the x, y or z-directions,
ζ is the wave elevation,
L is the reference length (i.e. characteristic linear dimension) that describes the travelled length of the fluid,
U_∞ is the reference velocity,
p_{hd} is the hydrodynamic pressure,
t is the time.

By introducing these dimensionless quantities into the governing equations, which are the continuity equation (see *Eq.*(2.4)) and the Navier-Stokes equations (see *Eq.*(2.7), (2.8) & (2.9)), the equations below are obtained.

2.3.1 The continuity equation

$$\frac{\partial(\bar{u}U_\infty)}{\partial(\bar{x}L)} + \frac{\partial(\bar{v}U_\infty)}{\partial(\bar{y}L)} + \frac{\partial(\bar{w}U_\infty)}{\partial(\bar{z}L)} = 0 \tag{2.10}$$

By dividing this equation by $\frac{U_\infty}{L}$, the following equation is obtained:

$$\frac{\partial\bar{u}}{\partial\bar{x}} + \frac{\partial\bar{v}}{\partial\bar{y}} + \frac{\partial\bar{w}}{\partial\bar{z}} = 0 \tag{2.11}$$

2.3.2 The Navier-Stokes equations

x-momentum:

$$\frac{\partial(\bar{u}U_\infty)}{\partial\left(\frac{\bar{t}L}{U_\infty}\right)} + \bar{u}U_\infty\frac{\partial(\bar{u}U_\infty)}{\partial(\bar{x}L)} + \bar{v}U_\infty\frac{\partial(\bar{u}U_\infty)}{\partial(\bar{y}L)} + \bar{w}U_\infty\frac{\partial(\bar{u}U_\infty)}{\partial(\bar{z}L)} = \tag{2.12}$$

$$-\frac{1}{\rho}\frac{\partial(\bar{p}\rho U_\infty^2)}{\partial(\bar{x}L)} + \nu\left(\frac{\partial^2(\bar{u}U_\infty)}{\partial(\bar{x}L)^2} + \frac{\partial^2(\bar{u}U_\infty)}{\partial(\bar{y}L)^2} + \frac{\partial^2(\bar{u}U_\infty)}{\partial(\bar{z}L)^2}\right) + S_{Mx}$$

By dividing this equation by $\frac{U_\infty^2}{L}$, the following equation is obtained:

$$\frac{\partial\bar{u}}{\partial\bar{t}} + \bar{u}\frac{\partial\bar{u}}{\partial\bar{x}} + \bar{v}\frac{\partial\bar{u}}{\partial\bar{y}} + \bar{w}\frac{\partial\bar{u}}{\partial\bar{z}} = \tag{2.13}$$

$$-\frac{\partial\bar{p}}{\partial\bar{x}} + \textcircled{\frac{\nu}{U_\infty L}}\left(\frac{\partial^2\bar{u}}{\partial\bar{x}^2} + \frac{\partial^2\bar{u}}{\partial\bar{y}^2} + \frac{\partial^2\bar{u}}{\partial\bar{z}^2}\right) + S_{Mx}$$

In a similar way, the equations for the other two directions are obtained as follows:

y-momentum:

$$\frac{\partial\bar{v}}{\partial\bar{t}} + \bar{u}\frac{\partial\bar{v}}{\partial\bar{x}} + \bar{v}\frac{\partial\bar{v}}{\partial\bar{y}} + \bar{w}\frac{\partial\bar{v}}{\partial\bar{z}} = \tag{2.14}$$

$$-\frac{\partial\bar{p}}{\partial\bar{y}} + \textcircled{\frac{\nu}{U_\infty L}}\left(\frac{\partial^2\bar{v}}{\partial\bar{x}^2} + \frac{\partial^2\bar{v}}{\partial\bar{y}^2} + \frac{\partial^2\bar{v}}{\partial\bar{z}^2}\right) + S_{My}$$

z-momentum:

$$\frac{\partial\bar{w}}{\partial\bar{t}} + \bar{u}\frac{\partial\bar{w}}{\partial\bar{x}} + \bar{v}\frac{\partial\bar{w}}{\partial\bar{y}} + \bar{w}\frac{\partial\bar{w}}{\partial\bar{z}} = \tag{2.15}$$

$$-\frac{\partial\bar{p}}{\partial\bar{z}} + \textcircled{\frac{\nu}{U_\infty L}}\left(\frac{\partial^2\bar{w}}{\partial\bar{x}^2} + \frac{\partial^2\bar{w}}{\partial\bar{y}^2} + \frac{\partial^2\bar{w}}{\partial\bar{z}^2}\right) - g + S_{Mz}$$

The governing equations are taken into account when similarity is about to be achieved in order to see which equations are dependent on the scale. The only parameter that appears in these equations is the **Reynolds number** Rn (which appears as 1/Rn and is circled in the above equations) in the dimensionless Navier-Stokes equations (see *Eq.*(2.13), (2.14) & (2.15)), which is defined as:

$$Rn = \frac{\rho u L}{\mu} = \frac{uL}{\nu} \tag{2.16}$$

where:
u is a scalar representing the velocity in x-direction in respect to the object,
μ is the dynamic viscosity of the fluid,
ν is the kinematic viscosity of the fluid.

2.3.3 Other conditions

Other conditions are also taken into account when similarity is to be achieved. Such conditions are the boundary conditions for solid surfaces, the free-surface boundary conditions and the infinity condition (Larsson & Raven, 2010). However, the only parameters that appear in those equations are in the free-surface boundary conditions. Those parameters are:

- the Euler number En, which is used to determine the cavitation,

$$En = \frac{p_u - p_d}{\rho U_\infty^2} \tag{2.17}$$

  where:
  p_u is the upstream pressure,
  p_d is the downstream pressure.

- the Froude number Fn, which is used to determine the resistance,

$$Fn = \frac{U_\infty}{\sqrt{gL}} \tag{2.18}$$

- the Weber number Wn, which is used to determine the spray, the wave breaking and the surface waves,

$$Wn = \frac{\rho U_\infty^2 L}{\gamma} \tag{2.19}$$

  where:
  γ is the surface tension or over-speed ratio in channel.

2.4 Propeller scale effects

Looking at the performance characteristics of a propeller in both model and full-scale, and taking into account that full-scale indicates higher Reynolds number, larger diameter and lower rotational speed, the thrust coefficient K_T is almost identical while the torque coefficient K_Q in full scale is lower according to Carlton (2007) as shown in *Figure 2.4*.

It should be mentioned that the above statement applies for open shaft arrangement where a huge number of model testing has been done. On the other hand, this statement is not true for azimuth thrusters due to the high model testing uncertainties that are derived from the high viscous effects that appear at model scale. For this reason, full-scale CFD might be a better alternative for azimuth thrusters compared to model testing.

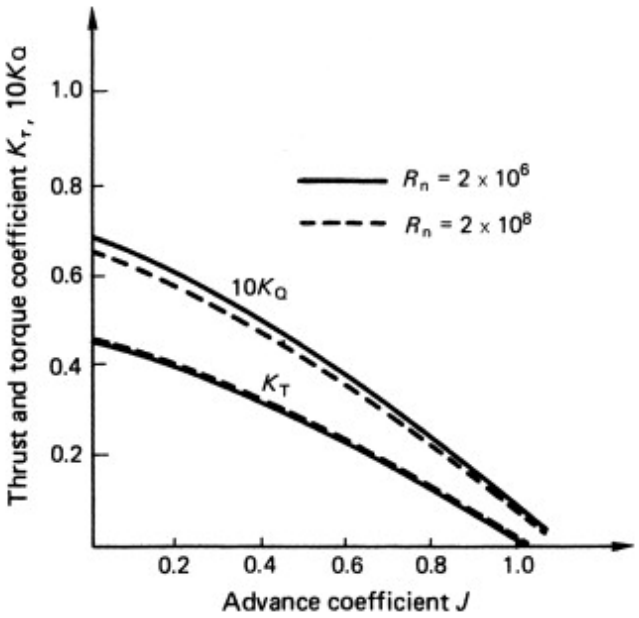

Figure 2.4: Scale effects (Carlton, 2007).

The viscous effects are the main reason for the differences between the model and full-scale due to the phenomena that are dependent on the Reynolds number. The dependency of these phenomena to the Reynolds number and consequently to the viscosity is explained thoroughly in Sections 2.2 and 2.3. The Reynolds number should be the same at both scales in order for the viscosity effects to be correct. However, due to the methods of testing model propellers, the Reynolds number ends up being different between model and full-scale and as a result a different boundary layer structure to the flow over the blades and nozzle arises. A consequence of that is the too high viscous resistance in model scale.

2.5 Types of fluid flow

- **Steady - Unsteady**
  A flow is described as steady (state) when the flow variables ϕ, such as velocity, pressure, temperature, and density, do not change through time. On the other hand, a flow is described as unsteady (also known as transient flow) when the flow variables ϕ change through time.
- **Uniform - Non-uniform**
  A flow is described as uniform when the velocity does not change through space at a specific time. On the other hand, a flow is described as non-uniform when the velocity changes through space at a specific time.
- **Laminar - Turbulent**
  A flow is described as laminar when the fluid particles follow smooth, well-defined paths. On the other hand, a flow is described as turbulent when the fluid particles follow random, chaotic paths.

- **Compressible - Incompressible**
  A flow is described as compressible when the density of the fluid ρ is dependent on the pressure, thus the density is changing within the control volume that moves with the flow velocity at regions with different pressure. On the other hand, a flow is described as incompressible when the density of the fluid ρ is independent on the pressure and thus, constant within the control volume that moves with the flow velocity at regions with different pressure.
- **Viscous - Inviscid**
  A flow is described as viscous when the fluid of the flow is viscous. On the other hand, a flow is described as inviscid when the fluid of the flow has no viscosity (i.e. viscosity is equal to zero).
- **Rotational - Irrotational**
  A flow is described as rotational when vorticity, which is the curl of the velocity vector, appears all over the flow field. On the other hand, a flow is described as irrotational when vorticity is zero all over the flow field.
- **1D - 2D - 3D**
  A flow is described as 1D when the flow variables ϕ, such as velocity, pressure, temperature and density are defined within one dimensional coordinate system in space. A flow is described as 2D and 3D when the flow variables ϕ are defined within two or three dimensional coordinate systems respectively in space.
- **Potential flow**
  A potential flow is a flow that is described by the velocity potential $\phi(x, y, z)$ for some scalar field ϕ, being a function of space and time and assuming incompressible, inviscid and irrotational flow. The flow velocity $\overrightarrow{v}$ is a vector field that is equal to the gradient of the velocity potential as shown below (Larsson & Raven, 2010):

$$\overrightarrow{v}(x, y, z) = \bigtriangledown\phi \tag{2.20}$$

2.6 Introduction to turbulence modelling

All types of fluid flow become unstable when a specific Reynolds number is exceeded. Flows are considered laminar at low Reynolds numbers while at high Reynolds numbers flows become turbulent (Versteeg & Malalasekera, 2007).

The Reynolds number associates the inertia forces that are related to the convective effects and viscous forces with the flow. A critical Reynolds number, Rn_{crit} is introduced, which determines the type of the flow. In cases where $Rn < Rn_{crit}$ the flow is considered as laminar while when $Rn \geq Rn_{crit}$ the flow is considered as turbulent. At turbulent flows the instantaneous flow variables ϕ are decomposed into a mean value and a fluctuating value. The instantaneous velocity u and pressure p are presented below:

$$u = U + u' \qquad and \qquad p = P + p' \tag{2.21}$$

where:
U is the steady mean value of the velocity component,

P is the steady mean value of the pressure component,
u' is the fluctuating velocity component,
p' is the fluctuating pressure component.

Turbulent flows include rotational flows that are called turbulent eddies. These eddies bring the fluid particles closer to each other, which results in a high heat, mass and momentum exchange. This yields to an effective mixing, which rises the diffusion coefficients. Turbulent eddies that are large enough to interact with the mean flow and extract energy from it are called vortices while vortex stretching shows how much a fluid particle has been stretched.

The characteristic velocity ϑ and the characteristic length ℓ of the larger eddies (e.g. vortices) is observed to be of the same order as the mean velocity U and length L of the mean flow. Thus, by looking at Reynolds equation (see *Eq.2.16*), it can be considered that vortices are highly influenced by inertia effects while viscous effects can be neglected due to the same order of the velocity and length. Since vortices are considered inviscid and the angular momentum is preserved, the rotation rate gets increased while the rotation radius gets decreased. This yields to creation of motion at the smaller length scales and within smaller time steps. As a result, vortex stretching provides the required energy and the turbulence is maintained.

Smaller eddies are mainly streched by larger eddies while mean flow has less impact on them. The so called energy cascade explains the transfer of kinetic energy from the larger eddies to the smaller ones. The smallest eddies that are dominated equally by inertia effects and viscous effects are called Kolmogorov microscales. The energy within these microscales is dissipated and converted into thermal energy, thus resulting in high energy losses. Kolmogorov microscales are expressed by the dissipation rate of turbulent kinetic energy ε and the fluid's kinematic viscosity ν.

Magnitude ratios of the larger scales and the Kolmogorov microscales are used in order to proceed to a dimensional analysis. These magnitude ratios, that are expressed by the characteristic velocity ϑ, length ℓ and time t of the larger scales and the characteristic velocity u, length η and time τ of the Kolmogorov microscales, are shown below:

- Velocity scale ratio:
$$\frac{u}{\vartheta} \approx Rn_\ell^{-1/4} \tag{2.22}$$
- Length scale ratio:
$$\frac{\eta}{\ell} \approx Rn_\ell^{-3/4} \tag{2.23}$$
- Time scale ratio:
$$\frac{\tau}{t} \approx Rn_\ell^{-1/2} \tag{2.24}$$

As it is already mentioned, the large eddies are considered as inviscid while they are highly dependent on the characteristic velocity ϑ and the characteristic length ℓ. As a result, the spectral energy content $E(\kappa)$ of the large eddies should be directly proportional to the characteristic velocity ϑ and the characteristic length

ℓ as shown in *Eq.*(2.25) and (2.26). The large eddies are considered anisotropic as the characteristic length ℓ is linked with components such as the boundary layer thickness δ, the obstacle width L and the surface roughness k_s.

$$E(\kappa) \propto \vartheta^2 \ell \tag{2.25}$$

where the wave number κ is defined as:

$$\kappa = \frac{1}{\ell} \tag{2.26}$$

On the other hand, Kolmogorov microscale eddies are dependent on the dissipation rate of turbulent kinetic energy ε and the fluid's kinematic viscosity ν. As a result, the energy content of the Kolmogorov microscale eddies should be directly proportional to the fluid's kinematic viscosity ν and the dissipation rate ε as shown in *Eq.*(2.27) and (2.28). The Kolmogorov microscale eddies are considered isotropic as the spectral energy content $E(\kappa)$ is linked with the dissipation rate ε.

$$E(\kappa) \propto \nu^{5/4} \varepsilon^{1/4} \tag{2.27}$$

where the wave number κ is defined as:

$$\kappa = \frac{1}{\eta} \tag{2.28}$$

2.6.1 Boundary layer

An interaction between the molecules of a solid surface, which is also known as wall, and a fluid element arises due to their collision. Hence, a tiny layer between the solid surface and the fluid elements is created where two different velocity fields are mixed. Nevertheless, these two different velocity fields get smoothed and finally become identical (i.e. the fluid element sticks to the solid surface and the difference of their velocities becomes zero). This interaction is described by the "no-slip" condition where the viscous effects (i.e. friction is included) are taken into consideration. Moving away from the solid surface, the velocity increases within the so called boundary layer. In *Figure 2.5*, the different regions of the flow are presented where the viscous sublayer and the turbulent boundary layer are part of the boundary layer while the inviscid flow is part of the free stream (Larsson & Raven, 2010).

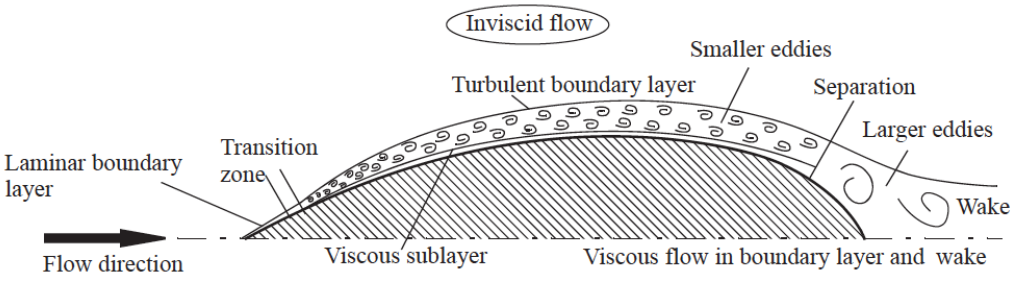

Figure 2.5: Regions of flow (Larsson & Raven, 2010).

2.6.2 Flat plate theory

The boundary layer is the most important region of flow where the transition from laminar to turbulent flow occurs. The simplest boundary layer is considered the one that is developed on a flat plate, a plate with really small thickness and parallel to the flow on which the pressure is considered constant. The flat plate consists of three regions: the laminar boundary layer, the transition region from laminar to turbulent flow and the turbulent boundary layer. The development of velocity boundary layer on a flat plate within these regions is shown in *Figure 2.6* (Larsson & Raven, 2010).

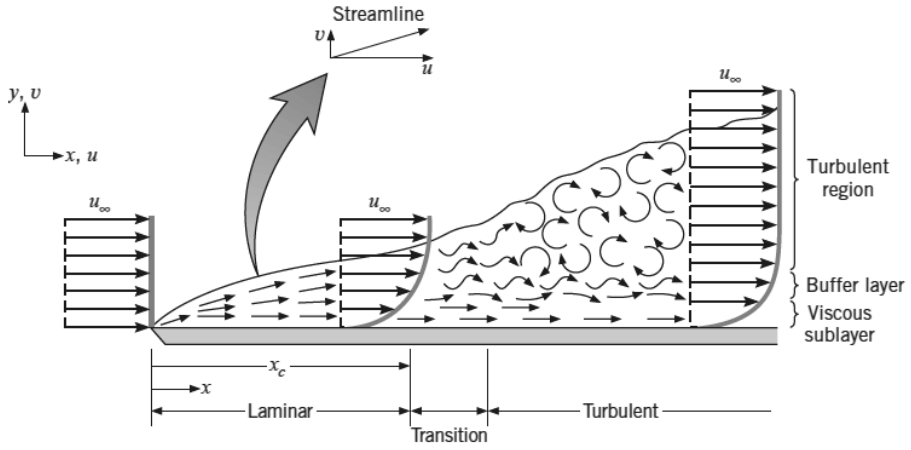

Figure 2.6: Regions of development of the velocity boundary layer on a flat plate (Bergman, Lavine, Incropera, & Dewitt, 2011).

Laminar flow is the only flow within the laminar boundary layer, which is characterized by ordered streamlines, until the transition region where an intermediate flow dominates (i.e. laminar flow within the viscous sublayer and intermediate flow within the buffer layer). Turbulent flow follows within the turbulent boundary layer where a turbulence flow dominates (i.e. laminar flow within the viscous sublayer, intermediate flow within the buffer layer and turbulent flow within the turbulent region) (Bergman, Lavine, Incropera, & Dewitt, 2011).

Moving streamwise from the laminar to the turbulent region (i.e. increasing x-direction), the boundary layer thickness δ grows (see *Figure 2.6*) and the velocity gradients on the flat plate decrease (see *Figure 2.7*).

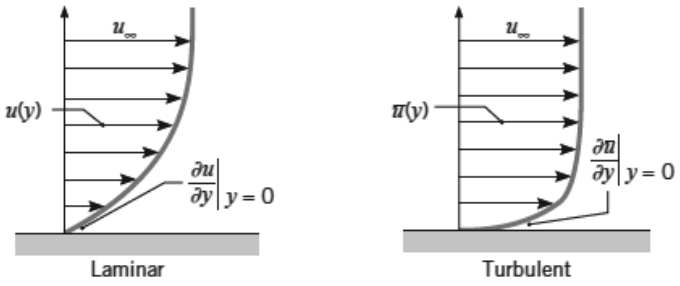

Figure 2.7: Comparison of laminar and turbulent velocity profiles of the boundary layer on a flat plate (Bergman, Lavine, Incropera, & Dewitt, 2011).

The reduction of the velocity is associated with the shear stresses τ acting in parallel to the velocity (see *Figure 2.8*) in order to conserve the particle motion at a distance δ from the solid surface.

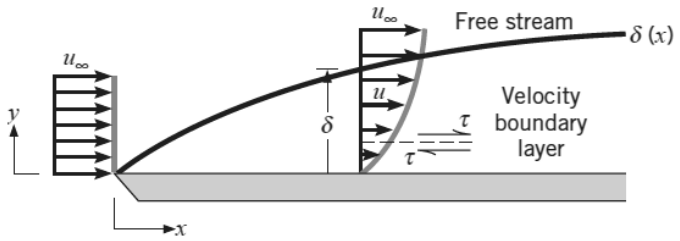

Figure 2.8: Development of the velocity boundary layer on a flat plate (Bergman, Lavine, Incropera, & Dewitt, 2011).

The velocity within the boundary layer needs to be expressed in terms of the fluid density ρ, the dynamic viscosity μ of the fluid and the shear stresses at the wall τ_w. It should be mentioned that the velocity should be kept independent of the boundary layer thickness δ. Thus, the following equations are introduced (Larsson & Raven, 2010):

- The non-dimensional velocity u^+:

$$u^+ = \frac{u}{u_\tau} \tag{2.29}$$

  where the friction velocity u_τ is defined as

$$u_\tau = \sqrt{\frac{\tau_w}{\rho}} \tag{2.30}$$

- The non-dimensional distance from the wall y^+:

$$y^+ = \frac{y u_\tau}{\nu} \tag{2.31}$$

Finally, the boundary layer can be split into four regions:

- **The viscous sublayer:** $0 \leq y^+ \leq 5$
  This region (i.e. region I) is part of the inner layer where a laminar flow dominates.

- **The buffer layer:** $5 \leq y^+ \leq 30$
  This region (i.e. region II) is part of the inner layer where an intermediate flow dominates.
- **The turbulent (logarithmic) region:** $30 \leq y^+ \leq 500$
  This region (i.e. region III) is part of the inner layer where a turbulent flow dominates.
- **The wake region:** $500 \leq y^+ \leq 10000$
  This region (i.e. region IV) is part of the outer layer. Therefore, it is not further explained.

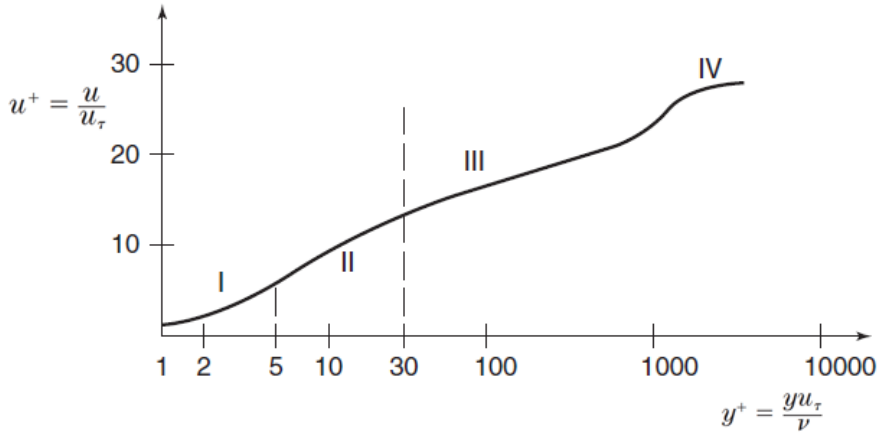

Figure 2.9: Regions of development of the velocity boundary layer on a flat plate (Larsson & Raven, 2010).

2.6.3 Numerical methods of turbulence modelling

The instantaneous flow variables are divided into a mean component and a turbulent fluctuating component. The fluctuating component consists of all scales of eddies. Based on this statement, the numerical methods that are used in order to treat the effects of turbulence are the following:

- **Reynolds-Averaged Navier-Stokes (RANS)**
  RANS uses time averaged Navier-Stokes equations to compute the steady mean flow, which is the same order as the large scale eddies (Versteeg & Malalasekera, 2007). Then, the effects of all the scales of eddies to the mean flow are modelled (Larsson & Raven, 2010).
- **Large Eddy Simulation (LES)**
  LES uses space filtering of the unsteady Navier-Stokes equations to compute the flow including large scale eddies (Larsson & Raven, 2010). Then, the effects of the small scale eddies are modelled.
- **Direct Numerical Simulation (DNS)**
  DNS uses the unsteady Navier-Stokes equations to compute the flow including all the scales of eddies, even the smallest ones which are the same scale as the Kolmogorov microscale eddies.

LES and DNS methods provide higher resolution and a more detailed description

of turbulence compared to RANS. However, both LES and DNS are much more expensive methods and the level of resolution and details that both provide is usually not needed. On the other hand, RANS yields a decent level of resolution and details, which are the result of the averaged flow properties such as the mean values of the velocities, pressures and stresses. Due to this fact, RANS method has been used the most among the three.

2.6.4 The Reynolds-Averaged Navier-Stokes equations

Taking the average of each term, one gets $u = \overline{u} + u' = U + u'$. The overbar (e.g. $\overline{u}$) or capital letters (e.g. U) indicate averaging and $\overline{u'} = 0$. Hence, the **continuity equation** is formed as (Fletcher, 1991):

$$\frac{\partial \overline{\rho}}{\partial t} + div(\overline{\rho u}) = 0 \tag{2.32}$$

which can also be written as:

$$\frac{\partial \overline{\rho}}{\partial t} + \frac{\partial}{\partial x}\overline{\rho u} \cdot dV + \frac{\partial}{\partial y}\overline{\rho v} \cdot dV + \frac{\partial}{\partial z}\overline{\rho w} \cdot dV = 0 \tag{2.33}$$

However, since the fluid is considered incompressible (i.e. $\rho = \overline{\rho}$) and by taking into account that $\overline{div(u)} = div(U)$, the continuity equation can be re-written as:

$$div(U) = 0 \tag{2.34}$$

Then, by taking the average of each term of the **Navier-Stokes equations** (see *Eq.*(2.7), (2.8) & (2.9)) for incompressible flow and assuming that the gravity g is the only body force along the z-axis, the RANS equation are obtained:

x-momentum:

$$\overline{\frac{\partial(\rho u)}{\partial t}} + \overline{div(\rho u u)} = \overline{-\frac{\partial p}{\partial x}} + \overline{div(\mu \text{ grad } u)} + S_{Mx} \tag{2.35}$$

Then, the mean and fluctuating components (see *Eq.*(2.21)) are introduced into the time-average of each term:

$$\frac{\partial(\rho U)}{\partial t} + div(\rho U U) + div(\overline{\rho u' u'}) = -\frac{\partial P}{\partial x} + div(\mu \text{ grad } U) + S_{Mx} \tag{2.36}$$

where:

$$\overline{\frac{\partial(\rho u)}{\partial t}} = \frac{\partial(\rho U)}{\partial t}, \qquad \overline{div(\rho u u)} = div(\rho U U) + div(\overline{\rho u' u'}) \tag{2.37}$$

$$\overline{-\frac{\partial p}{\partial x}} = -\frac{\partial P}{\partial x}, \qquad \overline{div(\mu \text{ grad } u)} = div(\mu \text{ grad } U)$$

Rearranging *Eq.*(2.36) and moving the fluctuating components on the right hand side, the following equation is obtained:

$$\rho\left(\frac{\partial U}{\partial t}+U\frac{\partial U}{\partial x}+V\frac{\partial U}{\partial y}+W\frac{\partial U}{\partial z}\right)=-\frac{\partial P}{\partial x}+\mu\left(\frac{\partial^2 U}{\partial x^2}+\frac{\partial^2 U}{\partial y^2}+\frac{\partial^2 U}{\partial z^2}\right)+ \tag{2.38}$$

$$\left[\frac{\partial(-\rho\overline{u'^2})}{\partial x}+\frac{\partial(-\rho\overline{u'v'})}{\partial y}+\frac{\partial(-\rho\overline{u'w'})}{\partial z}\right]+S_{Mx}$$

Dividing by ρ, the following equation is obtained:

$$\frac{\partial U}{\partial t}+U\frac{\partial U}{\partial x}+V\frac{\partial U}{\partial y}+W\frac{\partial U}{\partial z}=-\frac{1}{\rho}\frac{\partial P}{\partial x}+\nu\left(\frac{\partial^2 U}{\partial x^2}+\frac{\partial^2 U}{\partial y^2}+\frac{\partial^2 U}{\partial z^2}\right)+ \tag{2.39}$$

$$\frac{1}{\rho}\left[\frac{\partial(-\rho\overline{u'^2})}{\partial x}+\frac{\partial(-\rho\overline{u'v'})}{\partial y}+\frac{\partial(-\rho\overline{u'w'})}{\partial z}\right]+\frac{1}{\rho}S_{Mx}$$

In a similar way, the equations for the other two directions are obtained as follows:

y-momentum:

$$\frac{\partial V}{\partial t}+U\frac{\partial V}{\partial x}+V\frac{\partial V}{\partial y}+W\frac{\partial V}{\partial z}=-\frac{1}{\rho}\frac{\partial P}{\partial x}+\nu\left(\frac{\partial^2 V}{\partial x^2}+\frac{\partial^2 V}{\partial y^2}+\frac{\partial^2 V}{\partial z^2}\right)+ \tag{2.40}$$

$$\frac{1}{\rho}\left[\frac{\partial(-\rho\overline{u'v'})}{\partial x}+\frac{\partial(-\rho\overline{v'^2})}{\partial y}+\frac{\partial(-\rho\overline{v'w'})}{\partial z}\right]+\frac{1}{\rho}S_{My}$$

z-momentum:

$$\frac{\partial W}{\partial t}+U\frac{\partial W}{\partial x}+V\frac{\partial W}{\partial y}+W\frac{\partial W}{\partial z}=-\frac{1}{\rho}\frac{\partial P}{\partial x}+\nu\left(\frac{\partial^2 W}{\partial x^2}+\frac{\partial^2 W}{\partial y^2}+\frac{\partial^2 W}{\partial z^2}\right)+ \tag{2.41}$$

$$\frac{1}{\rho}\left[\frac{\partial(-\rho\overline{u'w'})}{\partial x}+\frac{\partial(-\rho\overline{v'w'})}{\partial y}+\frac{\partial(-\rho\overline{w'^2})}{\partial z}\right]-g+\frac{1}{\rho}S_{Mz}$$

By looking at the Navier-Stokes equations (see *Eq.*(2.7), (2.8) & (2.9)) and the RANS equations (see *Eq.*(2.39), (2.40) & (2.41)), nine extra terms can be observed, which represent three normal stresses:

$$\tau_{xx}=-\rho\overline{u'^2},\qquad \tau_{yy}=-\rho\overline{v'^2},\qquad \tau_{zz}=-\rho\overline{w'^2} \tag{2.42}$$

and three double shear stresses:

$$\tau_{xy}=\tau_{yx}=-\rho\overline{u'v'},\qquad \tau_{xz}=\tau_{zx}=-\rho\overline{u'w'},\qquad \tau_{yz}=\tau_{zy}=-\rho\overline{v'w'} \tag{2.43}$$

These stresses are knows at the Reynolds stresses. The Reynolds stresses are additional turbulent shear stresses within the fluid layers, which are result of momentum exchange derived from the convective transport by the eddies. This momentum exchange results to a deceleration of the faster moving fluid layers and an acceleration of the slower moving fluid layers. The symmetry of the double shear stresses is explained by the identical net flux of the x, y and z-momentum accordingly and the identical mean component of this net flux of the x, y and z-momentum out of the control volume (Versteeg & Malalasekera, 2007).

2.6.5 Turbulence models

For most CFD purposes, there is no need to resolve the details of the turbulent fluctuations. Thus, most of the turbulent flow computations are based on RANS equations. However, the effects of turbulence on the mean flow are important. In order to be able to compute turbulent flows with RANS that include the turbulence effects, turbulence models to predict the already mentioned Reynolds stresses as well as scalar transport terms are needed (Versteeg & Malalasekera, 2007).

Some of the most common turbulence models that are usually used in CFD are presented below:

- $\kappa - \varepsilon$ model
- Reynolds stress equation model (RSM)
- Wilcox $\kappa - \omega$ model
- Menter Shear Stress Transport (SST) $\kappa - \omega$ model

2.6.6 Menter SST $\kappa - \omega$ turbulence model

Menter SST $\kappa - \omega$ model is a hybrid model that uses the original Wilcox $\kappa - \omega$ model to solve the boundary layer due to its high sensitivity to the arbitrary assumed values and the $\kappa - \varepsilon$ model to solve the regions located far from the wall, which are fully turbulent.

The turbulent kinetic energy k, which is derived from the Navier-Stokes equations, is defined as the half of the sum of the fluctuating velocity components (Versteeg & Malalasekera, 2007):

$$k = \frac{1}{2}(\overline{u'^2} + \overline{v'^2} + \overline{w'^2}) \tag{2.44}$$

The dissipation rate of turbulent kinetic energy ε is defined as:

$$\varepsilon = 2\nu\overline{s'_{ij} \cdot s'_{ij}} \tag{2.45}$$

Finally, the specific dissipation rate of turbulent energy ω is defined as:

$$\omega = \frac{\varepsilon}{k} \tag{2.46}$$

For the $k - \varepsilon$ model, the velocity scale ϑ and the length scale ℓ are defined as:

$$\vartheta = k^{1/2} \tag{2.47}$$

$$\ell = \frac{k^{3/2}}{\varepsilon} \tag{2.48}$$

For the $k-\omega$ model, the velocity scale ϑ is the same as above while the the length scale ℓ is defined as:

$$\ell = \frac{k^{1/2}}{\omega} \tag{2.49}$$

The Reynolds stress and the k-equation are identical to the original Wilcox $k-\omega$ model:

$$\tau_{ij} = -\rho\overline{u'v'} = -\rho\overline{u_i'u_j'} = 2\mu_t S_{ij} - \frac{2}{3}\rho k\delta_{ij} = \mu_t\left(\frac{\partial U_i}{\partial x_j} + \frac{\partial U_j}{\partial x_i}\right) - \frac{2}{3}\rho k\delta_{ij} \tag{2.50}$$

$$\frac{\partial(\rho k)}{\partial t} + div(\rho k U) = div\left[\left(\mu + \frac{\mu_t}{\sigma_k}\right)grad(k)\right] + P_k - \beta^*\rho k\omega \tag{2.51}$$

while the ε-equation is transformed into an ω-equation by substituting $\varepsilon = k\omega$:

$$\frac{\partial(\rho\omega)}{\partial t} + div(\rho\omega U) = div\left[\left(\mu + \frac{\mu_t}{\sigma_{\omega,1}}\right)grad(\omega)\right] + \gamma_2\left(2\rho S_{ij}\cdot S_{ij} - \frac{2}{3}\rho\omega\frac{\partial U_i}{\partial x_j}\delta_{ij}\right) -$$

$$\beta_2\rho\omega^2 + 2\frac{\rho}{\sigma_{\omega,2}\omega}\frac{\partial k}{\partial x_k}\frac{\partial\omega}{\partial x_k} \tag{2.52}$$

The turbulent eddy viscosity is defined as:

$$\mu_t = \frac{\alpha_1\rho k}{max(\alpha_1\omega, SF_2)} \tag{2.53}$$

where:

$$S = \sqrt{2S_{ij}S_{ij}} \tag{2.54}$$

the blending function is defined as (Menter, Kuntz, & Langtry, 2003):

$$F_2 = tanh\left[\left[max\left(\frac{2\sqrt{k}}{\beta^*\omega y}, \frac{500\nu}{y^2\omega}\right)\right]^2\right] \tag{2.55}$$

and P_k is defined as:

$$P_k = min\left(10\beta^*\rho k\omega, 2\mu_t S_{ij} - \frac{2}{3}\rho k\frac{\partial U_i}{\partial x_j}\delta_{ij}\right) \tag{2.56}$$

while the revised model constants are the following (Versteeg & Malalasekera, 2007):

$$\sigma_k = 1.000, \quad \sigma_{\omega,1} = 2.000, \quad \gamma_2 = 0.440 \quad \beta_2 = 0.083 \quad \beta^* = 0.090$$

and $\alpha_1 = 5/9$ according to Menter et al. (2003).

2.7 Open water characteristics

The open water propeller characteristics are performance characteristics of a propeller operating in a uniform flow, that are usually obtained by model testing in a towing tank (see *Figure 2.10*) or in a cavitation tunnel (see *Figure 2.11*). In cases where the propeller is placed behind the hull, the inflow is not uniform. The thrust T and the torque Q of the propeller are measured while the rotational speed n is most of the times kept constant and the advance velocity V_A varies (Dyne & Bark, 2005).

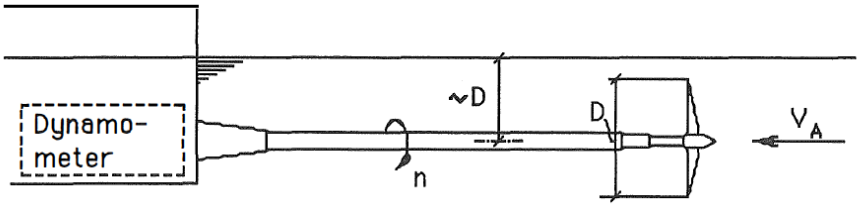

Figure 2.10: Arrangement of an open water test in a towing tank (Dyne & Bark, 2005).

Having everything known, the advance coefficient J is then obtained:

$$J = \frac{V_A}{nD} \tag{2.57}$$

which is a non-dimensional value that describes the operating condition of the propeller.

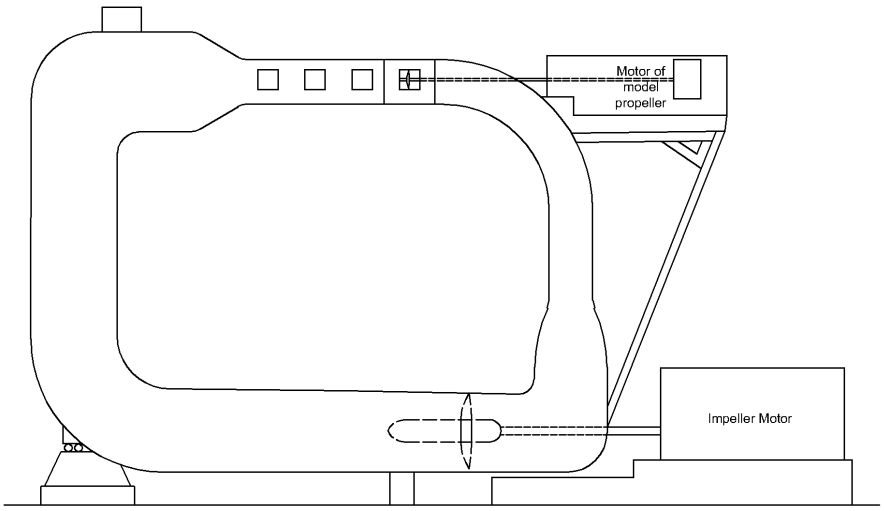

Figure 2.11: Arrangement of an open water test in a cavitation tunnel.

Then, the non-dimensional thrust coefficient K_T and torque coefficient K_Q are obtained:

$$K_T = \frac{T}{\rho n^2 D^4} \tag{2.58}$$

$$K_Q = \frac{Q}{\rho n^2 D^5} \tag{2.59}$$

The delivered power to the propeller via the shaft P_D is defined as:

$$P_D = 2\pi n Q \tag{2.60}$$

and the thrust power that is created from the propeller P_T is:

$$P_T = T V_A \tag{2.61}$$

The open water efficiency η_0 is finally defined as:

$$\eta_0 = \frac{P_T}{P_D} = \frac{J}{2\pi} \cdot \frac{K_T}{K_Q} \tag{2.62}$$

The results of an open water test are presented through an open water characteristics diagram as shown in *Figure 2.12*.

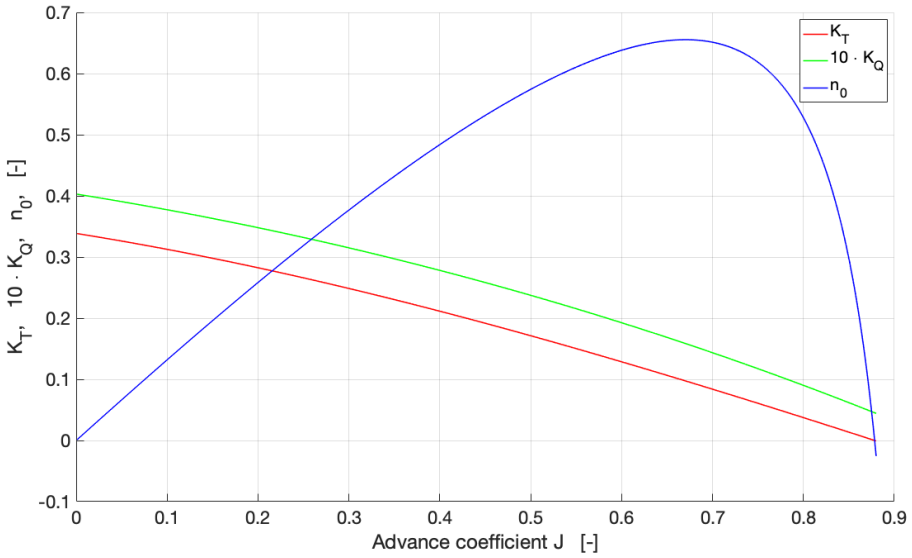

Figure 2.12: Open water characteristics diagram.

2.8 Propulsive factors

The propulsive factors are factors that express specific quantities of the flow that are relevant to the operation of a ship's propeller. Moreover, these factors also express the hydrodynamic interaction between the propeller and the hull, which is really important during the design of a propeller. The propulsive factors are determined based on values measured during open water tests, resistance tests and self propulsion tests. These propulsive factors are:

- The thrust deduction fraction t, which is defined as:

$$t = \frac{\Delta R}{T} \tag{2.63}$$

where:
ΔR is the increase of the resistance due to the propulsor.

- The effective mean wake w_{TM}, which is defined as:

$$w_T = \frac{V_S - V_{AT}}{V_S} \tag{2.64}$$

where:
V_{AT} is the advance mean velocity where T stands from the thrust,
V_S is the ship velocity.

- The relative rotative efficiency η_R, which is defined as:

$$\eta_R = \frac{K_{Q_o}}{K_Q} \tag{2.65}$$

where:
K_{Q_o} is the torque coefficient in open water condition,
K_Q is the torque coefficient in behind condition.

- The total propulsive efficiency η_D, which is defined as:

$$\eta_D = \eta_o \cdot \eta_R \cdot \eta_H \tag{2.66}$$

where the hull efficiency η_H is defined as:

$$\eta_H = \frac{R/T}{V_A/V_S} = \frac{1-t}{1-w_T} \tag{2.67}$$

and R is the resistance of the hull.

Another useful factor often connected to the hydrodynamic interactions, even if itself is a mechanical interaction, is the shaft efficiency η_S, which is defined as:

$$\eta_S = \frac{P_D}{P_B} \tag{2.68}$$

where:
P_B is the brake power.

Empirically, η_S is set to 0.97 for open shaft configurations and to 0.95 for azimuth thrusters.

2.9 Bollard pull condition

In Section 2.8, the **conventional ways** to express the hydrodynamic interactions that are commonly used in free sailing condition are presented. However, during **bollard pull condition** the movement of a vessel is restricted. The real application that the bollard pull condition tries to capture is the pushing or pulling of a really heavy structure (e.g. a vessel) or equipment (e.g. anchors for drilling rigs), which results to a high power operation and a vessel speed really close to zero. During bollard pull testing, a vessel operates in full power while it is connected on a bollard on shore through a tow-line. As a result, the ship's velocity V_S is zero and the advance velocity V_A looses its meaning since the ship is not moving. This yields an advance coefficient J equal to zero.

In bollard pull condition, the thrust deduction fraction t is mainly used to describe the increase of the resistance due to the suction of the propeller and to determine the generated thrust. On the other hand, some of the other conventional hydrodynamic interactions such as the effective Taylor's wake fraction w_T, the relative rotative efficiency η_R and the propulsive efficiency η_D cannot be applied and some alternative ways have to be used instead. The **merit coefficient** m_c is introduced as a replacement of the total propulsive efficiency η_D in order to be able to express the performance of the thruster. The merit coefficient is defined as:

$$m_c = \frac{(K_T/\pi)^{3/2}}{K_Q} \tag{2.69}$$

As it has already been mentioned, a vessel operates in full power while it is connected on a bollard on shore through a tow-line while bollard pull testing. This force applied on the line is represented in tons and is defined as:

$$T_{BP} = \frac{T_{tot}}{g} \tag{2.70}$$

Bollard pull condition is really important for tug boats among other types of vessels. However, it should be acknowledged that tug boats usually operate in really low power while high power is used only for a short period of time, which is usually less than the full power that bollard pull condition indicates. Though, full power is mainly used only during bollard pull testing during the vessel's sea trials.

2.10 Modelling methodologies

The CFD modelling of a propeller indicates a relative motion between the stationary parts (i.e. static parts such as the nozzle, gear case housing, hull) and the rotor (i.e. rotating parts such as the propeller blades, hub) of a propulsion unit and the vehicle (e.g. ship, airplane) that this propulsion unit is mounted on. Two methodologies have been widely used within the industry through the years among many other methodologies that are trying to capture the propeller motion. Those two methodologies are the Multiple Reference Frame (MRF) and the Sliding Mesh Interface

(SMI) (Tabib, Siddiqui, Rasheed, & Kvamsdal, 2017).

MRF is a steady state approach, which indicates a frozen rotor hypothesis. The RANS equations are solved for both the stationary parts and the rotor while the rotation effect of the rotor is taken into account by including the coriolis and centrifugal forces in additional source terms in the momentum equations.

SMI is a transient approach, which indicates a rotation of the rotor relative to the stationary parts. In a similar way as before, the RANS equations are solved for both the stationary parts and the rotor while the rotation effect of the rotor and the unsteady interactions between the stationary parts and the rotor are taken into account by solving the conservation equations on a moving (i.e. sliding) mesh. Moreover, the rotation effect of the moving volume mesh is taken into account by including the mesh motion flux in the face mass flux computation in the convective terms of the governing equations. Finally, the position of the mesh of the rotor is updated after every time step.

Here it should be mentioned that for both the MRF and SMI approaches, an Arbitrary Mesh Interpolation (AMI) takes place between the stationary parts and the rotor.

Comparing the two numerical modelling methodologies, it is concluded that the SMI approach reproduces representative hydrodynamic interactions such as the tip vortices, steep velocity gradients etc. and the transient behavior of the wake region is more realistic. On the other hand, MRF approach is weaker on calculating these significant details. Moreover, SMI shows higher accuracy on predicting the power and thrust. Nevertheless, it should be considered that SMI is much more expensive in terms of computational time compared to the MRF methodology and as a result, the use of MRF is often more realistic (J. Liu, Lin, & Purimitla, 2016).

3
Geometry

In this chapter, the main particulars of the vessel and the machinery that are used within this project are presented. Moreover, an explanation and representation of the geometries follows.

3.1 Main particulars

The classification and the dimensions of the vessel that is used within this study as well as the machinery, which includes the main engines, the propulsion and the propeller specifications, are presented in *Table 3.1*.

Classification	Harbour tug boat	
Dimensions	Length overall, L_{OA}	26.50 m
	Rule length, L_{PP}	22.60 m
	Max. breadth, B	11.40 m
	Draft (design), T	5.50 m
Machinery	**Main Engines**	
	Make	2x Caterpillar
	Type	B-rated 3516E
	Effect, each engine	2100 kW
	Rpm	1600
	Propulsion	
	Make	2x Caterpillar
	Type	Simplified MTA627
	Propellers	
	Make	2x Caterpillar
	Type	FPP
	Diameter, D_P	2.70 m
	Expanded blade area ration, EAR	0.67
	Design pitch ratio at 0.7r	1.136
	No. blades, Z	4

Table 3.1: Main particulars

3.2 Azimuth thruster

In *Figure 3.1*, the starboard ducted azimuth thruster (i.e. azimuth thruster that includes a nozzle) that is studied within this project is presented. During the CFD simulations the thruster is split into four different components: the propeller, which is also split into the four blades and the hub, the nozzle, the gear case housing and the lid. It should be mentioned that the lid is a geometry that does not exist in reality since the azimuth thruster is connected directly to the hull. However, its presence is important in order to have a closed geometry at the top of the gear case housing so that no strange flow is created around this region.

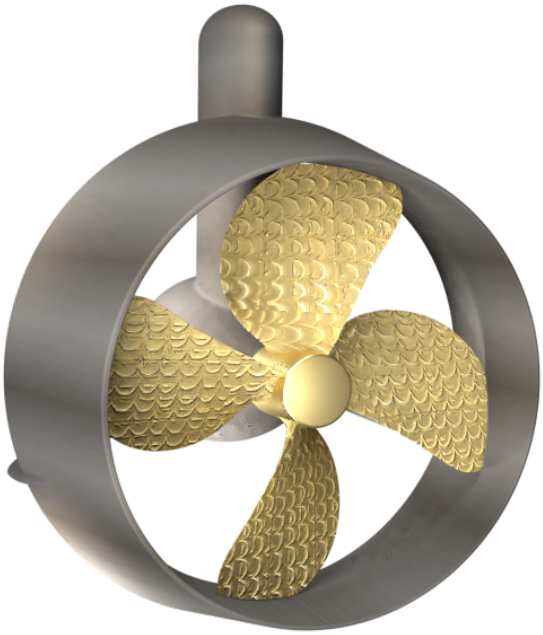

Figure 3.1: Starboard ducted azimuth thruster.

3.3 Hull

In *Figure 3.2*, the azimuth thrusters and the hull that are studied within this project are presented. The lid that is mentioned above is removed and the gear case housing is connected directly to the hull. Moreover, the hull is split into two different components: the main hull and the skeg, which is the "fin" under the hull that is used for stability during sailing.

Moreover, the azimuth thruster is rotated 6° around x-axis and 6° around y-axis as shown in *Figure 3.3*.

Finally, it is important to keep in mind that during the CFD simulations a symmetry plane is used on top of the domain while the water surface in *Figure 3.2* is used only for visualization and understanding of the geometries.

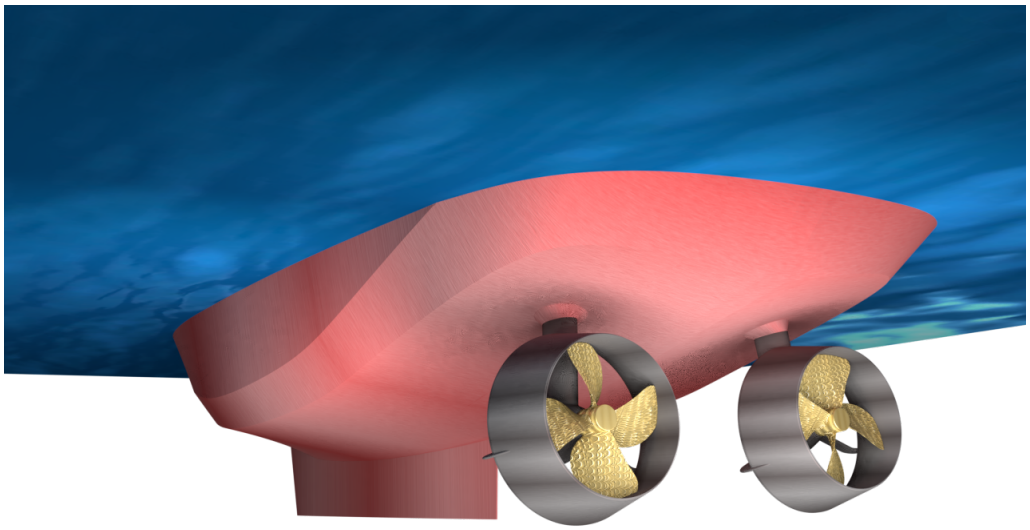

Figure 3.2: Ducted azimuth thrusters and hull.

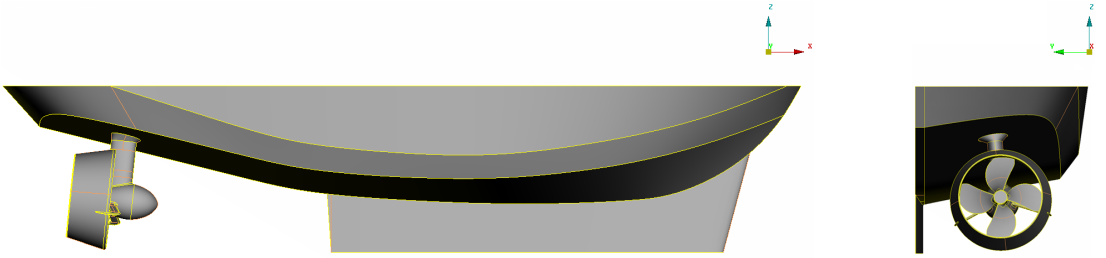

(a) Side view. **(b)** Rear view.

Figure 3.3: Ducted azimuth thrusters and hull.

4
Methodology

In this chapter, the methodology used in order to accomplish the CFD simulations is presented. In the first sections the three main steps of CFD (i.e. pre-processing, solving and post-processing) are presented while in the end the system used to run OpenFOAM is demonstrated.

As already mentioned in Section 1.4.1, the hydrodynamic interactions between the propeller, the nozzle, the gear case housing and the hull need to be investigated. Thus, the following cases are defined and then investigated separately:

- **Case 1**:
  The propeller and the nozzle in open water condition,
- **Case 2**:
  The propeller, the nozzle and the gear case housing in open water condition,
- **Case 3**:
  The propeller, the nozzle, the gear case housing and the hull in behind condition.

In order to achieve such an investigation, as also mentioned in Section 2.1, the input problem parameters need to be defined and specific tools need to be developed for analyzing the results. Thus, the following sections present the mandatory steps for the setup of a series of investigations within this study project.

4.1 Pre-processing

4.1.1 Definition of the computational domain

The main geometries used within this study project are modelled prior to this study by *Caterpillar Propulsion AB*, using Computer Aided Design (CAD) software packages. These geometries are later provided to the author and researcher of this project. However, small geometrical changes are made by the author using the Computer Aided Engineering (CAE) software ANSA pre-processor v.19.0.1. The flow domain is then defined using ANSA pre-processor, which is built around the main geometries. Here it should be noted that all the simulation models are defined in full-scale.

In *Figure 4.1*, the geometry of Case 1 is presented. A shaft that is connected to the hub and to the inlet of the domain is added in order to get rid of the stagnation point that would be created at the center of the hub in case the shaft was not added.

The velocity of the fluid would end up being zero at the stagnation point and thus, strange flows at this region would be created.

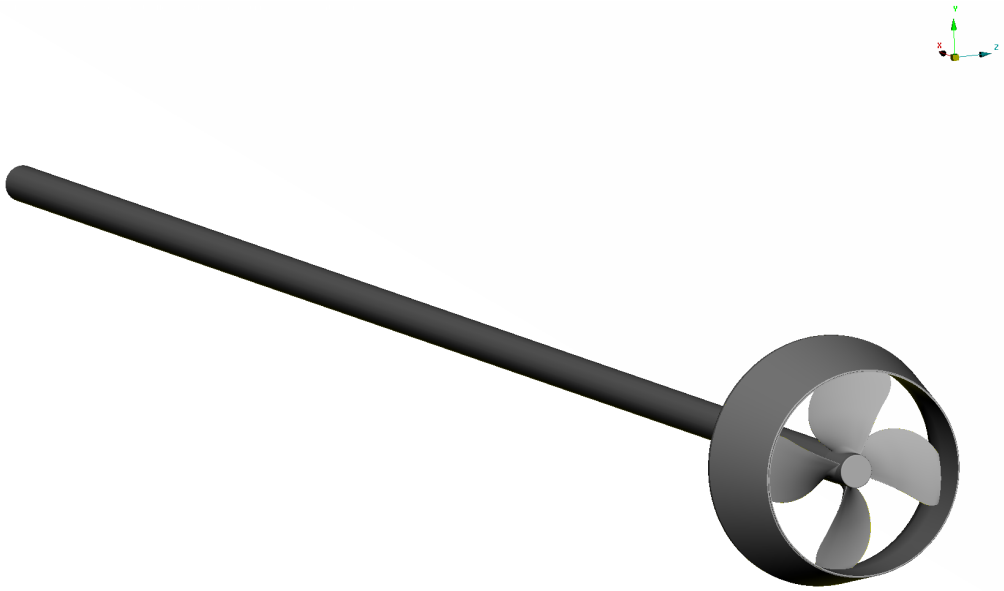

Figure 4.1: Geometry of Case 1.

In *Figure 4.2*, the domain of Case 1 is presented. The dimensions of the domain are:

- Diameter $d = 20D_P = 54m$
- Length $L = 30D_P = 81m$

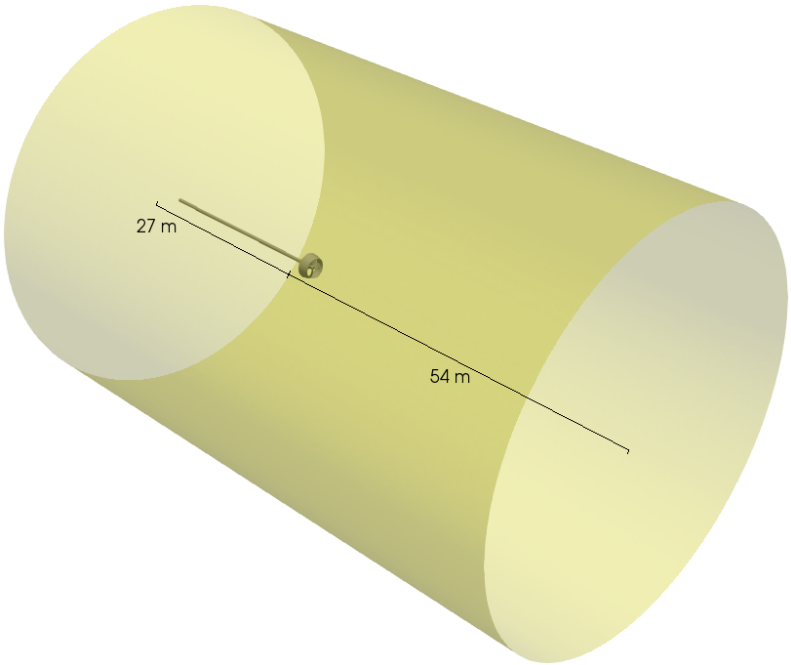

Figure 4.2: Domain of Case 1.

In *Figure 4.3*, the geometry of Case 2 is presented while the domain of Case 2 is identical to Case 1. As already mentioned in Chapter 3, the lid is an additional geometry that does not exist in reality since the azimuth thruster is connected directly to the hull. However, its presence is important in order to have a closed geometry so that no strange flow is created around this region.

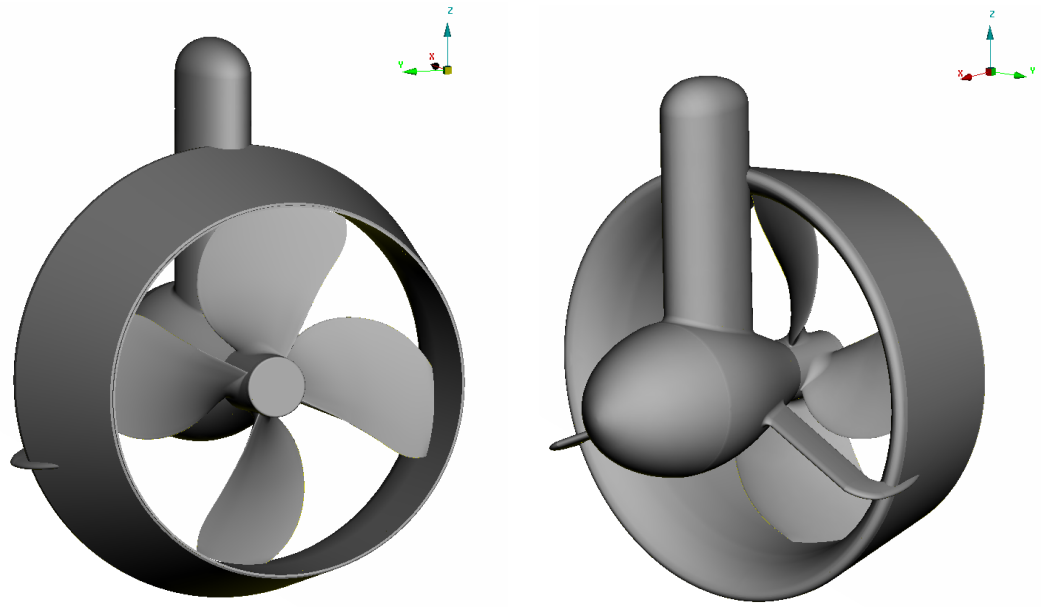

(a) Azimuth thruster pressure side. **(b)** Azimuth thruster suction side.

Figure 4.3: Geometry of Case 2.

In *Figure 4.4*, the geometry of Case 3 is presented,

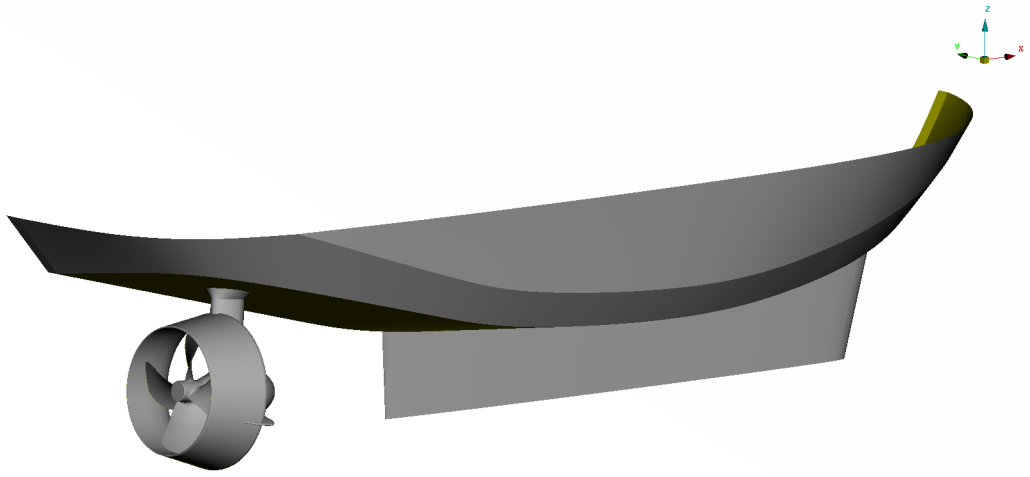

Figure 4.4: Geometry of Case 3.

while in *Figure 4.5*, the domain of Case 3 is presented. The dimensions of the domain are:

- Width $W \approx 20D_P = 2.3L_{PP} = 52m$
- Height $H \approx 20D_P = 2.3L_{PP} = 52m$
- Length $L \approx 58D_P = 6.9L_{PP} = 156m$

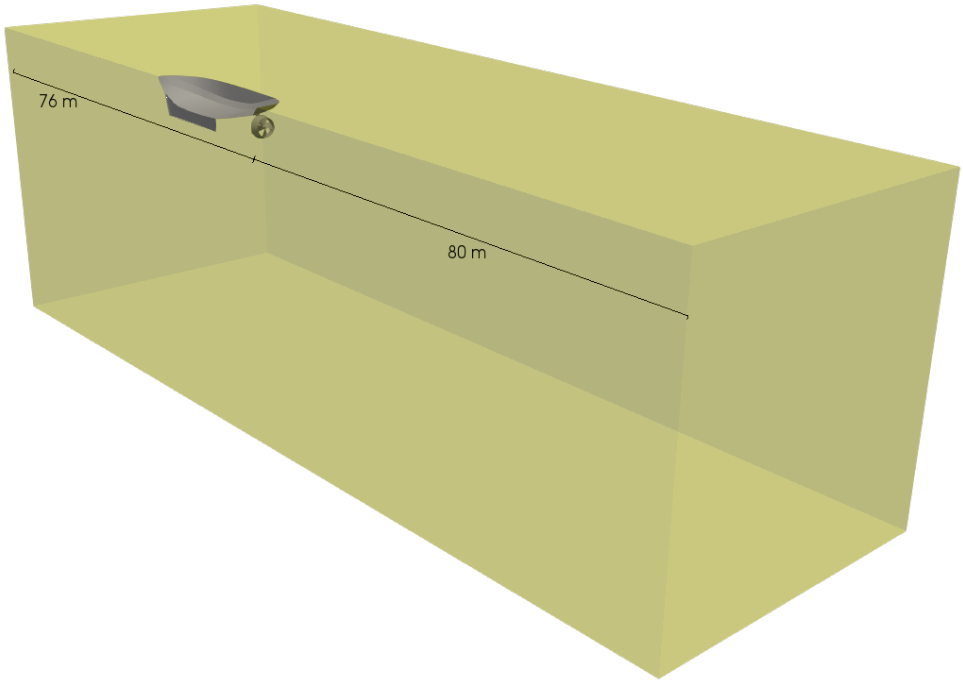

Figure 4.5: Domain of Case 3.

Looking at both the geometry and the domain of Case 3, it is clear that the the hull geometry is split into half and the reason is due to the geometrical symmetry. Thus, there is no need of simulating the whole geometry since this would result into a much more expensive computational simulation. A symmetry boundary layer during the CFD simulations is set on the top and side boundaries instead.

4.1.2 Grid generation

The grid that is used within this study is generated with ANSA pre-processor, using semi-automated functions and then manual corrections. The grid is a non-uniform mesh where finer mesh size is used in regions with large geometrical variations and coarser mesh size in regions with smaller geometrical variations.

Initial step of the meshing is the creation of a **surface mesh** with triangle shapes. Then, **layers** are created around the boundaries, which are a type of volume mesh that are created by the extrusion of the triangle surface mesh. In the next step, a **volume mesh** is created within the whole domain, which consists of elements with pyramid, tetrahedral and hexahedral shapes.

In *Figure 4.6*, the different types of mesh used in Case 1 are presented as an example. More precisely, the surface mesh appearing on the blades, the hub and the inner part of the nozzle is highlighted with magenta color, the layers around the solid geometries are highlighted with green and the volume mesh is highlighted with brown. Finally, the surface mesh on the nozzle is highlighted with lilac color.

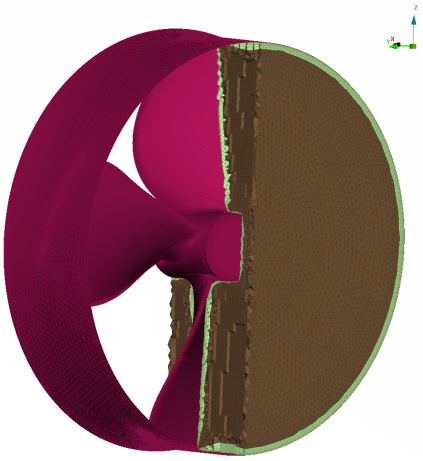

(a) Mesh of the rotor.

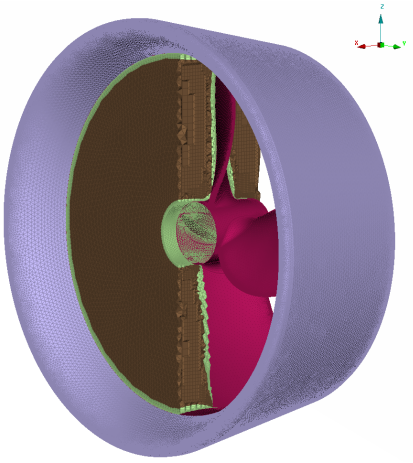

(b) Mesh of the rotor and the nozzle.

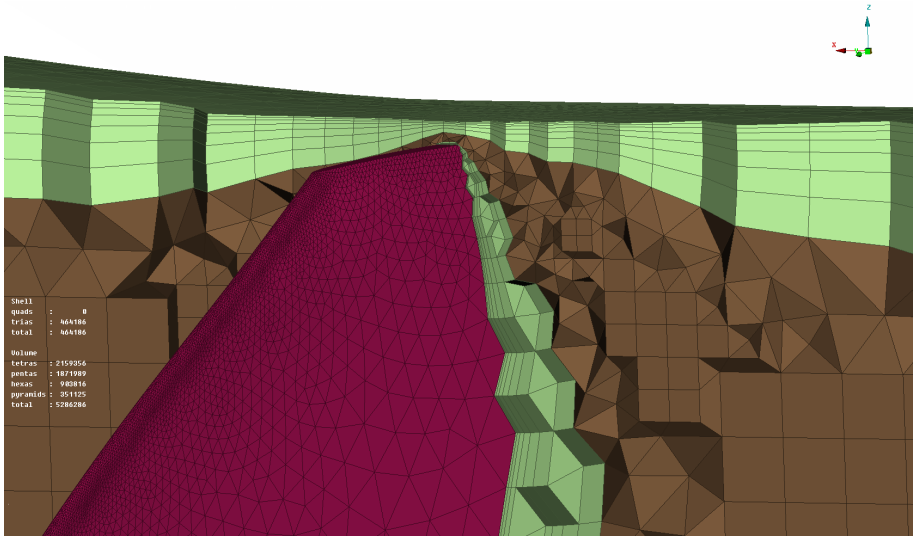

(c) Demonstration of the different types of mesh.

Figure 4.6: Initial mesh of Case 1.

Finally, the triangle (i.e. trias) and the square (i.e. quads) elements of the surface mesh are converted into polygons, the extruded triangle shapes of the layers are converted into extruded polygon shapes and the pyramid, tetrahedral (i.e. tetras), pentahedral (i.e. pentas) and hexahedral (i.e. hexas) elements of the volume mesh are **converted into polyhedral** elements.

In *Figure 4.7*, the converted polyhedral mesh of Case 1 is presented.

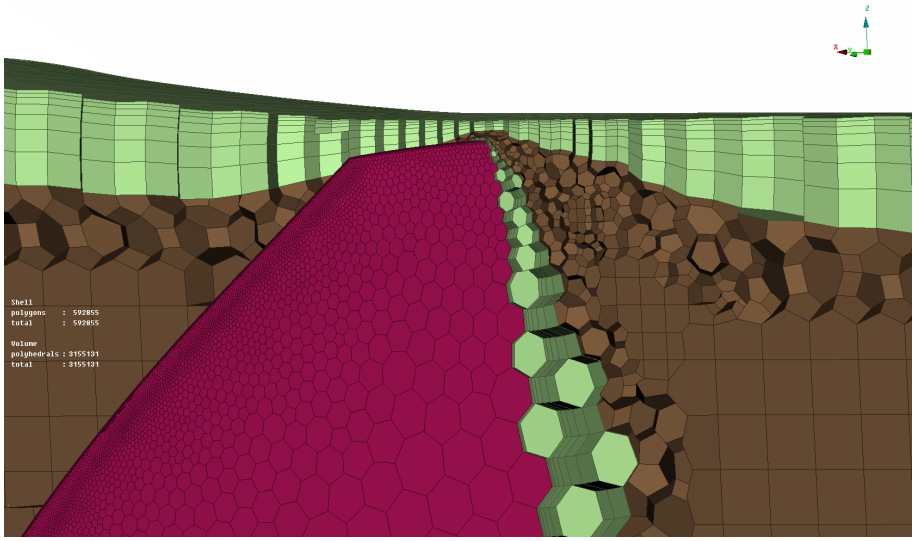

Figure 4.7: Final mesh of Case 1.

The cell sizes vary from $0.027\% \cdot D_P \approx 0.75mm$ at regions that require really high accuracy (i.e. leading and trailing edge of the propeller blades) to $124.000\% \cdot D_P \approx 3348.00mm$ at regions that require lower accuracy (i.e. domain). Moreover, seven layers are created around the boundaries with a growth factor of 1.5 and the first layer having a height with an aspect ratio of 0.05 (i.e. first height = base length $\cdot$ 0.05). In the following tables the total numbers of cells of all the three cases used within this study are demonstrated. The naming of the following elements and categories is presented as in ANSA Pre-processor v.19.0.1. The **shell elements** are surface elements that are referring to the trias, quads and polygons. On the other hand, the **volume elements** are referring to the the pyramids, tetras, pentas, hexas and polyhedrals. The layers that have already been discussed are part of the volume elements.

	Element type	**Surface mesh**	**Volume mesh**	**Volume mesh (Polyhedrals)**
No. Shell elements	trias	790,424	1,488,950	0
	quads	0	9,590	0
	polygons	0	0	1,208,839
	Total	**790,424**	**1,498,540**	**1,208,839**
No. Volume elements	pyramids	-	1,009,107	0
	tetras	-	6,139,306	0
	pentas	-	5,514,141	0
	hexas	-	3,324,486	0
	polyhedrals	-	0	9,813,408
	Total	**-**	**15,987,040**	**9,813,408**

Table 4.1: Number of cells: Case 1.

	Element type	Surface mesh	Volume mesh	Volume mesh (Polyhedrals)
No. Shell elements	trias	785,710	1,483,579	0
	quads	0	7,637	0
	polygons	0	0	1,217,205
	Total	**785,710**	**1,491,216**	**1,217,205**
No. Volume elements	pyramids	-	1,051,531	0
	tetras	-	6,378,624	0
	pentas	-	5,516,910	0
	hexas	-	3,367,500	0
	polyhedrals	-	0	9,970,230
	Total	**-**	**16,314,565**	**9,970,230**

Table 4.2: Number of cells: Case 2.

	Element type	Surface mesh	Volume mesh	Volume mesh (Polyhedrals)
No. Shell elements	trias	970,058	1,786,267	0
	quads	0	17,521	0
	polygons	0	0	1,415,604
	Total	**970,058**	**1,803,788**	**1,415,604**
No. Volume elements	pyramids	-	1,187,549	0
	tetras	-	7,371,853	0
	pentas	-	6,548,424	0
	hexas	-	3,633,511	0
	polyhedrals	-	0	11,161,882
	Total	**-**	**18,741,337**	**11,161,882**

Table 4.3: Number of cells: Case 3.

The quality of the final mesh is highly connected to the quality of the surface mesh, thus the surface mesh is the one with the highest importance and one should put a lot of effort into it. A detailed presentation of the different surface mesh types and cell sizes follows in Appendix B.

4.1.3 Identification of the physical and chemical phenomena that need to be modelled

All the cases are modeled in 3D. In the mean time, the flow is considered incompressible with a constant density $\rho = 1025 kg/m^3$. Finally, the turbulent flow is modelled since turbulence has a large contribution to the flow.

4.1.4 Definition of the fluid properties

All the fluid properties such as density, pressure and velocity are defined in space (i.e. x, y, z-directions) and in time during the transient simulations. Steady state MRF simulations are used for the initialisation of the flow properties and transient SMI simulations follow in order to have higher accuracy. The results that are finally used are derived from the transient SMI simulations.

4.1.5 Definition of the boundary conditions

Initial step before applying the boundary conditions in OpenFOAM v1806 is to break the boundaries into **patches**, where one patch might include several boundary surfaces. A **geometric patch type** is then selected for each patch. The patches are located in the *<case>/constant/polyMesh/boundary* directory (OpenCFD Ltd, 2018). It should be mentioned that the polyMesh folder is created during the grid generation step by ANSA pre-processor.

Second step is to define the **boundary conditions** for each field that needs to be solved (i.e. velocity U, pressure p). The boundary conditions are located in the *<case>/0/** directory (e.g. *<case>/0/U*).

Final step is to define the **wall functions** for the turbulence models (i.e. turbulent kinetic energy k, dissipation rate of turbulent kinetic energy ε, specific dissipation rate of turbulent energy ω, turbulent viscosity field ν_t). The wall functions are treated in the same way as the boundary conditions, which means that the wall functions are also applied on individual patches. The wall functions are located in the *<case>/0/** directory (e.g. *<case>/0/nut*).

A detailed presentation of the different patches, geometric patch types, boundary conditions and wall functions that are used within this project study follows. The patches that are demonstrated in *Table 4.4*, *Table 4.5* and *Table 4.6* that include an asterisk (*) are split into more components, thus more patches in the actual OpenFOAM case setup files. More specifically, the following patches are split into:

- Blades
  - Blade 000
  - Blade 090
  - Blade 180
  - Blade 270
- Nozzle
  - Nozzle inner
  - Nozzle outer
- Shaft
  - Shaft inner
  - Shaft outer

- Azimuth
  - Azimuth body (MTA) inner
  - Azimuth body (MTA) outer
  - Stay right
  - Stay left
- Domain (in Case 3)
  - Domain inner
  - Domain outer
  - Domain top
  - Domain bottom

It should be mentioned that the naming of the patches is free of choice. On the other hand, the geometric patch types, boundary conditions and wall functions should be set in openFOAM as they appear in the following tables. A thorough explanation of the patch types and the wall functions is given by F. Liu (2017) for a full understanding of the wall functions.

The boundary conditions used within this project are explained in the following list (OpenCFD Ltd, 2018):

- **calculated:** This boundary condition is not evaluated. It is rather assumed that the value is assigned vie field assignment.
- **fixedValue:** This boundary condition sets a fixed value constraint.
- **zeroGradient:** This boundary condition sets a zero gradient condition from the patch internal field to the patch faces.
- **cyclicAMI:** This boundary condition determines a cyclic condition between a pair of boundaries where communication between the patches is achieved using an Arbitrary Mesh Interpolation (AMI).
- **movingWallVelocity:** This boundary condition sets a velocity condition for cases with moving walls.
- **slip:** This boundary condition sets a slip constraint.

Finally, the patches, patch types, boundary conditions and wall functions are presented in *Table 4.4*, *Table 4.5* and *Table 4.6*. Here it should be mentioned that the slip boundary condition is the same as symmetry boundary condition for the fields over which the boundaries are imposed. However, symmetry boundary condition alters also the fields internal to the solvers. Thus, a slip condition is used.

Patch	**Geometric patch type**	**Boundary conditions**		
	boundary	**U**	**p**	**p_rgh**
Inlet	patch	fixedValue	zeroGradient	zeroGradient
Outlet	patch	zeroGradient	fixedValue	fixedValue
Domain	patch	slip	slip	slip
Blades*	wall	movingWallVelocity	zeroGradient	zeroGradient
Hub	wall	movingWallVelocity	zeroGradient	zeroGradient
Nozzle*	wall	fixedValue	zeroGradient	zeroGradient
Shaft*	wall	fixedValue	zeroGradient	zeroGradient
cyclic_half0	cyclicAMI	cyclicAMI	cyclicAMI	cyclicAMI
cyclic_half1	cyclicAMI	cyclicAMI	cyclicAMI	cyclicAMI

Patch	**Wall functions**				
	nut (ν_t)	**epsilon** (ε)	**k** (κ)	**omega** (ω)	**alpha.water**
Inlet	calculated	fixedValue	fixedValue	fixedValue	fixedValue
Outlet	calculated	zeroGradient	zeroGradient	zeroGradient	zeroGradient
Domain	slip	slip	slip	slip	slip
Blades*	nutUSpaldingWallFunction	epsilonWallFunction	kqRWallFunction	omegaWallFunction	zeroGradient
Hub	nutUSpaldingWallFunction	epsilonWallFunction	kqRWallFunction	omegaWallFunction	zeroGradient
Nozzle*	nutUSpaldingWallFunction	epsilonWallFunction	kqRWallFunction	omegaWallFunction	zeroGradient
Shaft*	nutUSpaldingWallFunction	epsilonWallFunction	kqRWallFunction	omegaWallFunction	zeroGradient
cyclic_half0	cyclicAMI	cyclicAMI	cyclicAMI	cyclicAMI	cyclicAMI
cyclic_half1	cyclicAMI	cyclicAMI	cyclicAMI	cyclicAMI	cyclicAMI

Table 4.4: Presentation of the boundary conditions: Case 1.

Patch	**Geometric patch type**	**Boundary conditions**		
	boundary	**U**	**p**	**p_rgh**
Inlet	patch	fixedValue	zeroGradient	zeroGradient
Outlet	patch	zeroGradient	fixedValue	fixedValue
Domain	patch	slip	slip	slip
Blades*	wall	movingWallVelocity	zeroGradient	zeroGradient
Hub	wall	movingWallVelocity	zeroGradient	zeroGradient
Nozzle*	wall	fixedValue	zeroGradient	zeroGradient
Azimuth*	wall	fixedValue	zeroGradient	zeroGradient
Lid	wall	fixedValue	zeroGradient	zeroGradient
cyclic_half0	cyclicAMI	cyclicAMI	cyclicAMI	cyclicAMI
cyclic_half1	cyclicAMI	cyclicAMI	cyclicAMI	cyclicAMI

Patch	**Wall functions**				
	nut (ν_t)	**epsilon** (ε)	**k** (κ)	**omega** (ω)	**alpha.water**
Inlet	calculated	fixedValue	fixedValue	fixedValue	fixedValue
Outlet	calculated	zeroGradient	zeroGradient	zeroGradient	zeroGradient
Domain	slip	slip	slip	slip	slip
Blades*	nutUSpaldingWallFunction	epsilonWallFunction	kqRWallFunction	omegaWallFunction	zeroGradient
Hub	nutUSpaldingWallFunction	epsilonWallFunction	kqRWallFunction	omegaWallFunction	zeroGradient
Nozzle*	nutUSpaldingWallFunction	epsilonWallFunction	kqRWallFunction	omegaWallFunction	zeroGradient
Azimuth*	nutUSpaldingWallFunction	epsilonWallFunction	kqRWallFunction	omegaWallFunction	zeroGradient
Lid	nutUSpaldingWallFunction	epsilonWallFunction	kqRWallFunction	omegaWallFunction	zeroGradient
cyclic_half0	cyclicAMI	cyclicAMI	cyclicAMI	cyclicAMI	cyclicAMI
cyclic_half1	cyclicAMI	cyclicAMI	cyclicAMI	cyclicAMI	cyclicAMI

Table 4.5: Presentation of the boundary conditions: Case 2.

Patch	**Geometric patch type**	**Boundary conditions**		
	boundary	**U**	**p**	**p_rgh**
Inlet	patch	fixedValue	zeroGradient	zeroGradient
Outlet	patch	zeroGradient	fixedValue	fixedValue
Domain*	patch	slip	slip	slip
Blades*	wall	movingWallVelocity	zeroGradient	zeroGradient
Hub	wall	movingWallVelocity	zeroGradient	zeroGradient
Nozzle*	wall	fixedValue	zeroGradient	zeroGradient
Azimuth*	wall	fixedValue	zeroGradient	zeroGradient
Cone	wall	fixedValue	zeroGradient	zeroGradient
Hull	wall	fixedValue	zeroGradient	zeroGradient
Skeg	wall	fixedValue	zeroGradient	zeroGradient
cyclic_half0	cyclicAMI	cyclicAMI	cyclicAMI	cyclicAMI
cyclic_half1	cyclicAMI	cyclicAMI	cyclicAMI	cyclicAMI

Patch	**Wall functions**				
	nut (ν_t)	**epsilon** (ε)	**k** (κ)	**omega** (ω)	**alpha.water**
Inlet	calculated	fixedValue	fixedValue	fixedValue	fixedValue
Outlet	calculated	zeroGradient	zeroGradient	zeroGradient	zeroGradient
Domain*	slip	slip	slip	slip	slip
Blades*	nutUSpaldingWallFunction	epsilonWallFunction	kqRWallFunction	omegaWallFunction	zeroGradient
Hub	nutUSpaldingWallFunction	epsilonWallFunction	kqRWallFunction	omegaWallFunction	zeroGradient
Nozzle*	nutUSpaldingWallFunction	epsilonWallFunction	kqRWallFunction	omegaWallFunction	zeroGradient
Azimuth*	nutUSpaldingWallFunction	epsilonWallFunction	kqRWallFunction	omegaWallFunction	zeroGradient
Cone	nutUSpaldingWallFunction	epsilonWallFunction	kqRWallFunction	omegaWallFunction	zeroGradient
Hull	nutUSpaldingWallFunction	epsilonWallFunction	kqRWallFunction	omegaWallFunction	zeroGradient
Skeg	nutUSpaldingWallFunction	epsilonWallFunction	kqRWallFunction	omegaWallFunction	zeroGradient
cyclic_half0	cyclicAMI	cyclicAMI	cyclicAMI	cyclicAMI	cyclicAMI
cyclic_half1	cyclicAMI	cyclicAMI	cyclicAMI	cyclicAMI	cyclicAMI

Table 4.6: Presentation of the boundary conditions: Case 3.

4.2 Solving

4.2.1 Integration of the governing equations of the flow over the finite control volumes of the domain

The numerical method used to model the flow and capture the effects of turbulence is the RANS model. Moreover, the Menter SST $\kappa - \omega$ turbulent model is used to model the boundary layer and the effect of the unresolved fully turbulent regions far from the wall. Both RANS and Menter SST $\kappa - \omega$ model are specified in *<case>/constant/RASProperties* directory.

4.2.2 Discretisation of the integrated equations into algebraic equations

The numerical schemes used in this project are:

- **Interpolation schemes:** Central differencing (i.e. *linear* in OpenFOAM) is used, which is a second order, unbounded scheme. Interpolation schemes are specified in *<case>/system/fvSchemes/interpolationSchemes*.
- **Surface normal gradient schemes:** Limited explicit non-orthogonal correction (i.e. *limited corrected* in OpenFOAM) is used. Surface normal gradient schemes are specified in *<case>/system/fvSchemes/snGradSchemes*.
- **Gradient schemes:** Gaussian integration with central differencing (i.e. *Gauss linear* in OpenFOAM) is used, which is a second order, unbounded scheme. Gradient schemes are specified in *<case>/system/fvSchemes/gradSchemes*.
- **Laplacian schemes:** Gaussian integration with central differencing and a blend of corrected and uncorrected numerical behaviour (i.e. *Gauss linear limited corrected* in OpenFOAM) is used. Laplacian schemes are specified in *<case>/system/fvSchemes/laplacianSchemes*.
- **Divergence schemes:**
  - Gaussian integration with upwind differencing
    (i.e. *Gauss upwind* in OpenFOAM), which is a first order, bounded scheme. This scheme is used for the $\nabla \cdot (\rho U \kappa)$ term, represented by the div(phi,k) and for the $\nabla \cdot (\rho U \omega)$ term, represented by the div(phi,omega).
  - Gaussian integration with linear upwind differencing
    (i.e. *Gauss linearUpwind* in OpenFOAM), which is a first/second order, bounded scheme. This scheme is used for the $\nabla \cdot (\rho U U)$ term, represented by the div(phi,U).

  Divergence schemes are specified in *<case>/system/fvSchemes/divSchemes*.
- **Time schemes:**
  Euler (i.e. *Euler* in OpenFOAM) is used in transient simulations, which is a first order, bounded and implicit scheme. Time schemes are specified in *<case>/system/fvSchemes/ddtSchemes*.

4.2.3 Solving of the algebraic equations by the use of iterative method

The algorithms used in this project are:

- **SIMPLE** for the steady state MRF simulations,
- **PIMPLE** for the transient SMI simulations.

The following iterative linear solvers are used for both the steady state MRF and transient SMI simulations:

- **Generalised geometric-algebraic multi-grid (GAMG)** (i.e. *GAMG* in OpenFOAM) with a **Gauss-Seidel** smoother (i.e. *GaussSeidel* in OpenFOAM) for the pressure p, which is specified in *<case>/system/fvSolution/solvers/p*.
- **Smoother solver** (i.e. *smoothSolver* in OpenFOAM) with a **symmetric Gauss-Seidel** smoother (i.e. *symGaussSeidel* in OpenFOAM) for the velocity U, the turbulent kinetic energy k, the dissipation rate of turbulent kinetic energy ε and the specific dissipation rate ω, which is specified in *<case>/system/fvSolution/solvers/<U|k|...>*.

while the transient simulations also need:

- **Generalised geometric-algebraic multi-grid (GAMG)** with a **Diagonal incomplete-Cholesky with Gauss-Seidel (symmetric)** smoother (i.e. *DICGaussSeidel* in OpenFOAM) for the pressure correction, which is specified in *<case>/system/fvSolution/solvers/"(pcorr.*)"*.
- **Generalised geometric-algebraic multi-grid** with a **Diagonal incomplete-Cholesky with Gauss-Seidel (symmetric)** smoother for the pressure range that matters, thus the pressure without the hydrostatic pressure which is formulated as $p\_rgh = p - \rho gh$. GAMG is specified in *<case>/system/fvSolution/solvers/p_rgh*.

Moreover, two types of modelling regarding the mesh take place within the project:

- MRF, which is specified in *<case>/system/fvOptions*.
- SMI, which is specified in *<case>/constant/dynamicMeshDict*.

4.3 Post-processing

4.3.1 Visualization of the simulation results

Initial step of the post-processing is to look at flow variable fields, which are a results of the CFD simulations. The following flow fields are observed thoroughly in ParaView v.5.6.0:

- Velocity field U
- Pressure field p
- The turbulent kinetic energy field k
- The specific dissipation rate of turbulent energy field ω

Next step is to plot the convergence of the forces F and moments M of all the cases

and for each advance coefficient J and part (e.g. blades, nozzle, hull) that are located in *<case>/postProcessing/<part>/0/forces.dat*. This is done in MATLAB R2018b.

4.3.2 Process of the numerical results

A mean value of the forces and moments of the last 720 iterations, which is equivalent to the last two full revolutions of the propeller of the total number of ten revolutions, of each case, advance coefficient J and part that are mentioned above is calculated. For a better understanding, these mean values are demonstrated below:

- Mean force $\overline{F}$, which is either expresses as mean thrust $\overline{T}$ or mean resistance $\overline{R}$,
- Mean moment $\overline{M}$, which is expressed as mean torque $\overline{Q}$.

Later on, by the use of these mean values the following variables are calculated:

- Mean thrust coefficient $\overline{K_T}$,
- Mean torque coefficient $10 \cdot \overline{K_Q}$,
- Mean open water efficiency $\overline{\eta_0}$.

Note: Due to simplification purposes, from now on all the forces, moments, coefficients and open water efficiencies will not be referred as mean values and the overline of these symbols will be neglected, even though they are all derived from a mean value.

The **thrust deduction factors** t are then calculated in order to describe the increase of the resistance due to the suction of the propeller, determine the generated thrust and obtain the different contributions of the gear case housing and the hull from a thrust perspective:

- Case 1

$$t = \frac{0}{T_{blades} + T_{nozzle}} = 0 \tag{4.1}$$

- Case 2

$$t = \frac{-R_{gear\_case\_housing}}{T_{blades} + T_{nozzle}} \tag{4.2}$$

- Case 3

$$t = \frac{-(R_{gear\_case\_housing} + R_{hull})}{T_{blades} + T_{nozzle}} \tag{4.3}$$

Next step is to calculate the **merit coefficients** m_c, which are a replacement of the total propulsive efficiency η_D:

- Case 1

$$m_c = \frac{[(K_{Tblades} + K_{Tnozzle})/\pi]^{3/2}}{K_{Qblades}} \tag{4.4}$$

- Case 2

$$m_c = \frac{[(K_{Tblades} + K_{Tnozzle} + K_{Tgear\_case\_housing})/\pi]^{3/2}}{K_{Qblades}} \tag{4.5}$$

- Case 3 (excluding hull)

$$m_c = \frac{[(K_{Tblades} + K_{Tnozzle} + K_{Tgear\_case\_housing})/\pi]^{3/2}}{K_{Qblades}} \tag{4.6}$$

- Case 3 (including hull)

$$m_c = \frac{[(K_{Tblades} + K_{Tnozzle} + K_{Tgear\_case\_housing} + K_{Thull})/\pi]^{3/2}}{K_{Qblades}} \tag{4.7}$$

Here it should be mentioned that the merit coefficient of Case 3 is calculated by both including and excluding the contribution of the hull. This is done in order to obtain the flow field that is derived from the case simulation with the hull (i.e. Case 3) but also at the same time to include or exclude the contribution of the hull itself.

Then, the **open water characteristic diagrams** for all the cases are generated. Both the MRF and SMI simulation results that have been performed in OpenFOAM are plotted for comparison and evaluation purposes.

A complete open water diagram is plotted for Case 1 with both MRF and SMI results in order to get an overall idea of the behaviour of this specific arrangement in bollard pull and free sailing conditions and in both steady state and transient approaches. The values that are plotted are the following:

- MRF results for $J = 0.00, 0.10, 0.20, 0.30, 0.40, 0.50, 0.60, 0.65, 0.70, 0.75, 0.80$ $0.85, 0.90, 1.00$,
- SMI results for $J = 0.00, 0.20, 0.40, 0.60, 0.80$.

The SMI results are chosen for $J = 0.00$ and the MRF results for all the other J values and a combined MRF-SMI open water characteristics diagram is created. This diagram, that from now on is referred to as "hybrid diagram", is later used as Case 1.

A complete open water diagram is also plotted for Case 2 but this time with only SMI results in order to get an overall idea of the behaviour of this specific arrangement in bollard pull and free sailing conditions and in transient approach. The values that are plotted are the following:

- SMI results for $J = 0.00, 0.20, 0.40,\ 0.60, 0.70, 0.80, 0.90, 1.00$.

In the end, only the values for $J = 0.00$ are plotted for Case 3 with SMI results but this time with the only focus in bollard pull condition and in transient approach. Finally, the open water case (i.e. Case 1) is compared with the **Wageningen CD Series** in three different ways (i.e. brake power similarity, thrust power similarity and geometrical similarity) in order to develop an evaluation tool which can be used in the future in order to evaluate the early stages of a project.

It should be noted that all the above calculations and plots are done in MATLAB.

4.4 System used to run OpenFOAM

A High-Performance Computing (HPC) system is used since parallel processing is needed. The CFD simulations within this project are run on a cluster owned by *Caterpillar Inc.* The simulations are decomposed into 144 cores and computed in parallel, something which is known as domain decomposition in OpenFOAM.

Through the domain decomposition, the geometry and the flow fields are split and then distributed into separate processors, which are then separately solved. After the completion of the simulation the decomposed cases are reconstructed into one case.

The steady state simulations take about two hours to be completed while the transient simulations are run overnight.

5

Results and data analysis

In this chapter, the results of all the CFD simulations are presented. In addition, discussion of the results and data analysis is achieved. In the first section of this chapter a data analysis in both free sailing and bollard pull conditions is achieved in order to get an overall idea of the behaviour of all the cases. The hydrodynamic interactions are presented in the second section only in bollard pull condition since this is the main focus of this study project.

5.1 Data analysis in free sailing and bollard pull conditions

The performance characteristics of a propeller or generally a propulsion unit are usually presented by open water characteristic diagrams. Thus, this type of diagrams are used in order to conduct various comparisons.

5.1.1 Comparison of MRF/SMI

In this section, a comparison of the two different modelling methodologies used within this project is achieved. For this type of comparison, results from both MRF and SMI of Case 1 have been used.

In *Figure 5.1*, two open water characteristic diagrams derived from the SMI (see *Table 5.2*) and MRF (see *Table 5.3*) results are presented. Since this comparison is done only for Case 1, the hydrodynamic coefficients discussed are the thrust coefficients of the blades $K_{Tblades}$ and nozzle $K_{Tnozzle}$, the torque coefficient of the blades $10 \cdot K_{Qblades}$ and the open water efficiency η_0. Moreover, identical rotational speed $n = 191rpm$ for all the advance coefficients J has been used. In this way, the difference of the resulting thrust and torque can be observed.

In *Figure 5.2*, the already mentioned hybrid open water characteristics diagram that combines the SMI results for $J = 0.00$ and the MRF results for $J = 0.10 - 1.00$ is presented.

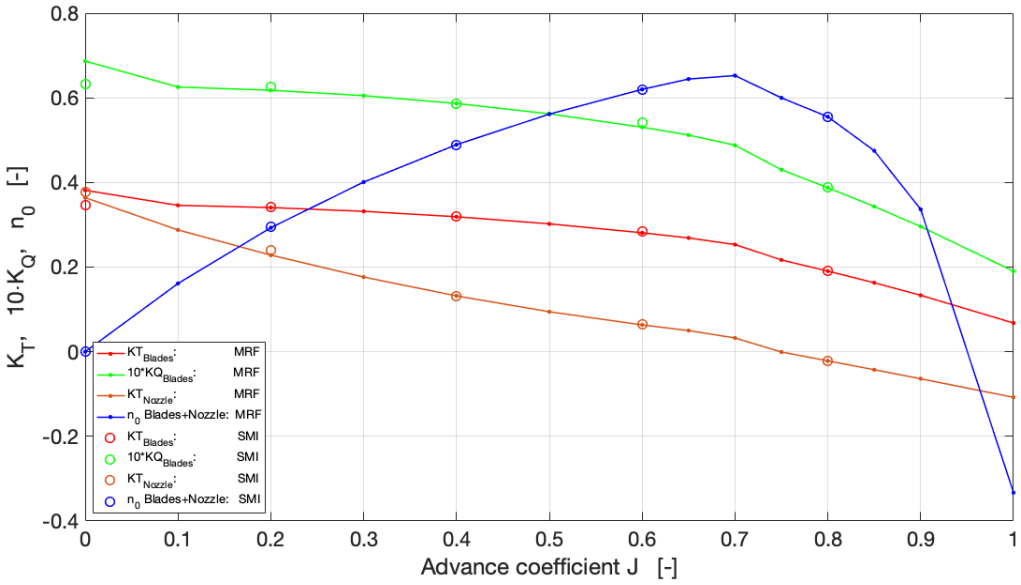

Figure 5.1: Open water characteristics diagram: MRF/SMI comparison of Case 1.

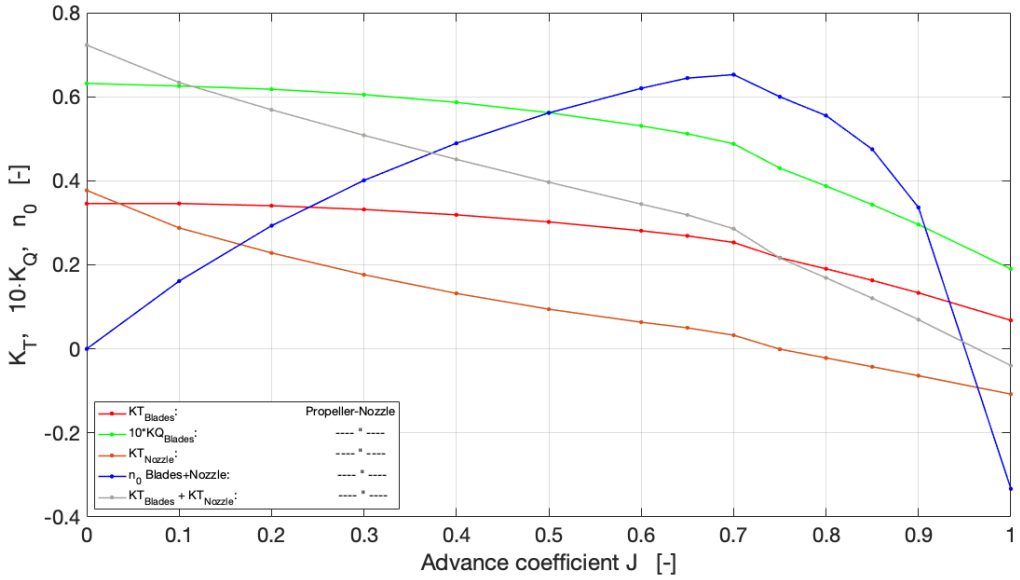

Figure 5.2: Open water characteristics diagram: Hybrid MRF/SMI diagram of Case 1.

The values of the hybrid diagram are presented in *Table 5.1.* The complete results are fully presented in *Table 5.2* for the SMI and in *Table 5.3* for the MRF.

	Blades				Nozzle				Open water efficiency
J [−]	T [kN]	K_T [-]	Q [kNm]	$10K_Q$ [-]	T [kN]	K_T [-]	Q [kNm]	$10K_Q$ [-]	η_0 [-]
0.00	190.98	0.3460	94.15	0.6317	208.20	0.3772	-0.09	-0.0006	0.0000
0.10	190.97	0.3460	93.22	0.6255	158.92	0.2879	-0.14	-0.0009	0.1613
0.20	188.07	0.3407	92.10	0.6179	126.03	0.2283	-0.13	-0.0009	0.2931
0.30	183.15	0.3318	90.20	0.6052	97.40	0.1764	-0.12	-0.0008	0.4010
0.40	176.08	0.3190	87.44	0.5867	72.84	0.1320	-0.11	-0.0008	0.4893
0.50	166.82	0.3022	83.78	0.5621	52.16	0.0945	-0.10	-0.0007	0.5616
0.60	155.19	0.2811	79.09	0.5306	35.00	0.0634	-0.08	-0.0005	0.6201
0.65	148.43	0.2689	76.31	0.5120	27.61	0.0500	-0.07	-0.0005	0.6444
0.70	139.82	0.2533	72.72	0.4879	17.96	0.0325	-0.06	-0.0004	0.6526
0.75	119.69	0.2168	64.10	0.4301	-0.37	-0.0007	-0.05	-0.0004	0.5999
0.80	105.18	0.1905	57.75	0.3875	-11.90	-0.0216	-0.05	-0.0003	0.5552
0.85	89.97	0.1630	51.14	0.3431	-23.47	-0.0425	-0.06	-0.0004	0.4749
0.90	73.63	0.1334	44.09	0.2958	-35.27	-0.0639	-0.06	-0.0004	0.3365
1.00	37.47	0.0679	28.35	0.1902	-59.44	-0.1077	-0.06	-0.0004	0.3330

Table 5.1: Hybrid MRF/SMI results: Case 1.

The total forces and moments extracted from the OpenFOAM post-processing simulation files for both MRF and SMI, in bollard pull condition (i.e. $J = 0.00$) and for all the three directions are presented in the following figures.

x-direction

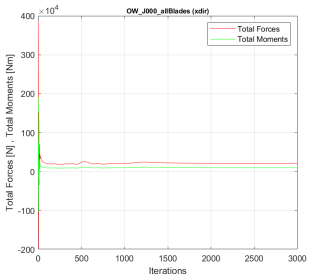

(a) Propeller blades.

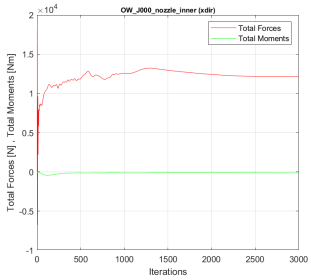

(b) Inner part of the nozzle.

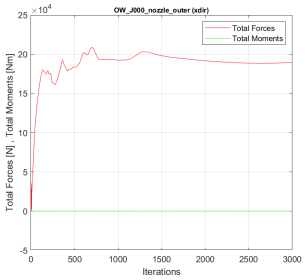

(c) Outer part of the nozzle.

Figure 5.3: MRF simulation of Case 1 at $J = 0.00$.

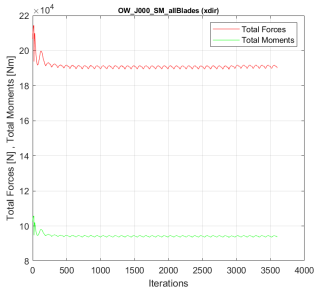

(a) Propeller blades.

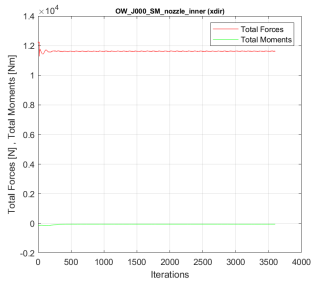

(b) Inner part of the nozzle.

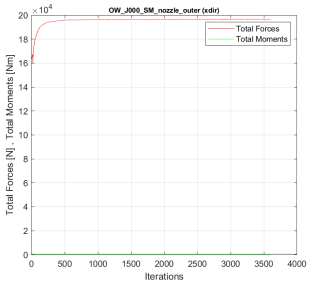

(c) Outer part of the nozzle.

Figure 5.4: SMI simulation of Case 1 at $J = 0.00$.

y-direction

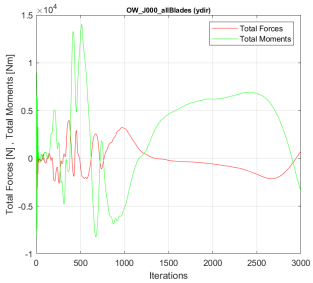

(a) Propeller blades.

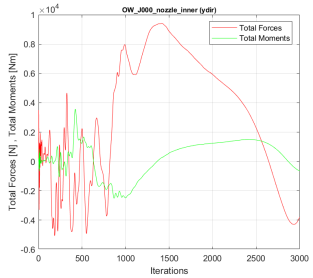

(b) Inner part of the nozzle.

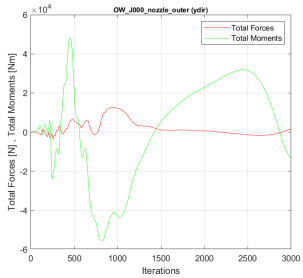

(c) Outer part of the nozzle.

Figure 5.5: MRF simulation of Case 1 at $J = 0.00$.

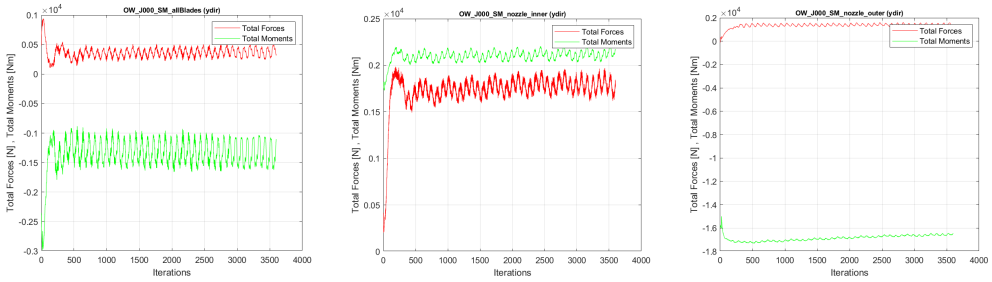

(a) Propeller blades.

(b) Inner part of the nozzle.

(c) Outer part of the nozzle.

Figure 5.6: SMI simulation of Case 1 at $J = 0.00$.

z-direction

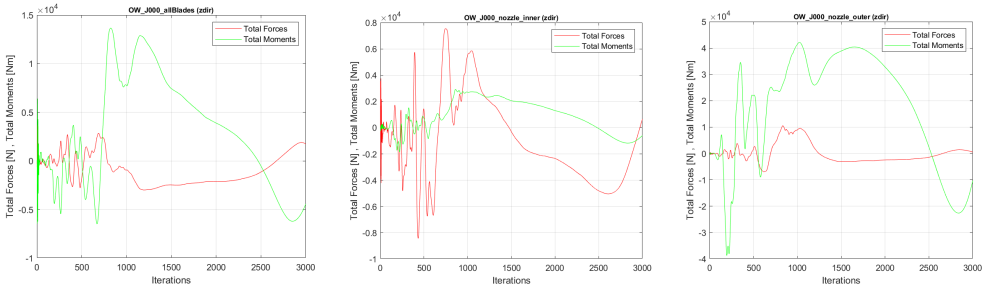

(a) Propeller blades.

(b) Inner part of the nozzle.

(c) Outer part of the nozzle.

Figure 5.7: MRF simulation of Case 1 at $J = 0.00$.

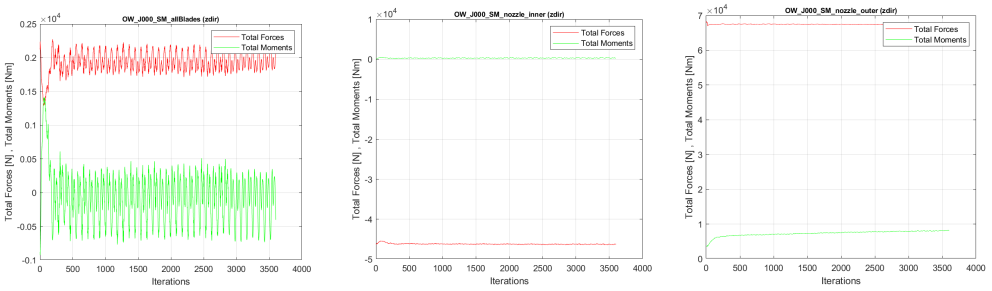

(a) Propeller blades.

(b) Inner part of the nozzle.

(c) Outer part of the nozzle.

Figure 5.8: SMI simulation of Case 1 at $J = 0.00$.

Looking at *Figure 5.1* and by comparing the complete results for SMI in *Table 5.2* and the complete results for MRF in *Table 5.3*, it is obvious that most of the MRF results are following the SMI results. However, a big difference is observed at $J = 0.00$ that bollard pull condition occurs. Observing the convergence plots above, it is obvious that the x-direction results seem to be converged for both MRF and SMI. However, the MRF results for y-direction and z-direction are not converged while the SMI results are. Moreover, it should be mentioned that an oscillation of the results appears for the SMI. Nevertheless, this oscillation is constant and thus an average value of the last 720 iterations is taken.

Considering that the results for bollard pull condition seem more realistic by taking into account the CFD results of other similar studies and by observing the convergence of SMI and the convergence issues of MRF, the already mentioned statement that the **transient SMI methodology gives much more accurate results compared to the steady state MRF** for low J values can be supported. Meanwhile, the results for medium J values computed with the MRF approach are quite reasonable.

Since the transient SMI methodology gives much more accurate results, the ideal would be to run every simulation with SMI. On the other hand, SMI is much more computationally expensive compared to MRF.

	Blades				Nozzle				Open water efficiency
J [−]	T [kN]	K_T [-]	Q [kNm]	$10K_Q$ [-]	T [kN]	K_T [-]	Q [kNm]	$10K_Q$ [-]	η_0 [-]
0.00	190.98	0.3460	94.15	0.6317	208.20	0.3772	-0.09	-0.0006	0.0000
0.20	188.78	0.3420	93.29	0.6259	132.26	0.2396	-0.12	-0.0008	0.2958
0.40	176.08	0.3190	87.44	0.5867	72.84	0.1320	-0.11	-0.0008	0.4893
0.60	157.22	0.2848	80.61	0.5408	36.29	0.0657	-0.09	-0.0006	0.6190
0.80	105.18	0.1905	57.75	0.3875	-11.90	-0.0216	-0.05	-0.0003	0.5552

Table 5.2: SMI results: Case 1 (see *Figure 5.2*).

	Blades				Nozzle				Open water efficiency
J [−]	T [kN]	K_T [-]	Q [kNm]	$10K_Q$ [-]	T [kN]	K_T [-]	Q [kNm]	$10K_Q$ [-]	η_0 [-]
0.00	210.64	0.3816	102.36	0.6868	200.99	0.3641	-0.12	-0.0008	0.0000
0.10	190.97	0.3460	93.22	0.6255	158.92	0.2879	-0.14	-0.0009	0.1613
0.20	188.07	0.3407	92.10	0.6179	126.03	0.2283	-0.13	-0.0009	0.2931
0.30	183.15	0.3318	90.20	0.6052	97.40	0.1764	-0.12	-0.0008	0.4010
0.40	176.08	0.3190	87.44	0.5867	72.84	0.1320	-0.11	-0.0008	0.4893
0.50	166.82	0.3022	83.78	0.5621	52.16	0.0945	-0.10	-0.0007	0.5616
0.60	155.19	0.2811	79.09	0.5306	35.00	0.0634	-0.08	-0.0005	0.6201
0.65	148.43	0.2689	76.31	0.5120	27.61	0.0500	-0.07	-0.0005	0.6444
0.70	139.82	0.2533	72.72	0.4879	17.96	0.0325	-0.06	-0.0004	0.6526
0.75	119.69	0.2168	64.10	0.4301	-0.37	-0.0007	-0.05	-0.0004	0.5999
0.80	105.18	0.1905	57.75	0.3875	-11.90	-0.0216	-0.05	-0.0003	0.5552
0.85	89.97	0.1630	51.14	0.3431	-23.47	-0.0425	-0.06	-0.0004	0.4749
0.90	73.63	0.1334	44.09	0.2958	-35.27	-0.0639	-0.06	-0.0004	0.3365
1.00	37.47	0.0679	28.35	0.1902	-59.44	-0.1077	-0.06	-0.0004	-0.3330

Table 5.3: MRF results: Case 1 (see *Figure 5.2*).

5.1.2 Comparison of Case 1/Case 2

In *Figure 5.9*, two open water characteristic diagrams derived from Case 1 and Case 2 are presented. The thrust coefficient of the gear case housing $K_{Tgear\_case\_housing}$ is also included among the other coefficients. Moreover, as in the previous section identical rotational speed $n = 191rpm$ for all the advance coefficients J has been used.

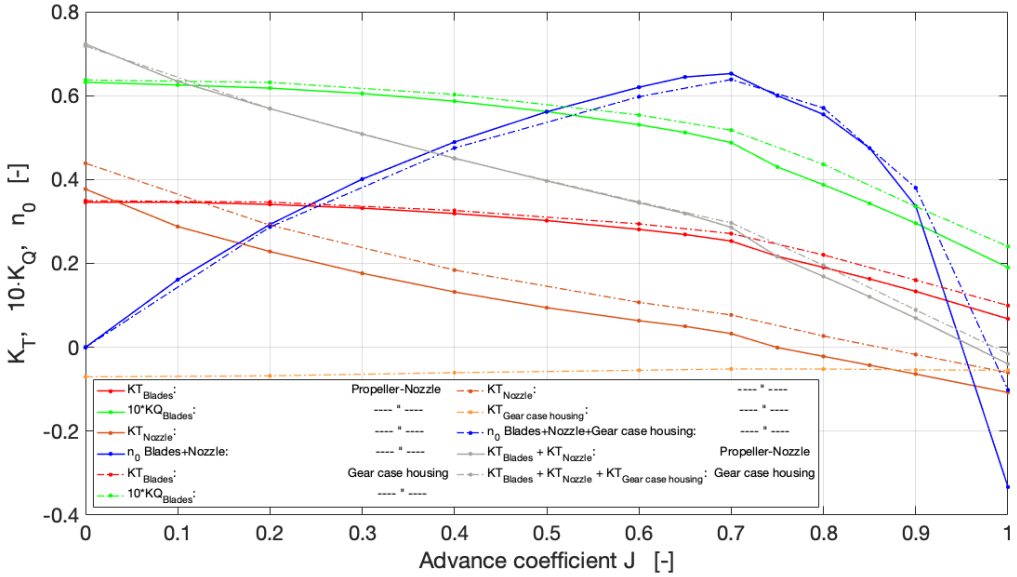

Figure 5.9: Open water characteristics diagram: Case 1/Case 2 comparison.

The values of Case 2 are presented in *Table 5.4*. It should be mentioned that while the hydrodynamic coefficients of Case 1 are derived from the hybrid MRF/SMI results, the coefficients of Case 2 are obtained only from the SMI results since only SMI was used in this case in order to have slightly better accuracy for the gear case housing within all the open water diagram.

Looking at *Figure 5.9*, it is noticed that the **propeller thrust** is really similar in both cases for $J = 0.00 - 0.40$ while the difference starts to increase after this point. For $J = 0.70 - 1.00$ the thrust is much higher for Case 2. The difference of the **propeller torque** appears to be quite large between $J = 0.00 - 0.40$ while after this point the difference gets even larger with the largest difference occurring between $J = 0.70 - 1.00$. Looking at the **nozzle thrust**, it is clear that in Case 2 the thrust is much higher than in Case 1 within the whole diagram. Moreover, it can be seen that the **gear case housing thrust** remains constant within the whole diagram. Since the thrust is having a negative value, it is considered as resistance instead. Finally, it is observed that the **open water efficiency** is lower for Case 2 between $J = 0.00 - 0.70$. Looking specifically at $J = 0.00$, the open water efficiency looses its meaning (i.e. open water efficiency is always zero since the velocity of the ship is zero). In this moment, the **merit coefficient** is introduced, however this is further discussed in Section 5.2.

	Blades				Nozzle				Gear Case Housing				Open water efficiency
J [−]	T [kN]	K_T [-]	Q [kNm]	$10K_Q$ [-]	T [kN]	K_T [-]	Q [kNm]	$10K_Q$ [-]	T [kN]	K_T [-]	Q [kNm]	$10K_Q$ [-]	η_0 [-]
0.00	193.00	0.3496	94.99	0.6373	242.24	0.4388	-0.10	-0.0007	-38.81	-0.0703	-1.10	-0.0074	0.0000
0.20	191.09	0.3462	94.14	0.6316	160.72	0.2912	-0.10	-0.0007	-37.56	-0.0680	1.70	0.0114	0.2869
0.40	180.09	0.3262	89.84	0.6028	101.65	0.1841	-0.08	-0.0005	-33.40	-0.0605	0.49	0.0033	0.4751
0.60	162.42	0.2942	82.57	0.5540	59.15	0.1072	-0.06	-0.0004	-30.25	-0.0548	-2.72	-0.0183	0.5974
0.70	149.66	0.2711	77.14	0.5176	42.56	0.0771	-0.05	-0.0003	-28.49	-0.0516	-4.50	-0.0302	0.6384
0.80	121.62	0.2203	65.00	0.4361	14.84	0.0269	-0.07	-0.0005	-28.56	-0.0517	-3.09	-0.0207	0.5707
0.90	88.37	0.1601	50.03	0.3357	-9.49	-0.0172	-0.07	-0.0005	-29.70	-0.0538	-2.64	-0.0177	0.3801
1.00	55.02	0.0997	35.85	0.2405	-33.30	-0.0603	-0.13	-0.0009	-30.21	-0.0547	-3.53	-0.0237	-0.1018

Table 5.4: SMI results: Case 2.

In *Figure 5.10*, the pressure distribution in bollard pull condition of Case 1 is presented. The pressure distribution seems normal with higher pressure at the pressure side and lower pressure at the suction side. Looking at *Figure 5.11* that presents the velocity field of Case 1, it is clearly demonstrated by the velocity magnitude field that the flow is straight. A small decrease of the velocities in the centerline is observed, which is due to the hub that is blocking the flow.

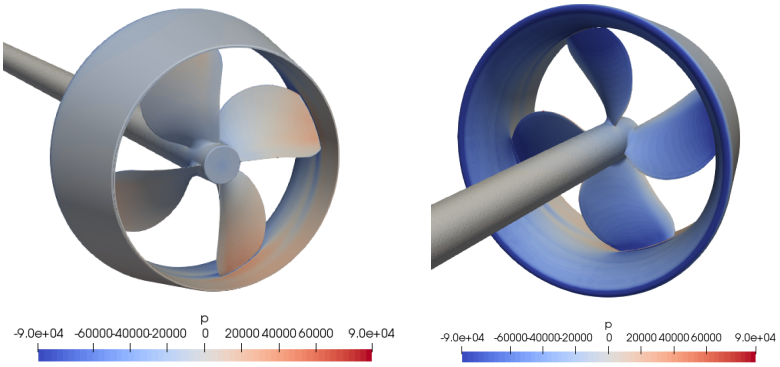

(a) Pressure side. **(b)** Suction side.

Figure 5.10: Pressure distributions at $J = 0.00$: Case 1.

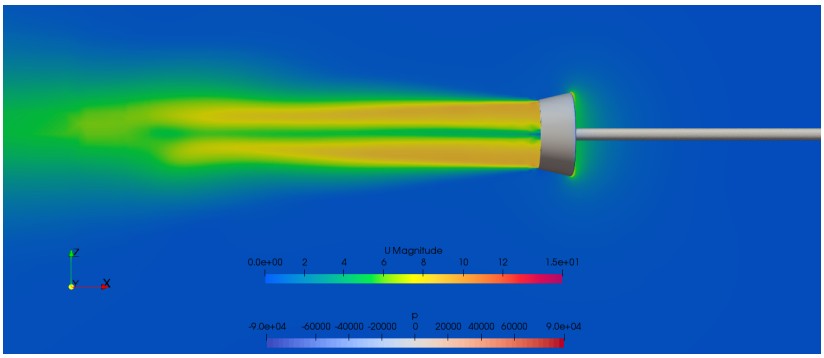

Figure 5.11: Velocity field at $J = 0.00$: Case 1.

In *Figure 5.12*, the pressure distribution of Case 2 is presented. The pressure distribution seems normal. Furthermore, it is observed that Case 2 has an inflow with lower pressure compared to Case 1 due to the gear case housing that is blocking the flow. Thus, the pressure difference in Case 2 is higher, which indicates higher acceleration of water from the pressure side to the suction side (i.e higher advance velocity). As a result, the higher thrust power that is created from the propeller towards the outflow is explained. Looking at *Figure 5.13* that presents the velocity field of Case 2, it is observed that some fluctuations have been introduced to the flow. Most likely this result occurs due to the change of the quality of the mesh within this region. However, further investigation should be done in order to answer whether this result is dependent on the mesh or whether it occurs due to physical phenomena.

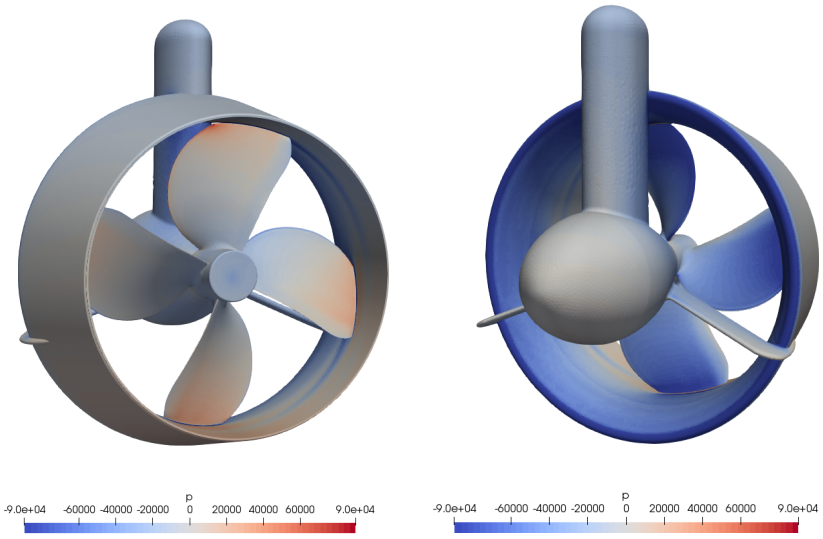

(a) Pressure side. **(b)** Suction side.

Figure 5.12: Pressure distributions at $J = 0.00$: Case 2.

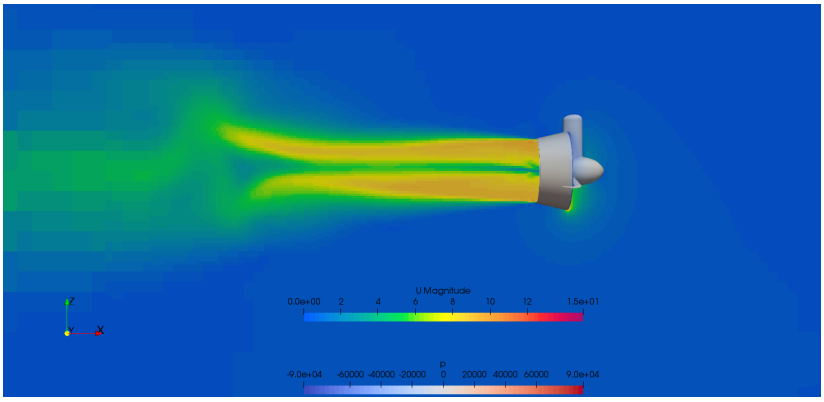

Figure 5.13: Velocity field at $J = 0.00$: Case 2.

In addition, looking at *Figure 5.14* that presents a closer view of the velocity field of Case 2, it can be observed that the inlet velocity at the nozzle leading edge is higher than the inlet velocity at the blades, hence the higher increase of the nozzle thrust compared to the blade thrust in Case 2. However, due to the increase of resistance at the same time, the net thrust generated in Case 2 is 0.68% lower than Case 1 (see *Table 5.12*).

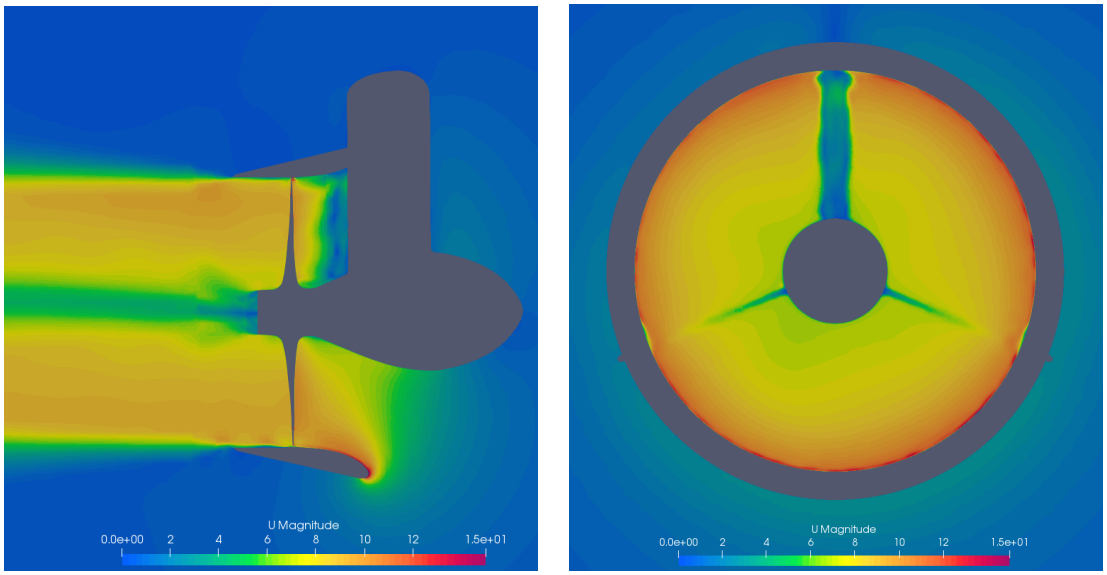

(a) Side view. **(b)** Rear view.

Figure 5.14: Velocity field at $J = 0.00$: Case 2.

5.1.3 Comparison of Case 1/Case 3

In *Table 5.5*, the hydrodynamic coefficients derived from Case 3 for the propeller-axis and in *Table 5.6* for the x-axis are presented. It should be mentioned that the coefficients of Case 3 are obtained only from the SMI results in bollard pull condition (i.e. $J = 0.00$). The thrust coefficient of the hull K_{Thull} is also included among the other coefficients that have already been discussed in the previous sections. Moreover, as in the previous section identical rotational speed $n = 191rpm$ for all the advance coefficients J has been used.

It is obvious that the results are presented in two different perspectives. By examining the first perspective (see *Table 5.5*), the values are derived from the actual thrust and presented in respect to the propeller-axis that the thrust is created. By examining the second perspective (see *Table 5.6*), the values are derived from the x-component of the actual thrust and presented in respect to the x-axis. Looking at the same tables, it could be noted that the hull values are calculated only for x-axis since the resistance of the hull is created only in this direction. Thus, the hull values are identical in both tables.

Moreover, it is noticed that the **propeller thrust** is increased significantly compared to Case 1 as well as Case 2. For a better understanding, it is highly recommended to look at the diagrams in parallel with *Table 5.12*. In a similar way, the **propeller torque** appears to be as well significantly larger compared to both previous cases. The **nozzle thrust** is also increased significantly. Furthermore, the **gear case housing resistance** is represented, which is almost identical to Case 2. Then, the **hull resistance** is introduced, which is also considered as resistance since it's negative. However, the hull resistance is really close to zero since the ship's speed is zero.

	Blades (propeller-axis)				Nozzle (propeller-axis)			
J [−]	T [kN]	K_T [-]	Q [kNm]	$10K_Q$ [-]	T [kN]	K_T [-]	Q [kNm]	$10K_Q$ [-]
0.00	199.64	0.3617	97.81	0.6563	229.82	0.4163	-38.63	-0.2592

	Gear case housing (propeller-axis)				Hull (x-axis)				Open water efficiency
J [−]	T [kN]	K_T [-]	Q [kNm]	$10K_Q$ [-]	T [kN]	K_T [-]	Q [kNm]	$10K_Q$ [-]	η_0 [-]
0.00	-35.72	-0.0714	-1.31	-0.0088	-5.08	-0.0092	62.52	0.4195	0.0000

Table 5.5: SMI results (propeller-axis): Case 3.

	Blades (x-axis)				Nozzle (x-axis)			
J [−]	T [kN]	K_T [-]	Q [kNm]	$10K_Q$ [-]	T [kN]	K_T [-]	Q [kNm]	$10K_Q$ [-]
0.00	198.55	0.3597	97.27	0.6527	228.56	0.4140	-38.42	-0.2578

	Gear case housing (x-axis)				Hull (x-axis)				Open water efficiency
J [−]	T [kN]	K_T [-]	Q [kNm]	$10K_Q$ [-]	T [kN]	K_T [-]	Q [kNm]	$10K_Q$ [-]	η_0 [-]
0.00	-35.52	-0.0710	-1.30	-0.0087	-5.08	-0.0092	62.52	0.4195	0.0000

Table 5.6: SMI results (x-axis): Case 3.

In a similar way as before, the open water efficiency looses its meaning and the total propulsive efficiency η_D becomes zero. Hence, the **merit coefficient** is used as a replacement of the total propulsive efficiency, which is further discussed in Section 5.2.

In *Figure 5.15*, the pressure distribution of Case 3 is presented. The pressure distribution seems reasonable. Furthermore, it is observed that Case 3 has an inflow similar to Case 2. The increase of the thrust in Case 3 compared to Case 1 is explained in a similar way as Case 2. Looking at *Figure 5.16* that presents the velocity field of Case 3, it is observed that a small "step" is observed at the top of the flow and under the hull. Most likely this result occurs due to a similar reason as Case 2, meaning the change of the quality of the mesh within this region. However, further investigation should also be done.

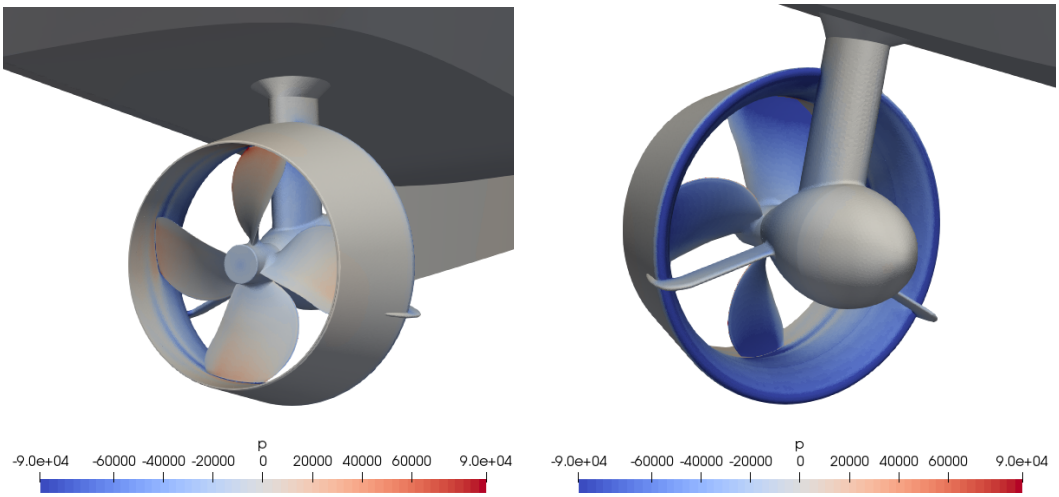

(a) Pressure side. **(b)** Suction side.

Figure 5.15: Pressure distributions at $J = 0.00$: Case 3.

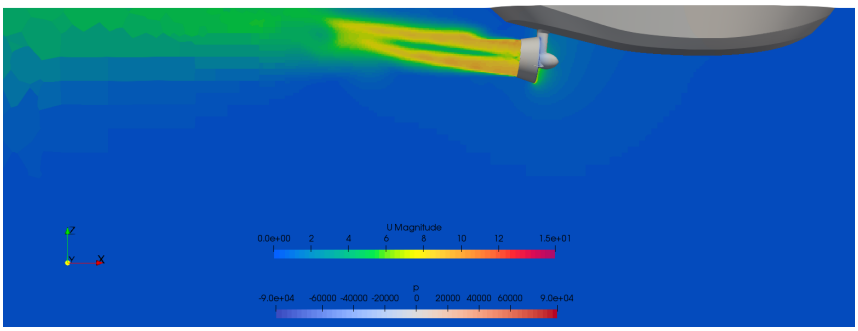

Figure 5.16: Velocity field at $J = 0.00$: Case 3.

Finally, in a similar way as Case 2, the inlet velocity at the nozzle leading edge is higher than the inlet velocity at the blades, hence the higher increase of the nozzle thrust compared to the blade thrust in Case 3. However, the net thrust generated

in Case 3 is 4.09% lower than Case 1 due to the increase of the resistance (see *Table 5.12*).

5.1.4 Comparison of Case 1/Wageningen CD Series

In the following figures, two open water characteristic diagrams derived from Case 1 and the Wageningen CD Series are presented for each of all the three different ways of comparison. For this comparison, the Microsoft Excel propCalcCD2.3.1 tool is used that has been developed by *Caterpillar Propulsion AB*.

propCalcCD2.3.1 needs some input parameters, such as brake power P_B, shaft efficiency η_S, expanded blade area ratio, propeller diameter D_P, ship velocity V_S, wake fraction w_T, rotational speed n, design pitch ratio at 0.7r and blade number. By the use of tabulated data from the Wageningen CD Series as well as from *Caterpillar Propulsion AB* test data, this tool predicts the propeller thrust, nozzle thrust, propeller torque, pitch ratio at 0.7r etc. These predicted values are used for evaluation of the early stages of a project.

Constant brake power P_B

In this section, the first comparison of Case 1 and the Wageningen CD Series is achieved.

In *Figure 5.17*, the hydrodynamic coefficients of Case 1 and the Wageningen CD Series are demonstrated. A brake power similarity is achieved between the compared cases by setting up the same brake power at the Wageningen CD Series as in Case 1. All the hydrodynamic coefficients are included while the pitch ratio at 0.7r is also plotted, which shows the geometrical similarity between the compared cases.

The brake power P_B is calculated by using the torque from the blades Q (see *Table 5.2*).

$\boldsymbol{J}$	$\boldsymbol{V_S}$ [kn]	$\boldsymbol{K_Q}$ [-]	$\boldsymbol{Q}$ [kNm]	$\boldsymbol{P_B}$ [kW]
0.00	3.3415	0.0632	94.15	**1883**
0.20	3.3415	0.0626	93.29	**1866**
0.40	6.6829	0.0587	87.44	**1749**
0.60	10.0244	0.0541	80.61	**1612**
0.80	13.3659	0.0387	57.75	**1155**

Table 5.7: Calculation of the brake power P_B by using the SMI results of Case 1.

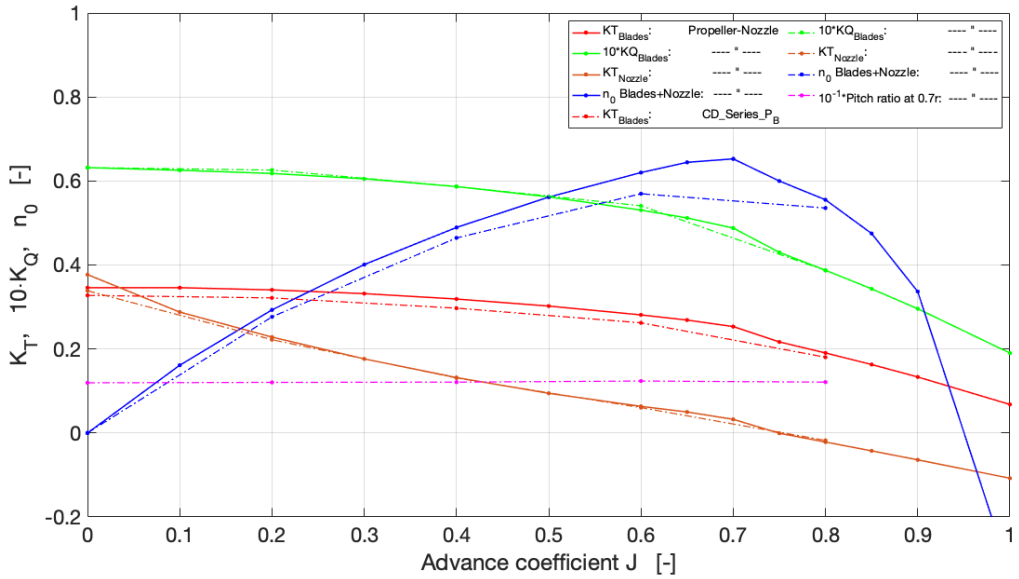

Figure 5.17: Open water characteristics diagram: Case 1/Wageningen CD Series comparison with constant P_B.

Then, the brake power P_B together with the ship's velocity V_S as well as a series of constant parameters such as:

- $n_S = 1$
- $EAR = 0.67$
- $D = 2.7m$
- $w = 0$
- $n = 191rpm$
- Design pitch ratio at 0.7r = 1.136
- No. blades = 4

are set as input parameters into the propCalcCD2.3.1 tool.

Finally, the results of propCalcCD2.3.1 are presented in the following table.

J	K_{Tp} [-]	K_{Tn} [-]	K_Q [-]	Pitch ratio at 0.7r [-]	T_p [kN]	η_0 [-]
0.00	0.3276	0.3387	0.0632	1.195	180.90	0.0000
0.20	0.3216	0.2221	0.0626	1.205	177.50	0.2765
0.40	0.2972	0.1310	0.0587	1.211	164.00	0.4644
0.60	0.2623	0.0604	0.0541	1.237	144.80	0.5696
0.80	0.1804	-0.0176	0.0387	1.211	99.60	0.5356

Table 5.8: propCalcCD2.3.1 results: Constant P_B.

Looking at *Figure 5.17*, it is noticed that the **propeller thrust** of Case 1 is higher than the one that the Wageningen CD Series suggests. For a better understanding, it is recommended to look at *Table 5.8* for the Wageningen CD Series and at *Table 5.12* for Case 1. On the other hand, the **propeller torque** appears to be identical (i.e. brake power similarity is achieved). The **nozzle thrust** behaves in a similar

way for most of the advance coefficients while there is a quite big difference between $J = 0.00 - 0.10$ with Case 1 having a higher thrust at bollard pull condition. Finally, the **pitch ratio at 0.7r** remains almost identical within the whole diagram for the Wageningen CD Series, which has values really close to the constant pitch ratio of Case 1, which is 1.136.

Constant thrust power P_T

In this section, the second comparison of Case 1 and the Wageningen CD Series is achieved.

In *Figure 5.18*, the hydrodynamic coefficients of Case 1 and the Wageningen CD Series are demonstrated. A thrust power similarity is achieved between the compared cases by setting up the same thrust power at the Wageningen CD Series as in Case 1. The hydrodynamic coefficients and the pitch ratio at 0.7r are included as previously.

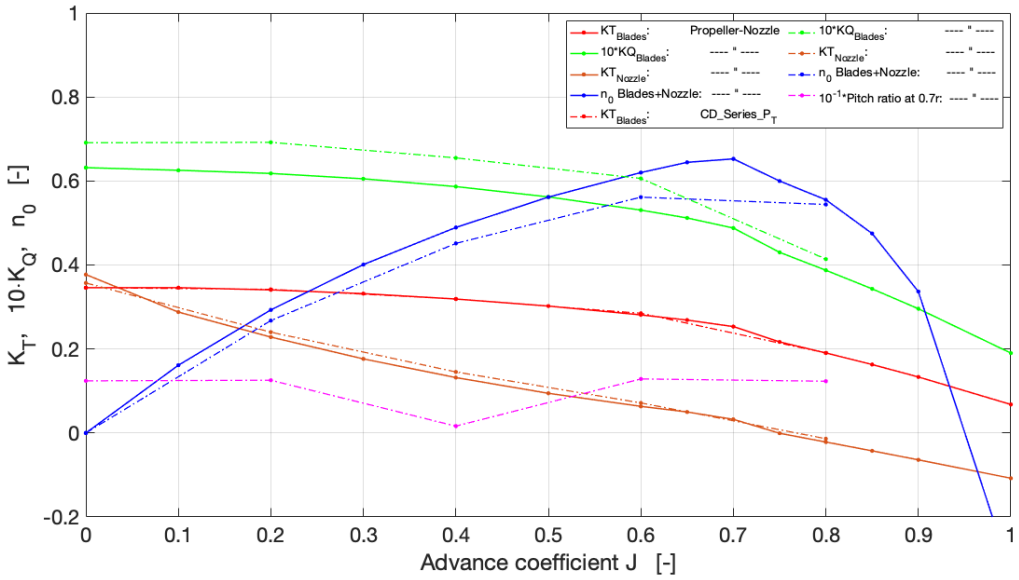

Figure 5.18: Open water characteristics diagram: Case1/Wageningen CD Series comparison with constant P_T.

The thrust power P_T is calculated by using the thrust from the propeller blades T_p (see *Table 5.2*).

J	V_S [kn]	T_p [kN]	K_{Tp} [-]	P_T [kW]
0.00	3.3415	190.98	0.3460	**0**
0.20	3.3415	188.78	0.3420	**325**
0.40	6.6829	176.08	0.3190	**605**
0.60	10.0244	157.22	0.2848	**811**
0.80	13.3659	105.18	0.1905	**723**

Table 5.9: Calculation of the thrust power P_T by using the SMI results of Case 1.

Then, the thrust power P_T together with the ship's velocity V_S as well as the same constant parameters as previously are set as input parameters into propCalcCD2.3.1.

Finally, the results of propCalcCD2.3.1 are presented in the following table.

J	K_{Tp} [-]	K_{Tn} [-]	K_Q [-]	**Pitch ratio at 0.7r** [-]	P_B [kW]	η_0 [-]
0.00	0.3460	0.3572	0.0691	1.241	2061	0.0000
0.20	0.3420	0.2400	0.0692	1.256	2064	0.2677
0.40	0.3190	0.1454	0.0655	0.163	1953	0.4514
0.60	0.2850	0.0716	0.0606	1.287	1807	0.5615
0.80	0.1905	-0.0136	0.0414	1.232	1234	0.5440

Table 5.10: propCalcCD2.3.1 results: Constant P_T.

Looking at *Figure 5.18*, it is noticed that the **propeller thrust** appears to be identical (i.e. thrust power similarity is achieved). On the other hand, the **propeller torque** appears to be quite higher for the Wageningen CD Series compared to Case 1. For a better understanding, it is recommended to look at *Table 5.10* for the Wageningen CD Series and at *Table 5.12* for Case 1. The **nozzle thrust** appears to be quite similar in both compared cases. However, Case 1 achieves a higher nozzle thrust at bollard pull condition while in the rest of the diagram the Wageningen CD Series is leading with higher thrust. Finally, the **pitch ratio at 0.7r** remains almost identical between $J = 0.00 - 0.20$ and $J = 0.60 - 0.80$ while a difference appears for $J = 0.20 - 0.60$.

Constant pitch ratio at 0.7r

In this section, the third and last comparison of Case 1 and the Wageningen CD Series is achieved.

In *Figure 5.19*, the hydrodynamic coefficients of Case 1 and the Wageningen CD Series are demonstrated. A geometrical similarity is achieved between the compared cases by setting a constant pitch ratio at 0.7r.

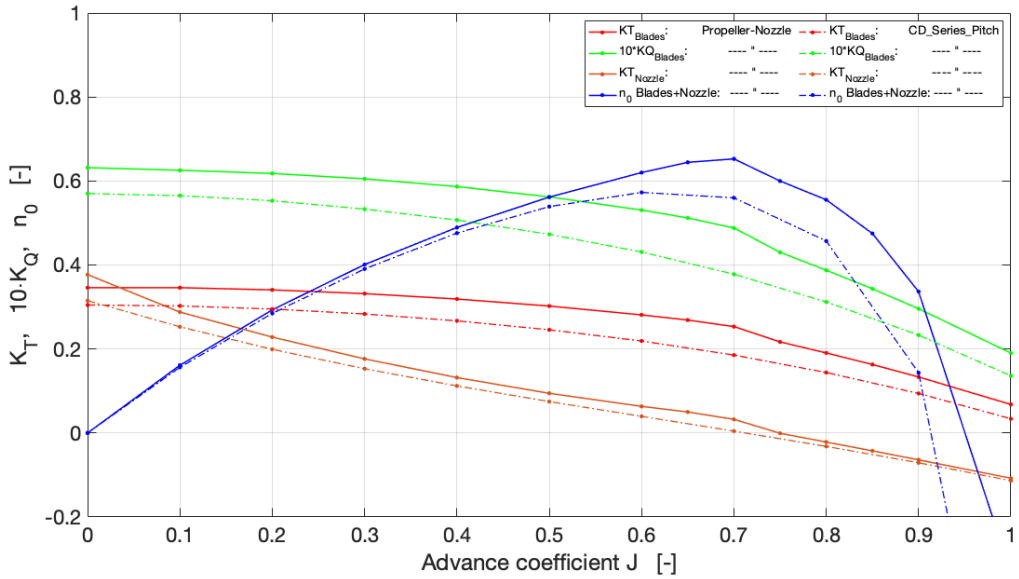

Figure 5.19: Open water characteristics: Case1/CD Series with constant pitch ratio at 0.7r comparison.

In this case, a geometrical comparison is achieved. Thus, the pitch ratio at 0.7r is the only input parameter into propCalcCD2.3.1, which is same as before:

- Design pitch ratio at 0.7r = 1.136

Finally, the results of propCalcCD2.3.1 are presented in the following table.

J	K_{Tp} [-]	K_{Tn} [-]	K_Q [-]	P_B [kW]	T_p [kN]	η_0 [-]
0.00	0.3048	0.3152	0.0570	1698	168.24	0.0000
0.10	0.3025	0.2528	0.0565	1685	166.99	0.1563
0.20	0.2951	0.1992	0.0553	1647	162.91	0.2847
0.30	0.2834	0.1530	0.0533	1590	156.45	0.3906
0.40	0.2670	0.1121	0.0507	1512	147.40	0.4759
0.50	0.2457	0.0748	0.0473	1411	135.63	0.5390
0.60	0.2190	0.0396	0.0431	1285	120.88	0.5728
0.70	0.1855	0.0045	0.0378	1127	102.40	0.5599
0.80	0.1440	-0.0320	0.0312	930	79.51	0.4571
0.90	0.0941	-0.0709	0.0233	693	51.97	0.1433
1.00	0.0338	-0.1135	0.0136	406	18.68	-0.9300

Table 5.11: propCalcCD2.3.1 results: Constant pitch ratio at 0.7r.

Looking at *Figure 5.19*, it is obviously recognised that the **propeller thrust** is much lower for the Wageningen CD Series within the whole range of the diagram. Similarly, the **propeller torque** is much lower for the Wageningen CD Series compared to Case 1. For a better understanding, it is recommended to look at *Table 5.11* for the Wageningen CD Series and *Table 5.12* for Case 1. The **nozzle thrust** appears to be again lower for the Wageningen CD Series with a significant difference

between $J = 0.00 - 0.20$.

Finally, it should be mentioned that there are other differences between the geometrical properties of the propeller as well as differences between the geometrical properties of the nozzle between Case 1 and the Wageningen CD Series, thus **the plotted Wageningen CD Series values might differ in reality**. Thus, the above comparisons can only provide an approximation of the behaviour.

5.1.5 Flow separation

Looking at *Figure 5.2*, a small change in the slope of the hydrodynamic coefficients between $J = 0.70$ and $J = 0.80$ is observed. By visualizing the pressure distribution and the velocity fields of both cases in ParaView 5.6.0, derived from the MRF simulations, it is observed that **flow separation** occurs within this region. More specifically, looking at *Figure 5.21* it is observed that separation arises on the nozzle, starting at the advance coefficient $J = 0.75$ while prior to this point no separation appears. After this point, separation increases proportionally with the advance coefficient.

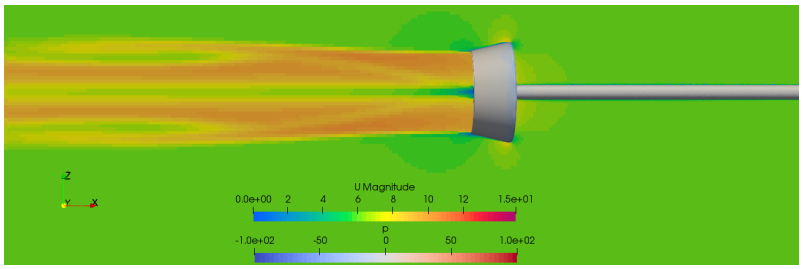

Figure 5.20: Velocity field in free sailing condition: Case 1 MRF simulation at $J = 0.70$.

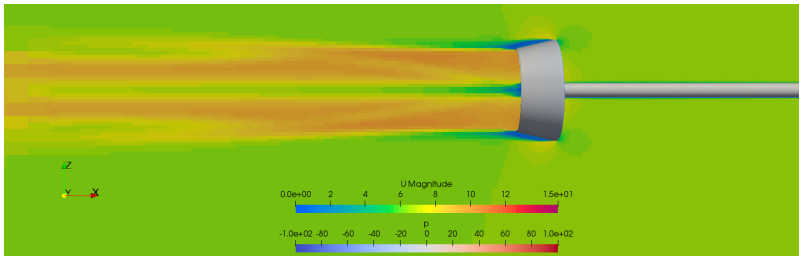

Figure 5.21: Velocity field in free sailing condition: Case 1 MRF simulation at $J = 0.75$.

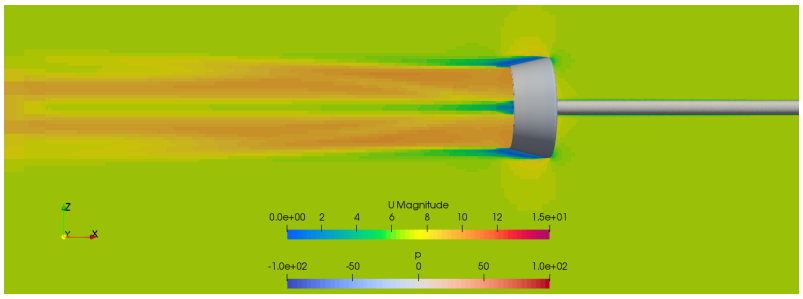

Figure 5.22: Velocity field in free sailing condition: Case 1 MRF simulation at $J = 0.80$.

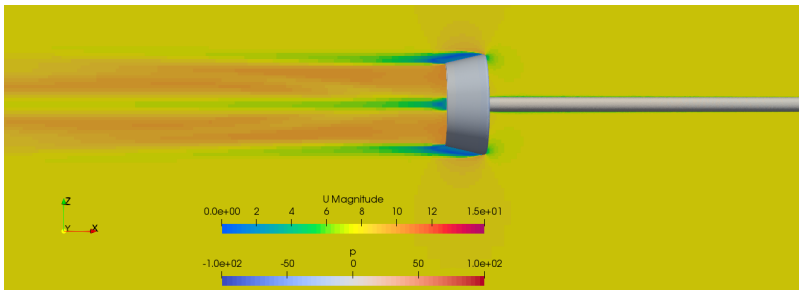

Figure 5.23: Velocity field in free sailing condition: Case 1 MRF simulation at $J = 0.90$.

Finally, comparing the MRF (see *Figure 5.22*) and SMI (see *Figure 5.24*) results for the advance coefficient $J = 0.80$ where the flow separation has already occured, it is obvious that the separation is of similar scale. On the other hand, the flow field of MRF is slightly different from the one of the SMI, with the SMI flow field resulting in a more straight flow compared to the one of MRF.

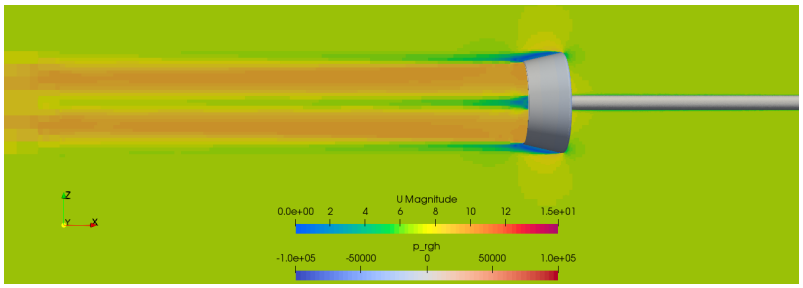

Figure 5.24: Velocity field in free sailing condition: Case 1 SMI simulation at $J = 0.80$.

5.1.6 Cavitation

Looking at the three following figures, it is observed that a really low pressure in Case 2 and Case 3 occurs at the connection point of the gear case housing and the nozzle as well as at the tip of the blade that is behind the gear case housing. This observation indicates that cavitation will first appear at these points.

In this low pressure region the pressure value derived from the CFD simulations, which is read from ParaView, is equal to:

$$-200kPa$$

The atmospheric pressure of the air is equal to:

$$1atm = 101.325kPa$$

and the hydrostatic pressure is equal to:

$$\rho \cdot g \cdot z = 1025kg/m^3 \cdot 9.81m/s^2 \cdot 2.4m = 24.133kPa$$

where:
z is the distance of the upper part of the nozzle and the water surface.

By summing up the three pressure values above, the actual pressure at the connection point of the gear case housing and the nozzle is calculated, which is equal to $-74.54kPa$. This is an unrealistic pressure since the vapor pressure for sea water at $20°C$ is equal to $2.29kPa$. In other words, this means that the minimum value that the pressure can get is $2.29kPa$, while when this minimum value is exceeded, cavitation will occur. Thus, this should be further investigated by running cavitation CFD simulations.

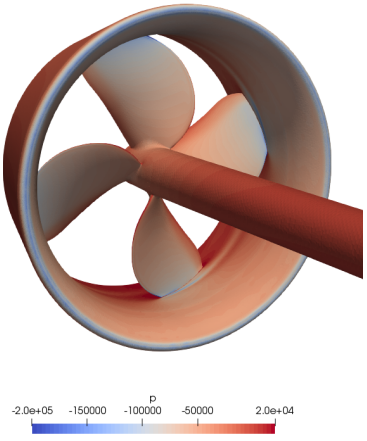

Figure 5.25: Pressure distributions in bollard pull condition: Case 1.

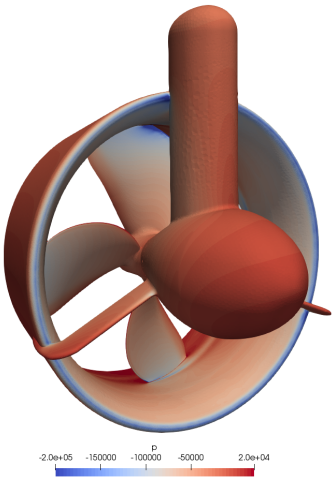

Figure 5.26: Pressure distributions in bollard pull condition: Case 2.

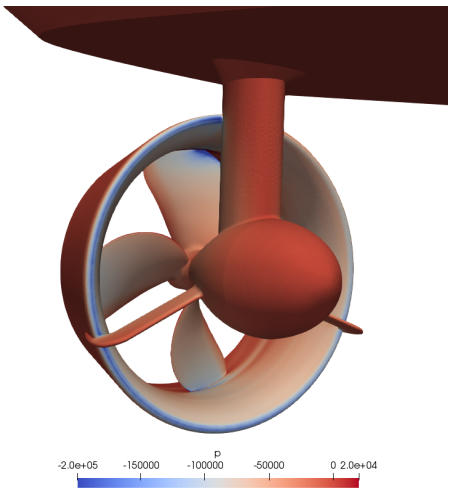

Figure 5.27: Pressure distributions in bollard pull condition: Case 3.

5.2 Hydrodynamic interactions in bollard pull condition

In this section, the hydrodynamic interactions of all the cases in bollard pull condition (i.e. $J = 0.00$) are demonstrated and a comparison among these cases is achieved. Moreover, a short explanation of some of the variables is given since there are variables with special subscripts that haven't been discussed prior to this moment.

In *Table 5.12*, the hydrodynamic coefficients of all the cases are decomposed and a detailed presentation of the thrust of each component is presented. Furthermore, the torque coefficients derived from the propeller blades are also presented. It can also be observed that Case 3 is divided into two parts. This is done in order to express the forces in respect to the x-axis as well as the axis that the propeller is

rotating.

Coefficients	Case 1	Case 2	Case 3 x-axis	Case 3 propeller-axis
	[-]	[-]	[-]	[-]
K_T blades	0.3460	0.3496	0.3597	0.3617
$10K_Q$ blades	0.6317	0.6373	0.6527	0.6563
K_T nozzle	0.3772	0.4388	0.4140	0.4163
K_T gear_case_housing	-	-0.0703	-0.0710	-0.0714
K_T hull	-	-	-0.0092	-0.0092
$K_{T,net}$	0.7231	0.7182	0.6935	0.6935

Table 5.12: Decomposition of the hydrodynamic coefficients in bollard pull condition.

The above table is then presented in percentages, which makes it easier to identify the contribution of each component to the thrust and resistance accordingly.

Coefficients	Case 1	Case 2	Case 3 x-axis	Case 3 propeller-axis
	[%]	[%]	[%]	[%]
K_T blades	47.85	48.68	51.87	52.16
$10K_Q$ blades	-	-	-	-
K_T nozzle	52.16	61.10	59.70	60.03
K_T gear_case_housing	-	-9.79	-10.24	-10.30
K_T hull	-	-	-1.33	-1.33
$K_{T,net}$	100.00	100.00	100.00	100.00

Table 5.13: Decomposition of the hydrodynamic coefficients in bollard pull condition.

Looking at *Table 5.13*, it is observed that **the nozzle has the highest contribution in thrust** for all cases. Besides that, the gear case housing has the highest contribution to resistance for all cases.

In the following tables (see *Table 5.14*, *Table 5.15*, *Table 5.16* & *Table 5.17*), a comparison among the cases is presented by demonstrating values derived from the CFD simulation in OpenFOAM as well as by demonstrating the calculated hydrodynamic interactions.

In *Table 5.14*, T_{net} represents the net sum of the total thrust (i.e. $T - R$), $T_{net,deduct}$ represents its deduction and T_{BP} represents the bollard pull force. In *Table 5.15*, $K_{T,T}$ represents the sum of the thrust coefficients that are creating thrust (i.e. $K_{Tp} + K_{Tn}$), $K_{T,R}$ represents the sum of the thrust coefficients that are derived from the parts that are creating resistance (i.e. Case 2: $K_{Tgear\_case\_housing}$ and Case

3: $K_{Tgear\_case\_housing} + K_{Thull}$), $K_{T,net}$ represents the net sum of all the thrust coefficients (i.e. $K_{T,T} - K_{T,R}$), m_c represents the merit coefficient and finally $m_{c,deduct}$ represents its deduction.

In *Table 5.16*, n_{1995kw} represents the rotational velocity of the propeller at a fixed delivered power and $n_{1995kw,deduct}$ represents its deduction. Here it should be mentioned that a delivered power of $P_D = 1995kW$ is derived from the main engine's power (see *Table 3.1*) with a reduction factor of 5%. Looking again at the definition of the variables, T_{1995kw} represents the generated thrust at a fixed delivered power and $T_{1995kw,deduct}$ represents its deduction. $P_{D,191rpm}$ represents the delivered power at a fixed rotational speed and $P_{D,191rpm,deduct}$ represents its deduction. Finally, T_{191rpm} represents the generated thrust at a fixed rotational speed and $T_{191rpm,deduct}$ its deduction. It should be mentioned that the 191 rpm is an estimation of another CFD study that was conducted within *Caterpillar Propulsion AB*.

Note: All the calculations below are presented for half the vessel and one azimuth thruster unit. Moreover, the values presented in *Table 5.14* and *Table 5.15* are derived from the CFD results while in *Table 5.16* and *Table 5.17* the values are calculated by assuming constant delivered power and rotational velocity accordingly.

Case	Parts included	T [kN]	R [kN]	t [%]	T_{net} [kN]	$T_{net,deduct}$ [%]	T_{BP} [ton]
Case 1	Blades+Nozzle	399.17	0.00	0.00	399.17	0.00	40.69
Case 2	Blades+Nozzle+Gear Case Housing	435.24	38.81	8.92	396.44	0.69	40.41
Case 3 excluding hull	Blades+Nozzle+Gear Case Housing	427.11	35.52	8.32	391.58	1.90	39.92
Case 3 including hull	Blades+Nozzle+Gear Case Housing Hull	427.11	40.33	9.44	386.50	3.17	39.40

Table 5.14: Case comparison: Presentation of the thrust, resistance, thrust deduction, net forces, deduction of the net forces and bollard pull forces.

Case	$K_{T,T}$ [-]	$K_{T,R}$ [-]	$10K_Q$ [-]	$K_{T,net}$ [-]	m_c [-]	$m_{c,deduct}$ [%]
Case 1	0.7231	0.0000	0.6317	0.7231	1.7481	0.00
Case 2	0.7885	0.0703	0.6373	0.7182	1.7150	1.90
Case 3 excluding hull	0.7737	0.0710	0.6527	0.7027	1.6210	7.27
Case 3 including hull	0.7737	0.0797	0.6527	0.6935	1.5892	9.09

Table 5.15: Case comparison: Presentation of thrust, torque, net thrust coefficients, merit coefficient and the deduction of the merit coefficient.

Case	n_{1995kw} [rpm]	$n_{1995kw,deduct}$ [%]	T_{1995kw} [kN]	$T_{1995kw,deduct}$ [%]
Case 1	194.71	0.00	414.82	0.00
Case 2	194.14	0.31	409.56	1.27
Case 3 excluding hull	192.60	1.08	394.45	4.91
Case 3 including hull	192.60	1.08	389.28	6.16

Table 5.16: Case comparison: Presentation of the rotational velocity, thrust and their deduction in constant delivered power.

Case	$P_{D,191rpm}$ [kW]	$P_{D,191rpm,deduct}$ [%]	T_{191rpm} [kN]	$T_{191rpm,deduct}$ [%]
Case 1	1883	0.00	399.17	0.00
Case 2	1900	-0.89	396.44	0.69
Case 3 excluding hull	1946	-3.31	387.91	2.82
Case 3 including hull	1946	-3.31	382.83	4.09

Table 5.17: Case comparison: Presentation of the delivered power, thrust and their deduction in constant rotational velocity.

Looking at *Table 5.14*, it can be seen that 8.92% of the **thrust deduction** occurs at Case 2 when the gear case housing is placed behind the propeller and the nozzle. By placing the whole azimuth thruster unit behind the hull and by excluding the resistance created by the hull the thrust is deducted by 8.32%. Finally, the thrust is deducted by 9.44% by including the resistance of the hull. Thus, **the highest thrust deduction occurs at Case 2 by placing the gear case housing behind the propeller and the nozzle** while the hull has a smaller contribution to the thrust deduction.

The **merit coefficient** is introduced as a replacement of the total propulsive efficiency η_D. Looking at *Table 5.15*, it can be seen that the merit coefficient of Case 2 is deducted by 1.90% when the gear case housing is placed behind the propeller and the nozzle. Meanwhile, the merit coefficient of Case 3 is deducted by 7.27% by excluding the hull and by 9.09% by including the hull. Hence, **the highest merit deduction occurs at Case 3 by placing the whole azimuth thruster unit behind the hull** due to the flow field that is generated by the hull while the resistance from the hull itself has a smaller contribution of only 1.82%.

By reviewing *Table 5.16*, it can be identified that **the highest decrease of rotational speed of the propeller** as well as **the highest thrust decrease occurs in Case 3**. However, the decrease of both values is almost unnoticeable.

In the end, by reviewing *Table 5.17*, similar conclusions as in *Table 5.16* can be drawn.

In *Table 5.18*, $T_{BP,1995kw,CFD}$ is representing the bollard pull force that is derived from the generated thrust at a fixed delivered power T_{1995kw} (see *Table 5.16*). This generated thrust is calculated based on the CFD simulation results. Moreover, $T_{BP,1995kw,CD}$ is the bollard pull force that the Wageningen CD Series gives, which is calculated in propCalcCD2.3.1 by using as inputs the delivered power $P_D = 1995kW$ and the rotational velocity at a fixed delivered power n_{1995kw} among other parameters.

Case	$\boldsymbol{T_{BP,1995kw,CFD}}$ [ton]	$\boldsymbol{T_{BP,1995kw,CD}}$ [ton]	$\boldsymbol{T_{BP,1995kw,CD}/T_{BP,1995kw,CFD}}$ [%]
Case 1	42.29	38.81	8.23
Case 2	41.75	-	-
Case 3 excluding hull	40.21	-	-
Case 3 including hull	39.68	36.10	9.02

Table 5.18: Case comparison: Presentation of the hydrodynamic coefficients in bollard pull condition and comparison with the Wageningen CD Series.

A reduction factor of 7% is added at $T_{BP,1995kw,CD}$ for the hull (i.e. Case 3 including hull) while the reductions that appear on Case 2 and Case 3 by excluding the hull are unknown.

5.3 Accuracy and reliability

The highest accuracy of the results is immensely connected with the size and quality of the mesh, the choice of the numerical methods of turbulence modelling and the choice of the turbulence model. A really high quality mesh has been achieved during this project since almost half of this project in respect to time was dedicated to the mesh generation. A lot of manual work was required to generate the mesh, which means that every part of the mesh has thoughtfully been created by the user. The reliability of the results can be obtained by comparing different mesh sizes, numerical methods and turbulence models as well as by comparing the convergence of the results. However, this is very time consuming, thus, the above choices were made according to standard procedures that have been validated and used for a long time by *Caterpillar Propulsion AB*.

6

Conclusions and future work

In this chapter, a conclusion of this study project is drawn and the degree that the initial purposes are fulfilled within this project is presented. In the end of the chapter, suggestions for further investigations and things that should be kept in mind are presented as part of the future work.

The CFD modelling of a propeller indicates a relative motion between the stationary parts and the rotor of a propulsion unit and the vehicle that this propulsion unit is mounted on. Two methodologies have been used within this project in order to capture this motion: the steady state Multiple Reference Frame (MRF) and the transient Sliding Mesh Interface (SMI). By comparing the simulation results of SMI and MRF and by looking at their convergence plots, it is concluded that the transient SMI methodology gives much more accurate results compared to the steady state MRF for low advance coefficient J values. Meanwhile, the results for medium J values computed with the MRF approach are quite reasonable. Finally, MRF gives appropriate results at low computational cost for initializing the flow properties of the CFD simulations in a steady state so then these flow properties can be used to proceed to transient SMI simulations in order to increase the accuracy of the results.

Looking into the results of interest of this study project, it is concluded that the contribution of the nozzle is higher than the propeller in terms of thrust while the contribution of the gear case housing is higher than the hull in terms of resistance. Thus, the highest thrust deduction occurs on the gear case housing. Bollard pull condition indicates advance coefficient J and velocity of the ship V_S both equal to zero. As a result, the open water efficiency looses its meaning and the propulsive efficiency η_D becomes zero. Thus, the performance of the propulsion unit in bollard pull condition needs to be expressed with the merit coefficient m_c, which is a replacement of the total propulsive efficiency η_D. Moving back to the results of interest, the highest merit deduction occurs when placing the gear case housing behind the hull. Finally, a higher bollard pull force of the open water case (i.e. Case 1) compared to the Wageningen CD Series is observed.

During the current study, a symmetry boundary condition has been used at the top and side of the domain during the CFD simulations. As part of the future work would be to include the free surface effect at the top boundary instead. It would also be suggested to run more transient SMI simulations, whether enough resources are available to proceed to these computationally expensive simulations, in order to complete the open water characteristic diagrams only with transient SMI results.

CFD simulations in order to get the towing resistance of the hull for various J values and investigation of the behavior of the gear case housing and hull in free running condition would also be suggested. Furthermore, cavitation should be investigated more by running cavitation CFD simulations. Moreover, comparison of numerical methods and turbulence models should be included in order to obtain the reliability of the results. Last but not least, a grid refinement study should be done.

References

Bergman, T. L., Lavine, A. S., Incropera, F. P., & Dewitt, D. P. (2011). *Fundamentals of Heat and Mass Transfer* (7th ed.). Chichester, United Kingdom: John Wiley and Sons Ltd.

Carlton, J. S. (2007). *Marine Propellers and Propulsion* (2nd ed.). Burlington, USA: Elsevier Ltd.

Dyne, G., & Bark, G. (2005). *Ship Propulsion: Compendium for part of the MSc course "Ship resistance and propulsion"*. Gothenburg, Sweden.

Fletcher, C. A. J. (1991). *Computational Techniques for Fluid Dynamics: Specific Techniques for Different Flow Categories* (2nd ed.). Berlin; New York: Springer-Verlag.

Funeno, I. (2009). Hydrodynamic Optimal Design of Ducted Azimuth Thrusters. In *Proceedings of the First International Symposium on Marine Propulsors - smp'09*, Trondheim, Norway.

Gullberg, P., & Sengupta, R. (2011). *Axial Fan Performance Predictions in CFD, Comparison of MRF and Sliding Mesh with Experiments.* doi:https://doi-org.proxy.lib.chalmers.se/10.4271/2011-01-0652

Larsson, L., & Raven, H. C. (2010). *The Principles of Naval Architecture Series: Ship Resistance and Flow.* Jersey City, USA: The Society of Naval Architects and Marine Engineers.

Liu, F. (2017). A Thorough Description Of How Wall Functions Are Implemented In OpenFOAM. In *Proceedings of the CFD with OpenSource Software, 2016, Edited by Nilsson. H.* Gothenburg, Sweden. Retrieved from http://www.tfd.chalmers.se/~hani/kurser/OS_CFD_2016

Liu, J., Lin, H., & Purimitla, S. R. (2016). Wake field studies of tidal current turbines with different numerical methods.

Matin, F. (2011). *Hydrodynamics of Conventional Propeller and Azimuth Thruster in Behind Condition.* (Master's thesis, Chalmers University of Technology, Department of Shipping and Marine Technology).

Menter, F. R., Kuntz, M., & Langtry, R. (2003). Ten Years of Industrial Experience with the SST Turbulence Model. In *Proceedings of the Fourth International Symposium on Turbulence, Heat and Mass Transfer*, Redding, USA.

OpenCFD Ltd. (2018). OpenFOAM User Guide v1812. Retrieved from https://www.openfoam.com/documentation/user-guide/

Tabib, M., Siddiqui, M. S., Rasheed, A., & Kvamsdal, T. (2017). Industrial scale turbine and associated wake development - comparison of RANS based Actuator Line Vs Sliding Mesh Interface Vs Multiple Reference Frame method.

In *Proceedings of the 14th Deep Sea Offshore Wind R&D Conferencem EERA DeepWind'2017*, Trondheim, Norway.

Versteeg, H. K., & Malalasekera, W. (2007). *An Introduction to Computational Fluid Dynamics: The Finite Volume Method* (2nd ed.). Harlow, England: Pearson Education Limited.

Appendices

A

Convergence of the simulated results

In this chapter, the total forces and moments extracted from the OpenFOAM simulations are plotted and their convergence is observed.

The total forces and moments extracted from the OpenFOAM v1806 simulations for all the cases used within this study project are plotted with MATLAB R2018b and their convergence is observed. For a better understanding, all the simulated cases are presented below:

- MRF Simulations at $J = 0.00, 0.10, 0.20, 0.30, 0.40, 0.50, 0.60, 0.65, 0.70, 0.75, 0.80, 0.85, 0.90, 1.00$,
- SMI Simulations at $J = 0.00, 0.20, 0.40, 0.60, 0.80$,
- SMI Simulations at $J = 0.00, 0.20, 0.40, 0.60, 0.70, 0.80, 0.90, 1.00$,
- SMI Simulations at $J = 0.00$.

All the convergence plots bellow are represented in all the three dimensions (i.e. x-dir, y-dir and z-dir).

A.1 Convergence plots of Case 1

x-dir

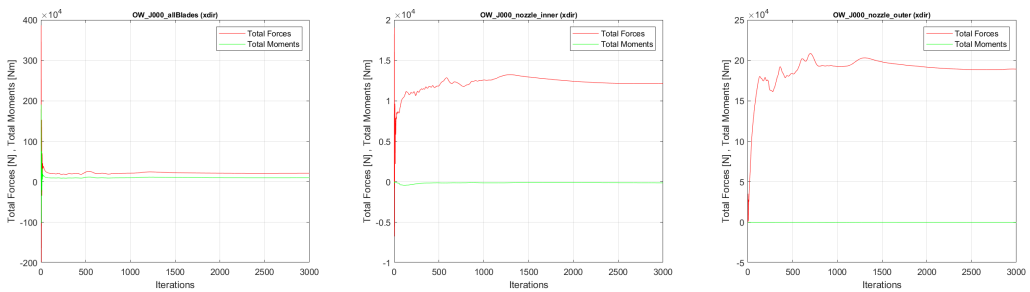

(a) MRF.

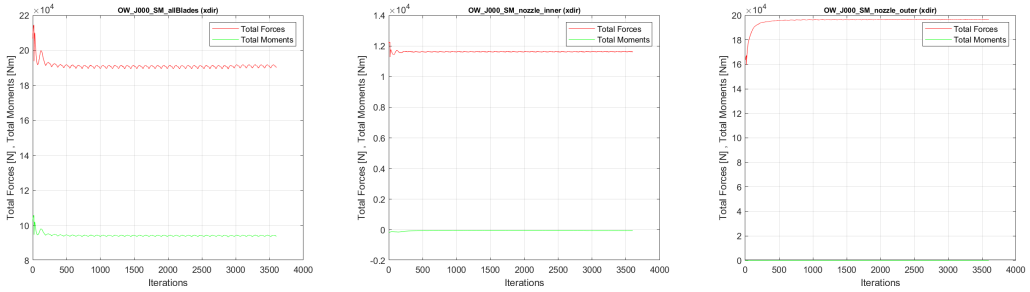

(b) SMI.

Figure A.1: Simulations at $J = 0.00$.

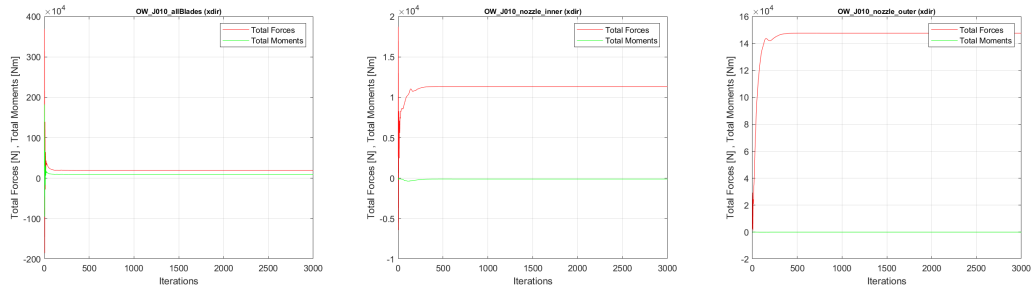

Figure A.2: MRF simulation of Case 1 at $J = 0.10$.

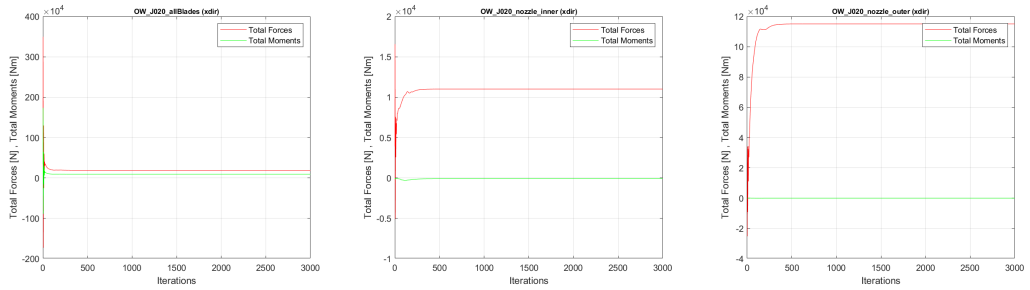

(a) MRF.

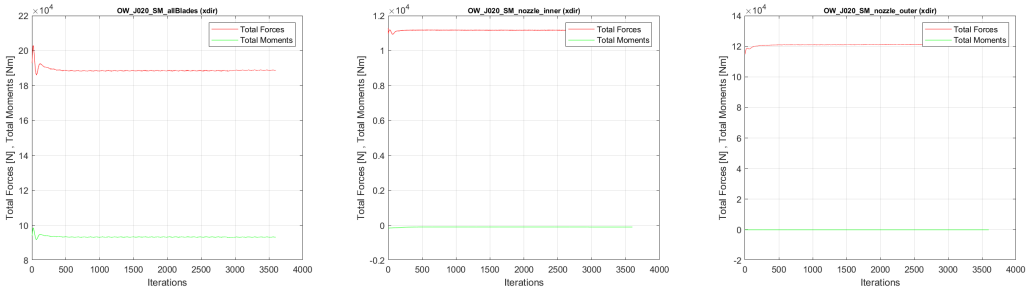

(b) SMI.

Figure A.3: Simulations at $J = 0.20$.

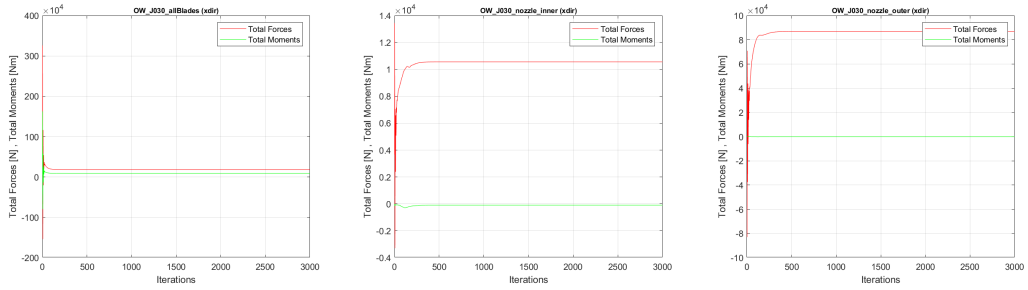

Figure A.4: MRF simulation of Case 1 at $J = 0.30$.

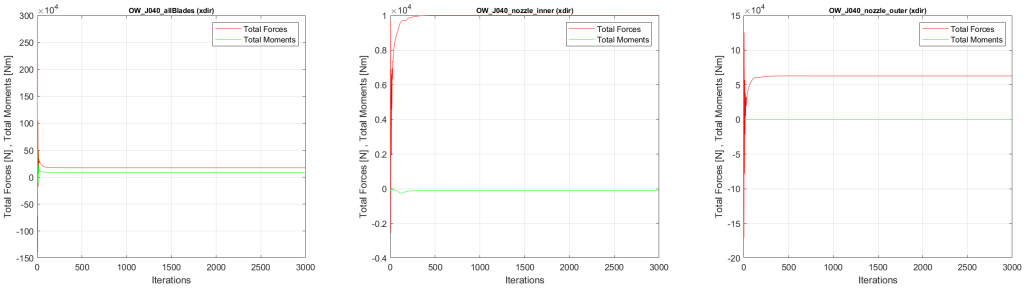

(a) MRF.

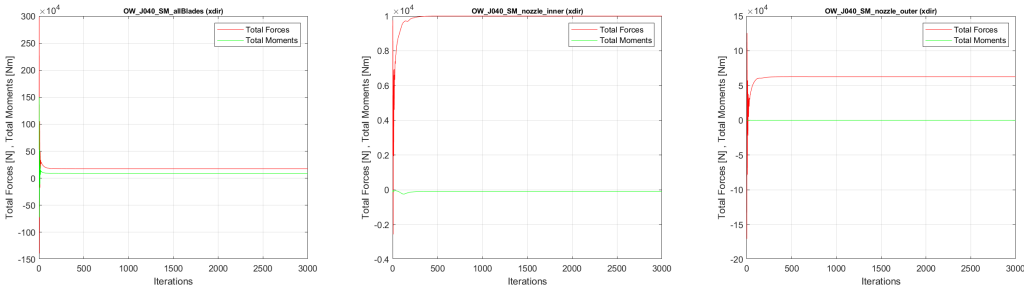

(b) SMI.

Figure A.5: Simulations at $J = 0.40$.

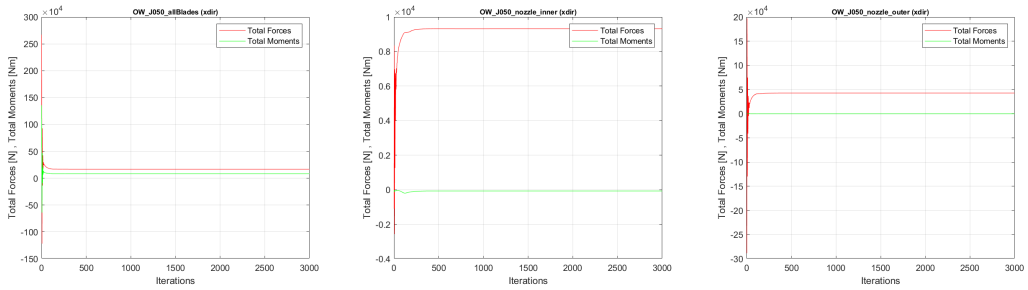

Figure A.6: MRF simulation of Case 1 at $J = 0.50$.

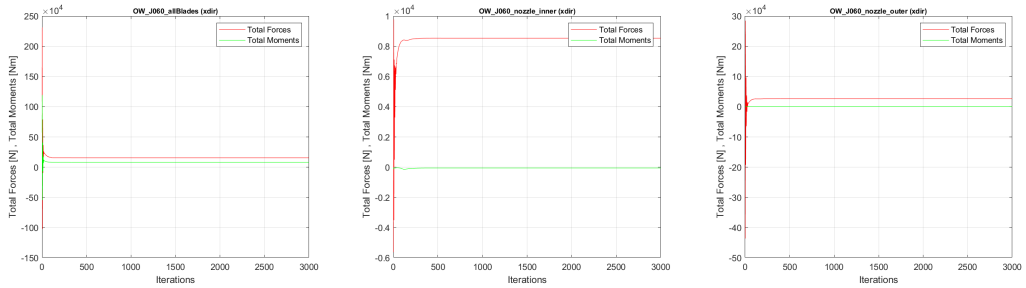

(a) MRF.

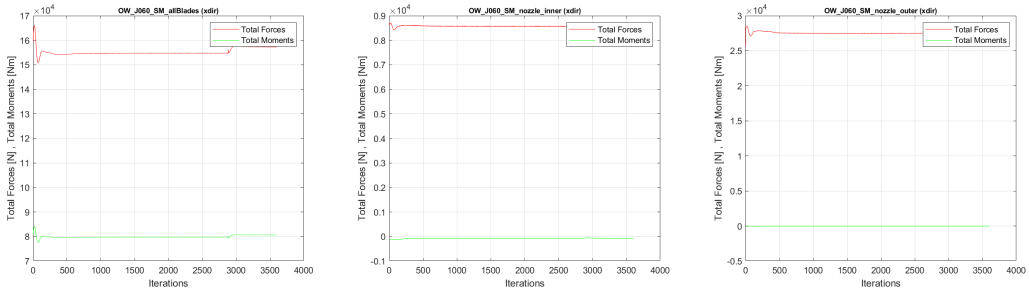

(b) SMI.

Figure A.7: Simulations at $J = 0.60$.

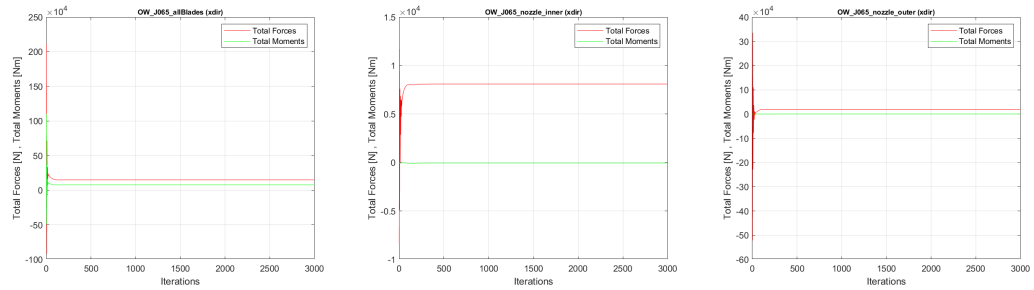

Figure A.8: MRF simulation of Case 1 at $J = 0.65$.

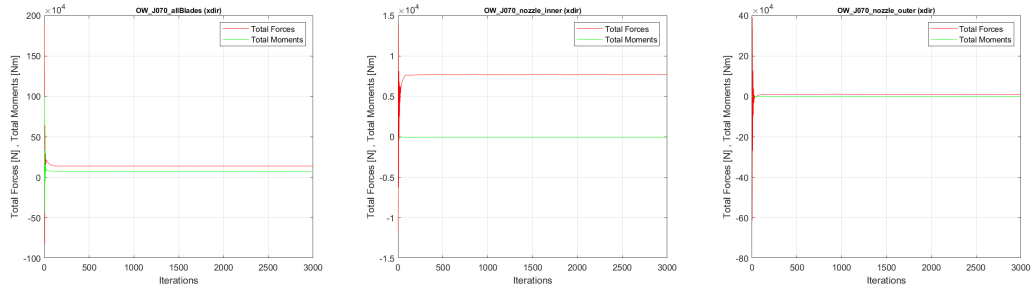

Figure A.9: MRF simulation of Case 1 at $J = 0.70$.

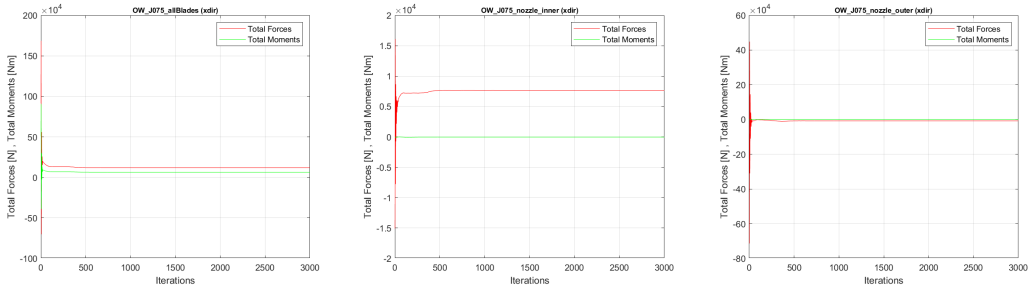

Figure A.10: MRF simulation of Case 1 at $J = 0.75$.

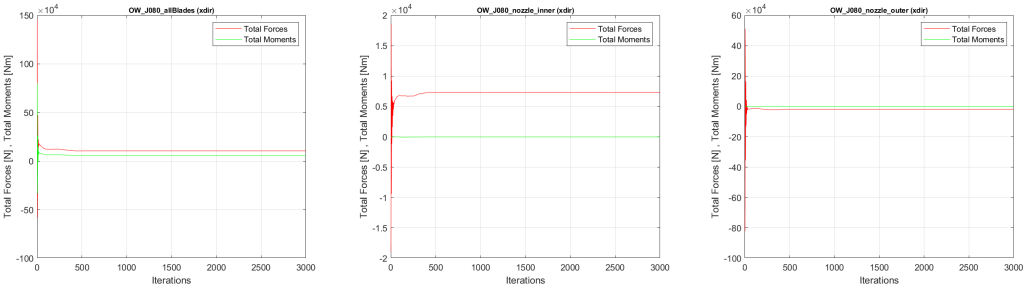

(a) MRF.

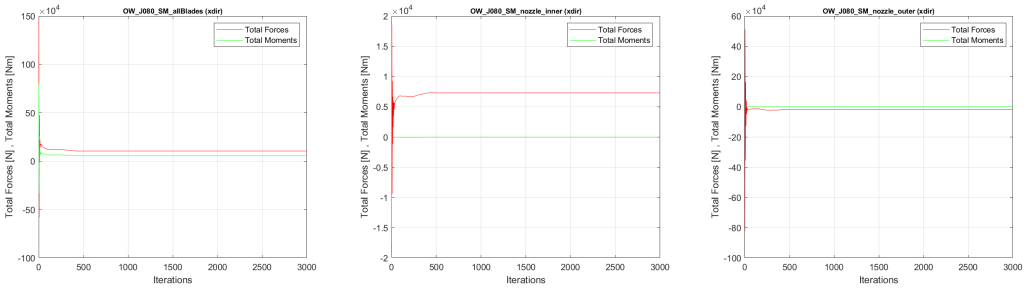

(b) SMI.

Figure A.11: Simulations at $J = 0.80$.

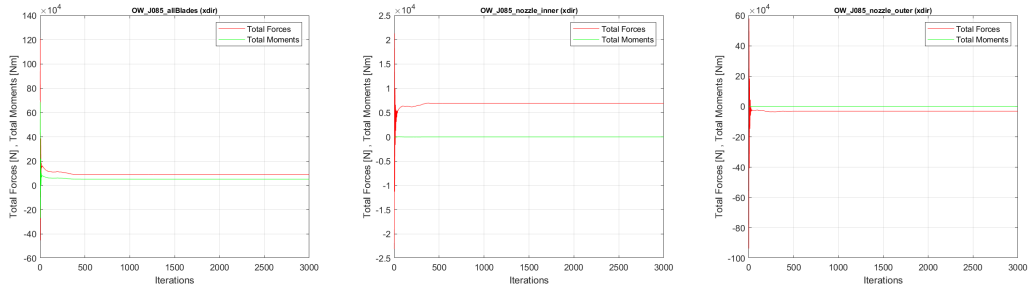

Figure A.12: MRF simulation of Case 1 at $J = 0.85$.

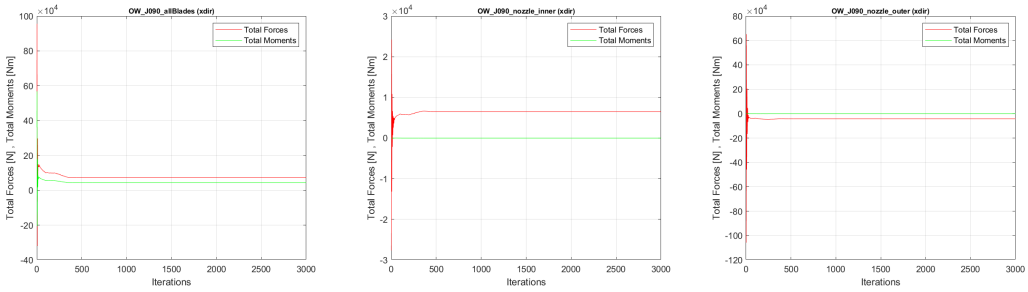

Figure A.13: MRF simulation of Case 1 at $J = 0.90$.

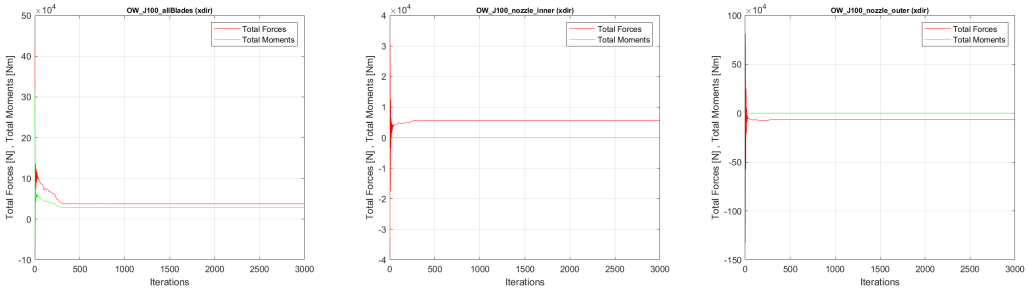

Figure A.14: MRF simulation of Case 1 at $J = 1.00$.

y-dir

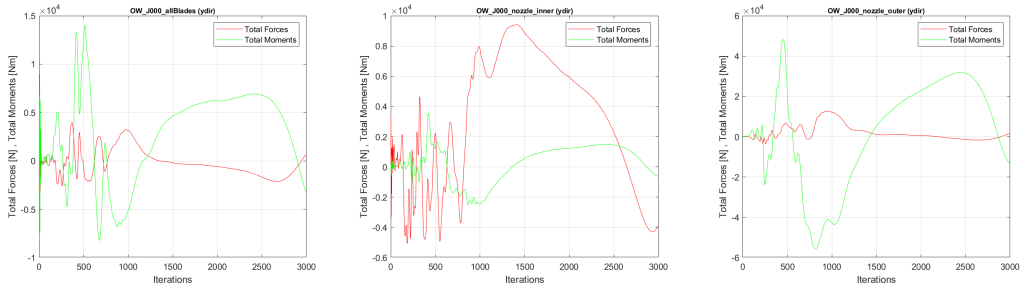

(a) MRF.

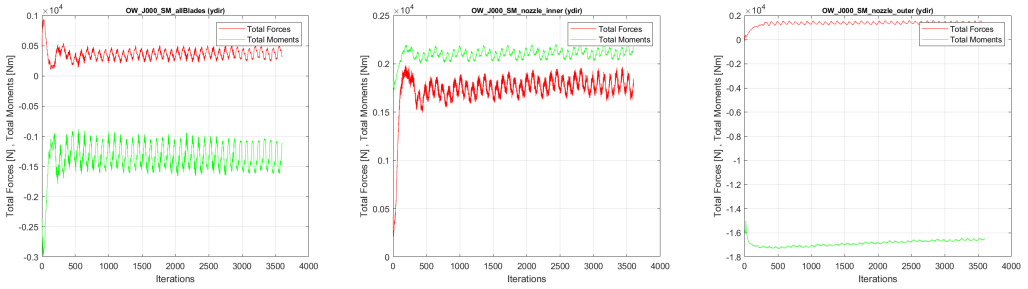

(b) SMI.

Figure A.15: Simulations at $J = 0.00$.

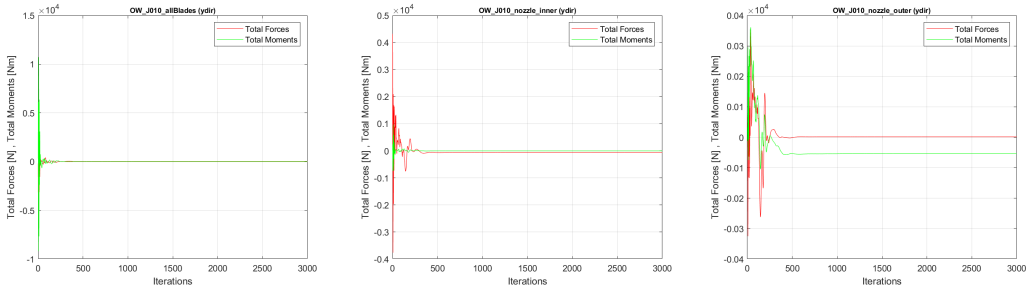

Figure A.16: MRF simulation of Case 1 at $J = 0.10$.

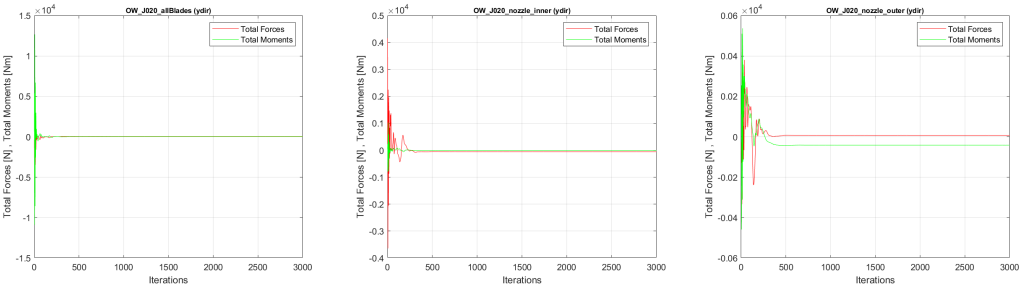

(a) MRF.

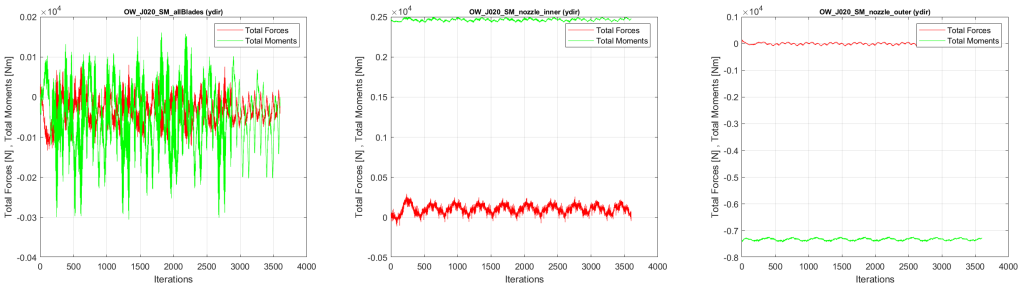

(b) SMI.

Figure A.17: Simulations at $J = 0.20$.

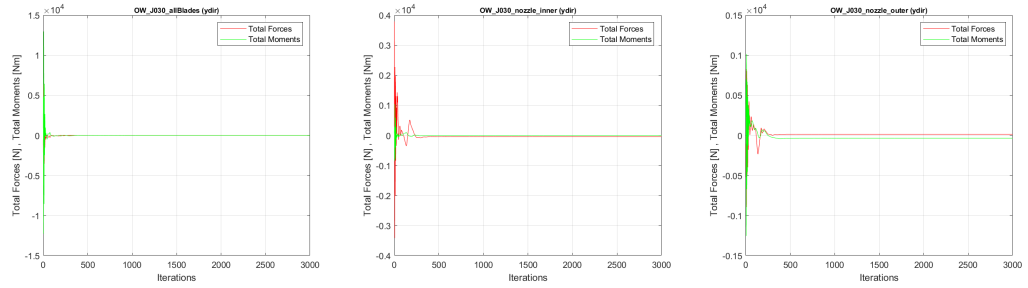

Figure A.18: MRF simulation of Case 1 at $J = 0.30$.

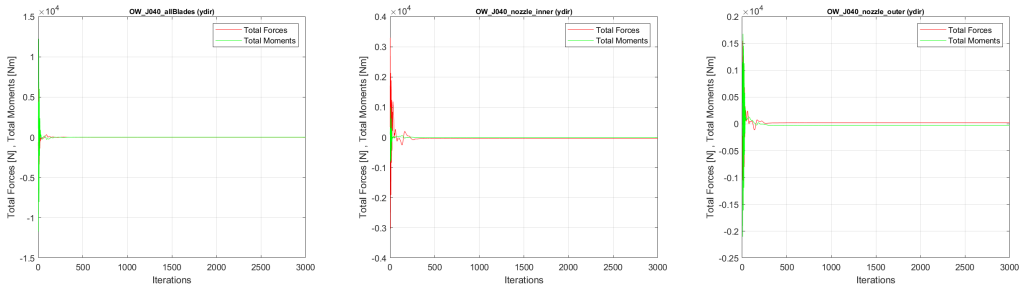

(a) MRF.

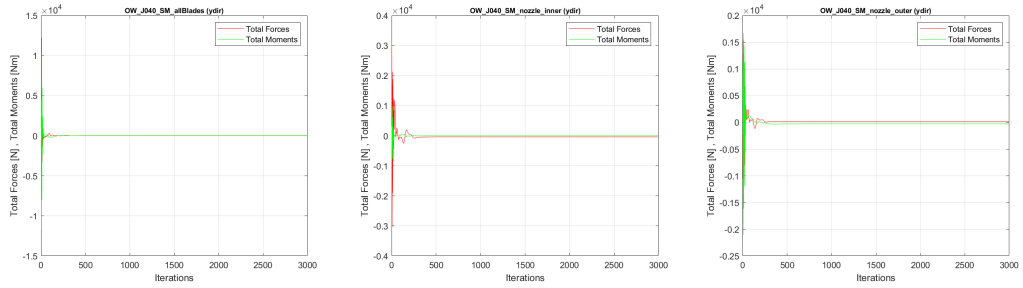

(b) SMI.

Figure A.19: Simulations at $J = 0.40$.

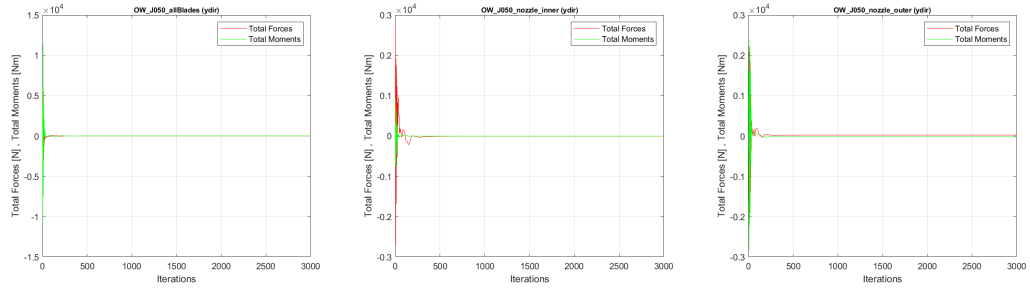

Figure A.20: MRF simulation of Case 1 at $J = 0.50$.

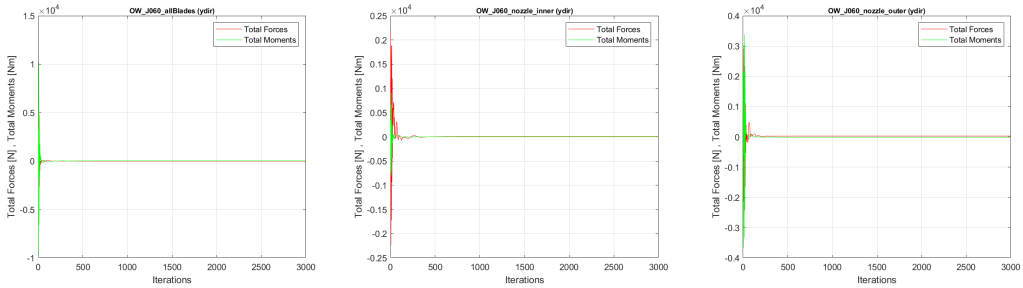

(a) MRF.

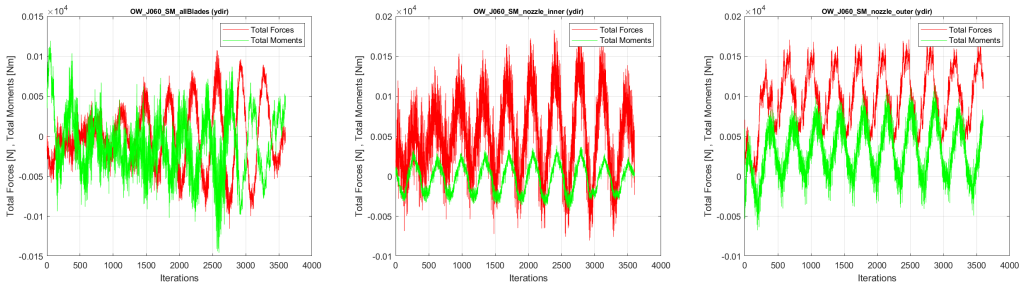

(b) SMI.

Figure A.21: Simulations at $J = 0.60$.

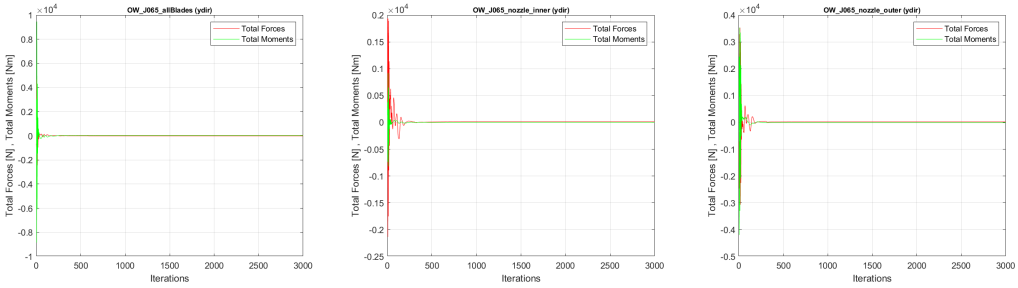

Figure A.22: MRF simulation of Case 1 at $J = 0.65$.

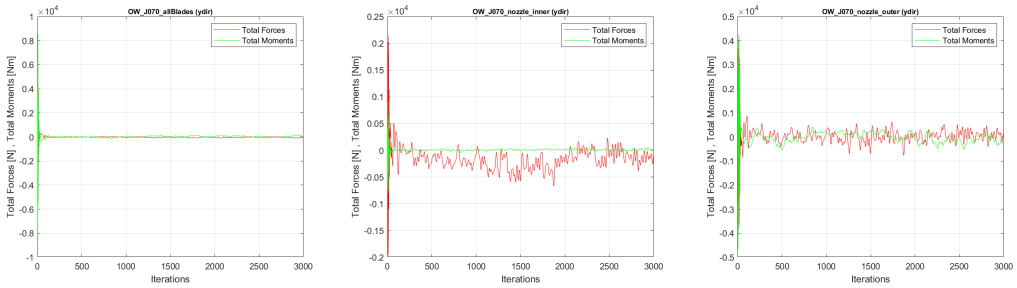

Figure A.23: MRF simulation of Case 1 at $J = 0.70$.

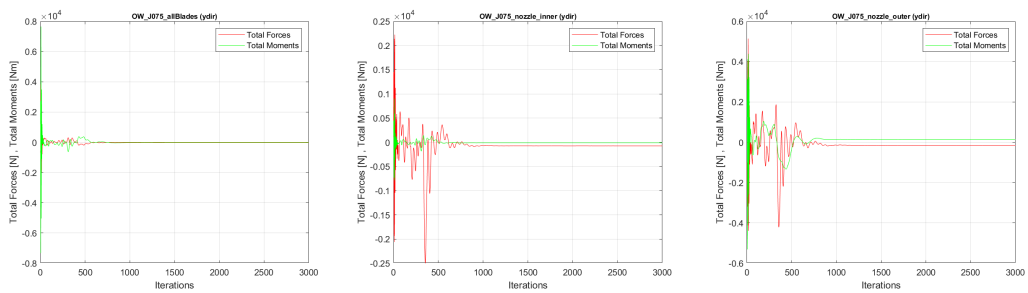

Figure A.24: MRF simulation of Case 1 at $J = 0.75$.

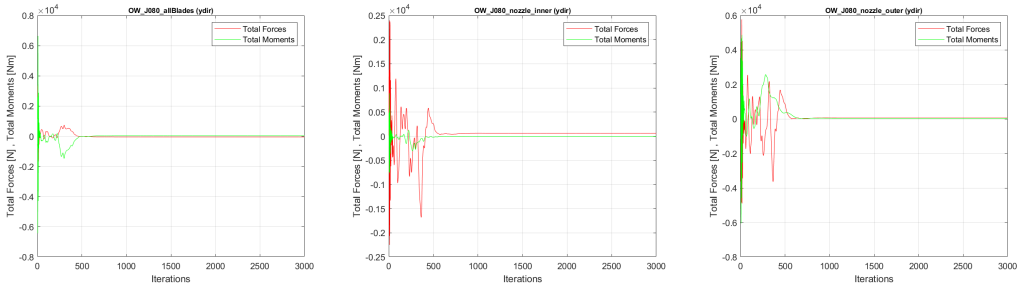

(a) MRF.

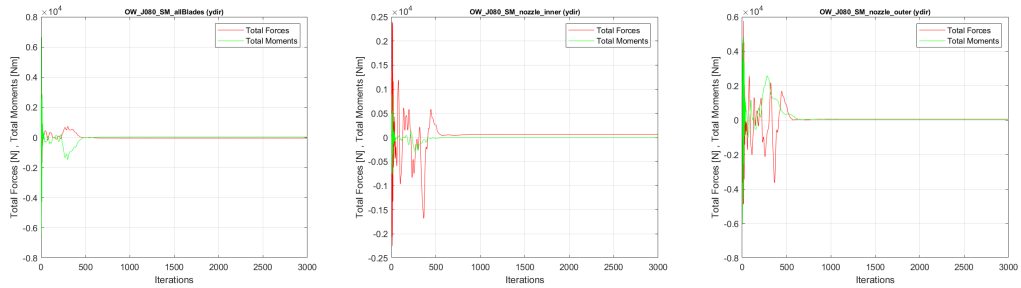

(b) SMI.

Figure A.25: Simulations at $J = 0.80$.

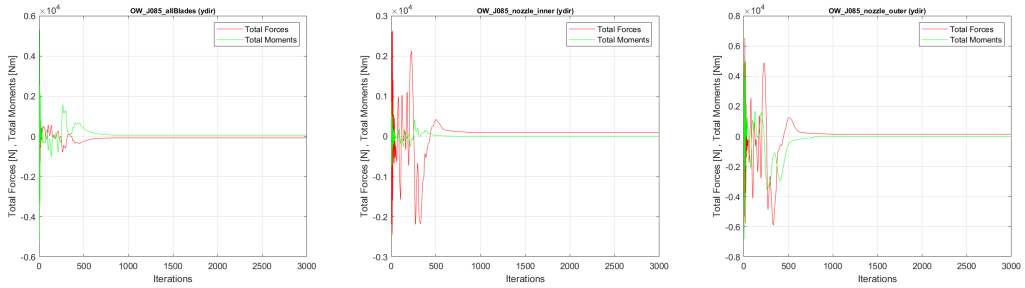

Figure A.26: MRF simulation of Case 1 at $J = 0.85$.

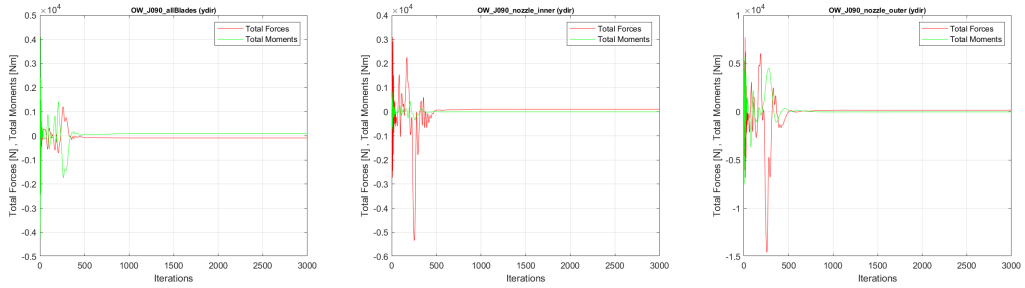

Figure A.27: MRF simulation of Case 1 at $J = 0.90$.

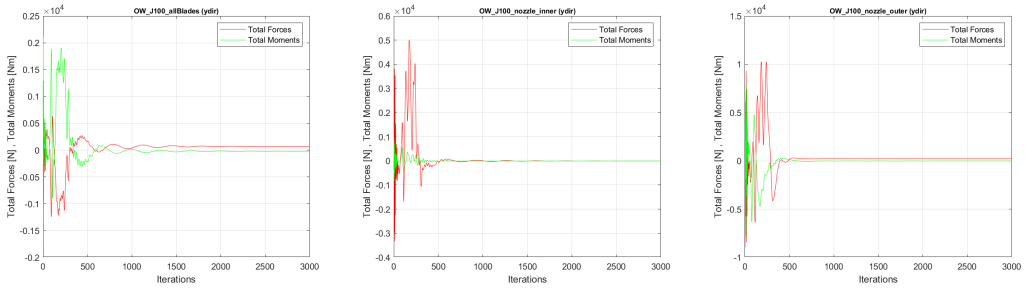

Figure A.28: MRF simulation of Case 1 at $J = 1.00$.

z-dir

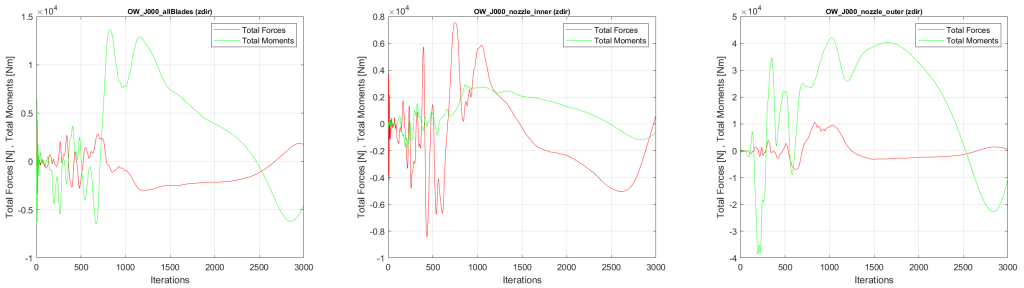

(a) MRF.

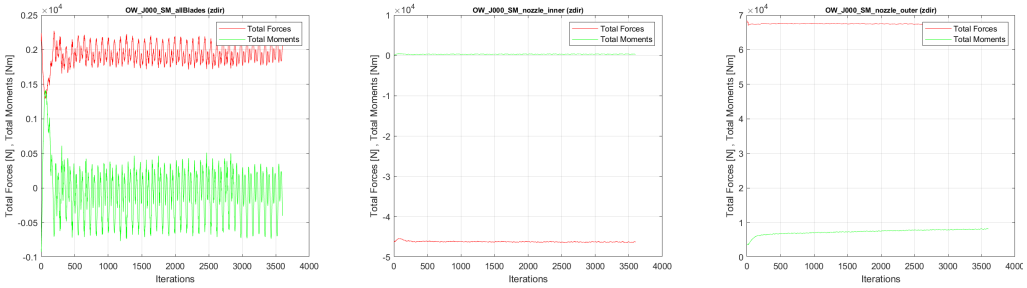

(b) SMI.

Figure A.29: Simulations at $J = 0.00$.

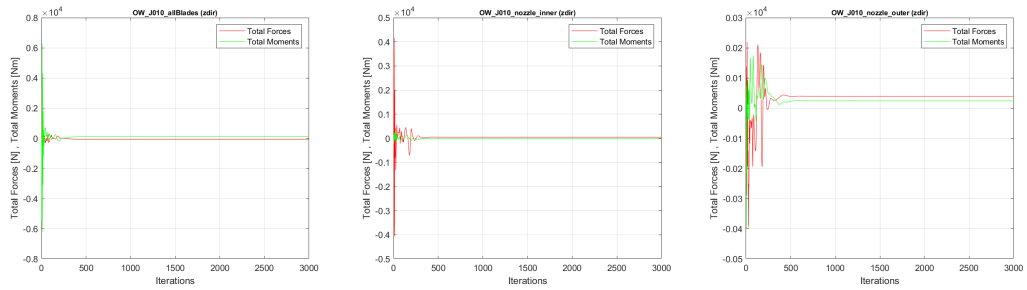

Figure A.30: MRF simulation of Case 1 at $J = 0.10$.

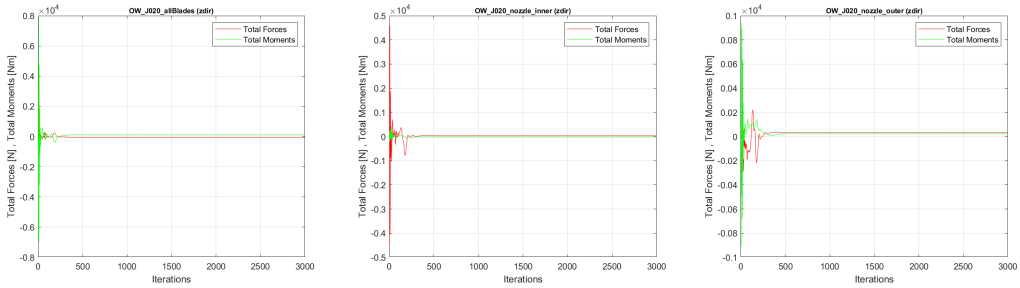

(a) MRF.

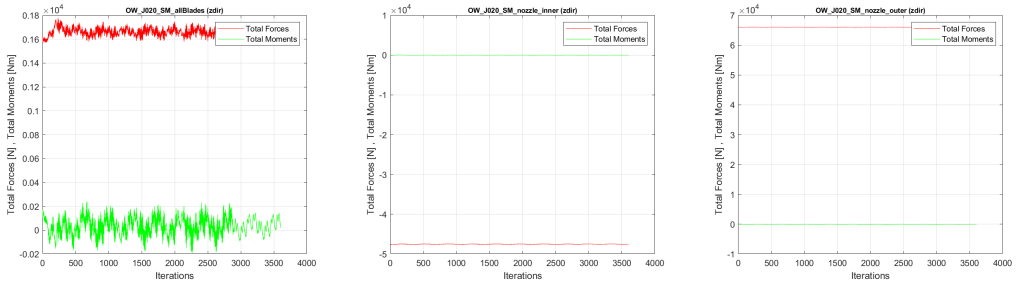

(b) SMI.

Figure A.31: Simulations at $J = 0.20$.

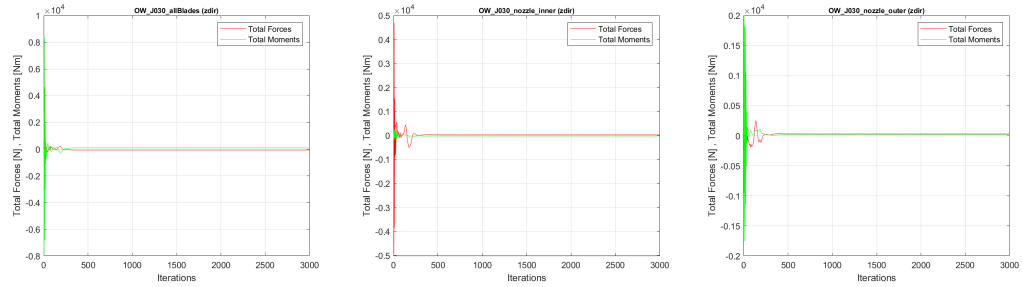

Figure A.32: MRF simulation of Case 1 at $J = 0.30$.

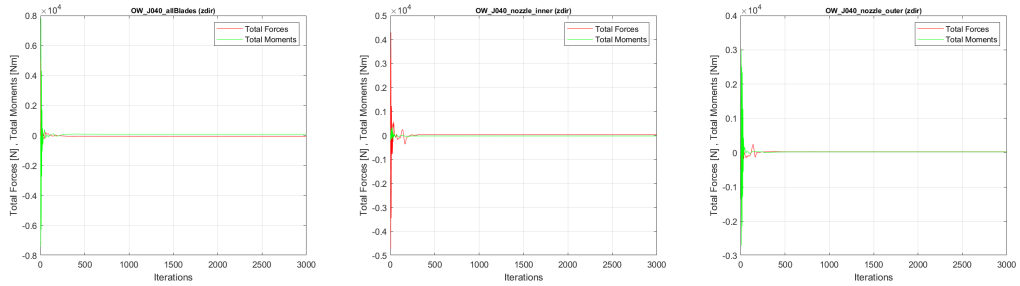

(a) MRF.

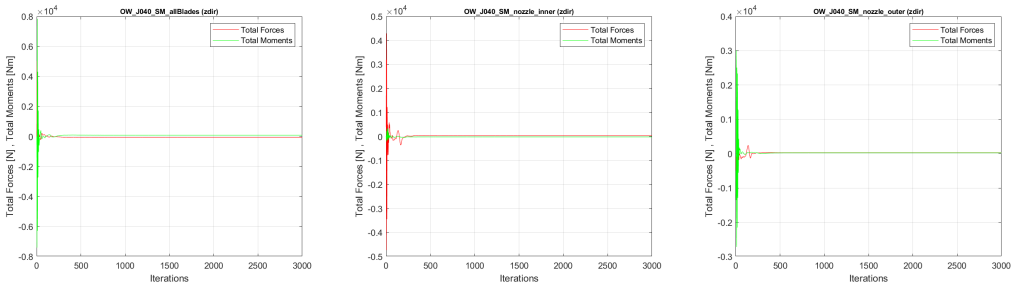

(b) SMI.

Figure A.33: Simulations at $J = 0.40$.

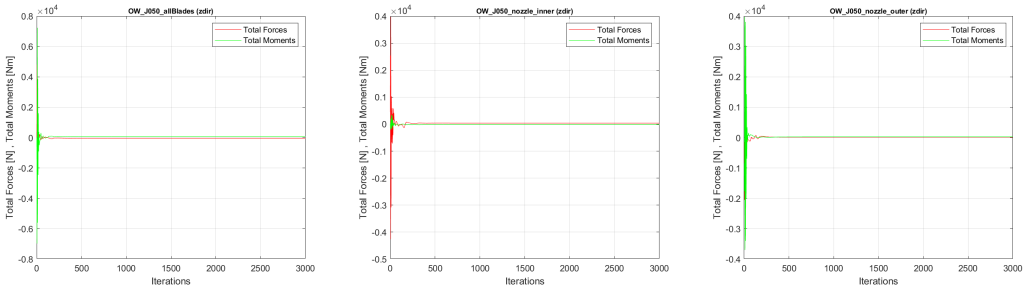

Figure A.34: MRF simulation of Case 1 at $J = 0.50$.

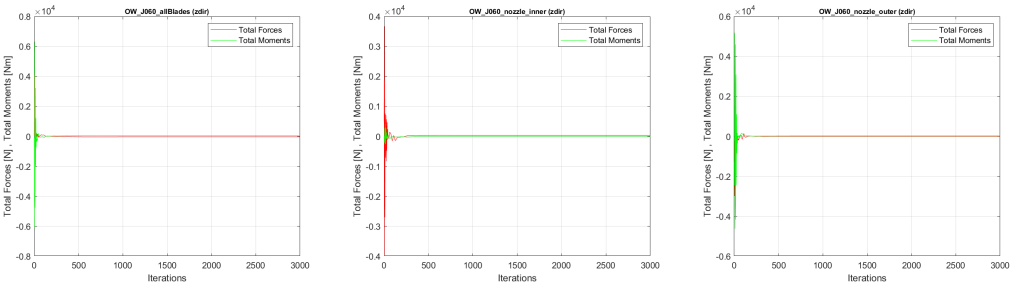

(a) MRF.

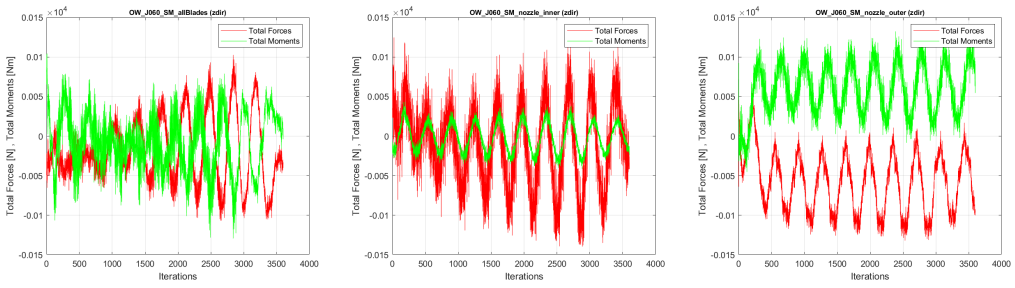

(b) SMI.

Figure A.35: Simulations at $J = 0.60$.

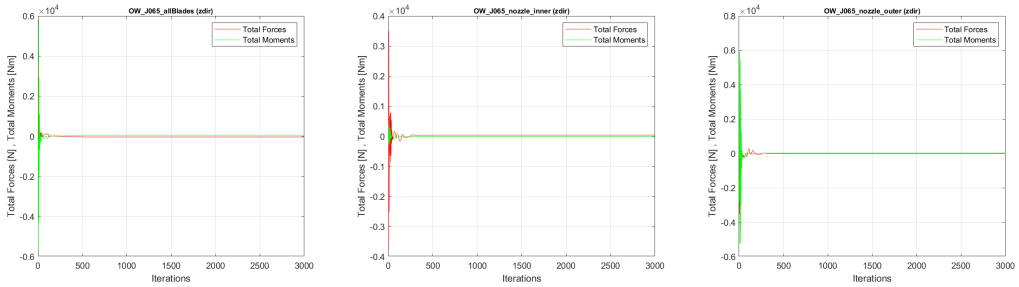

Figure A.36: MRF simulation of Case 1 at $J = 0.65$.

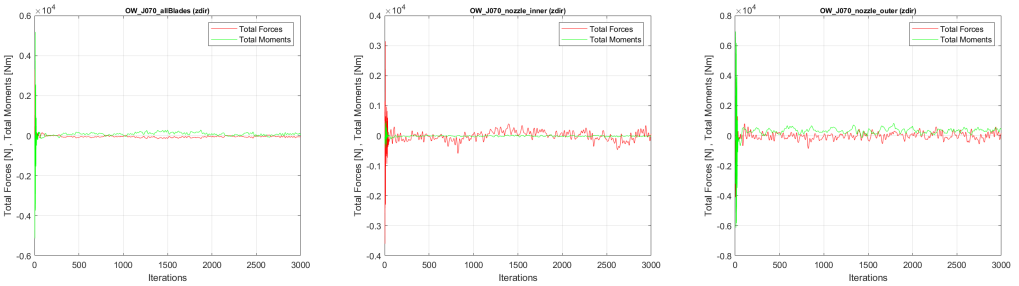

Figure A.37: MRF simulation of Case 1 at $J = 0.70$.

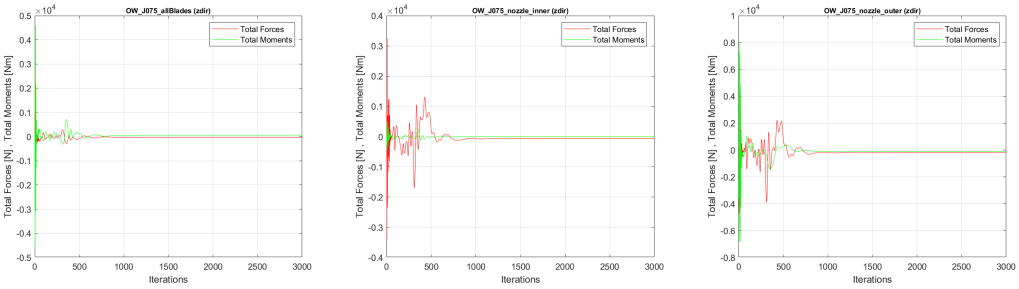

Figure A.38: MRF simulation of Case 1 at $J = 0.75$.

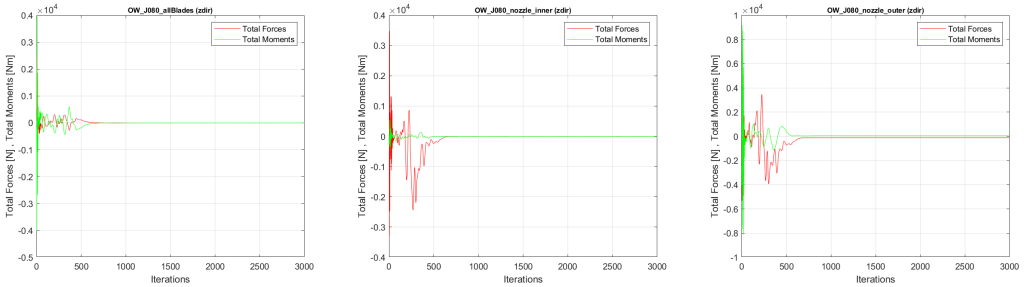

(a) MRF.

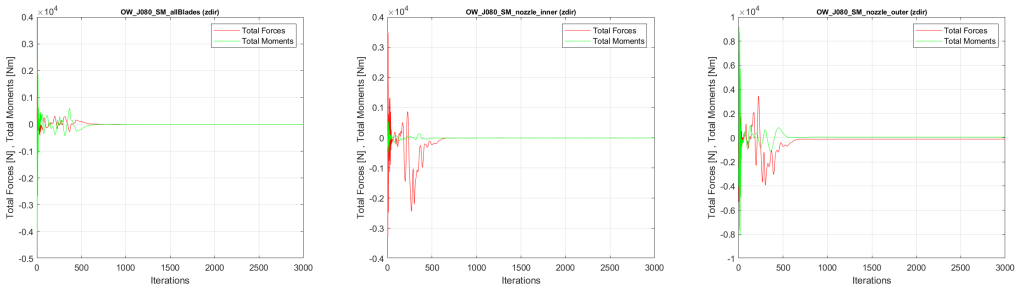

(b) SMI.

Figure A.39: Simulations at $J = 0.80$.

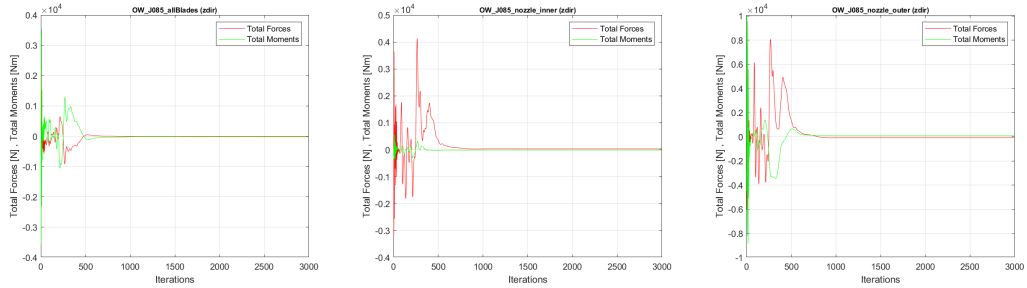

Figure A.40: MRF simulation of Case 1 at $J = 0.85$.

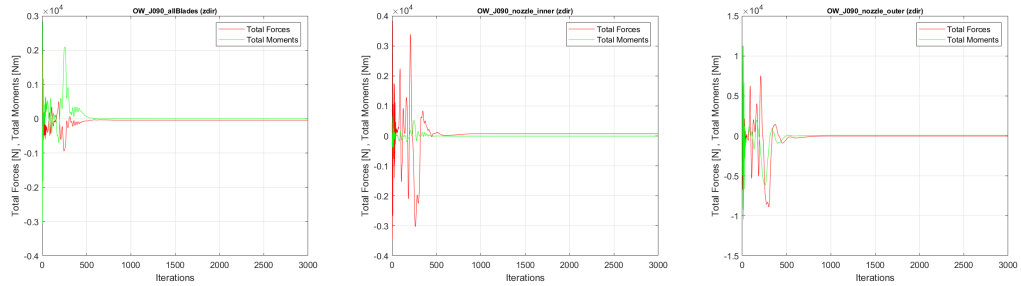

Figure A.41: MRF simulation of Case 1 at $J = 0.90$.

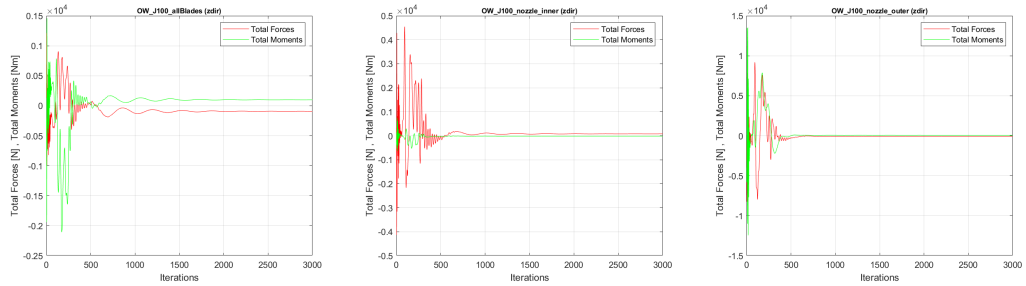

Figure A.42: MRF simulation of Case 1 at $J = 1.00$.

A.2 Convergence plots of Case 2

x-dir

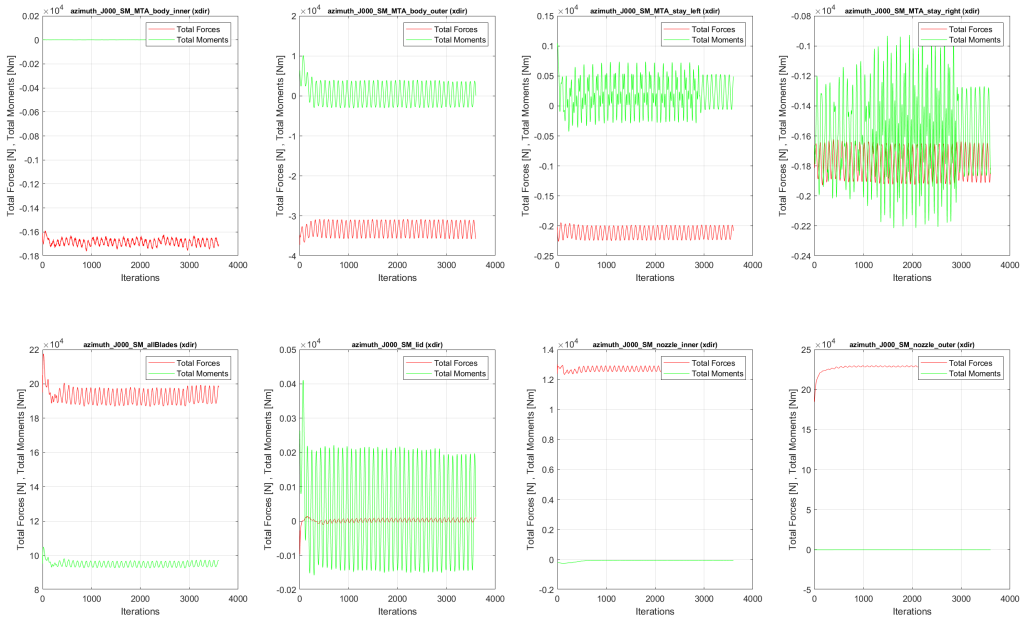

Figure A.43: SMI simulation of Case 2 at $J = 0.00$.

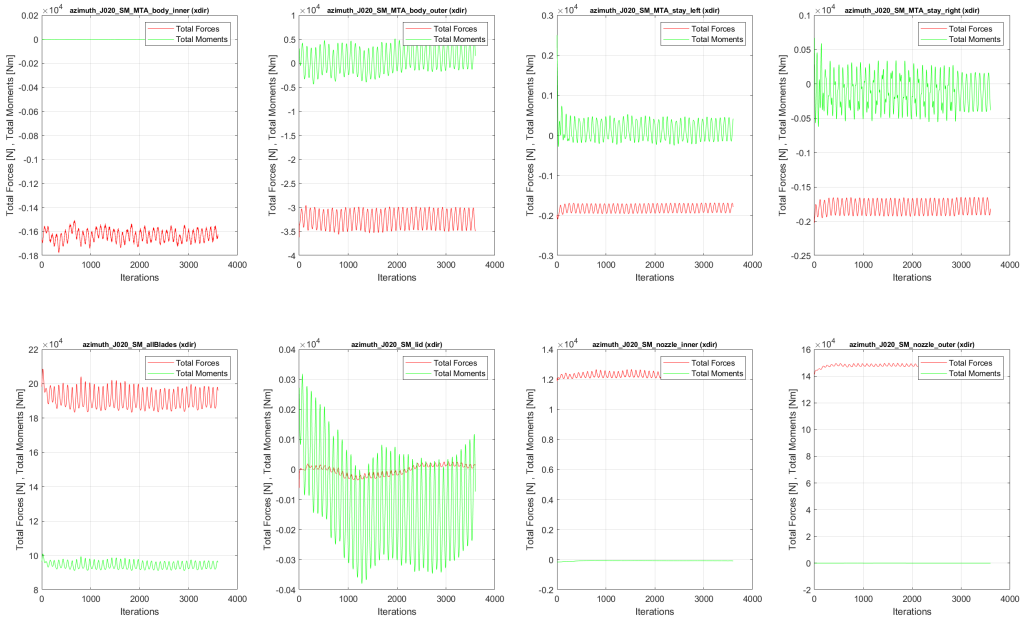

Figure A.44: SMI simulation of Case 2 at $J = 0.20$.

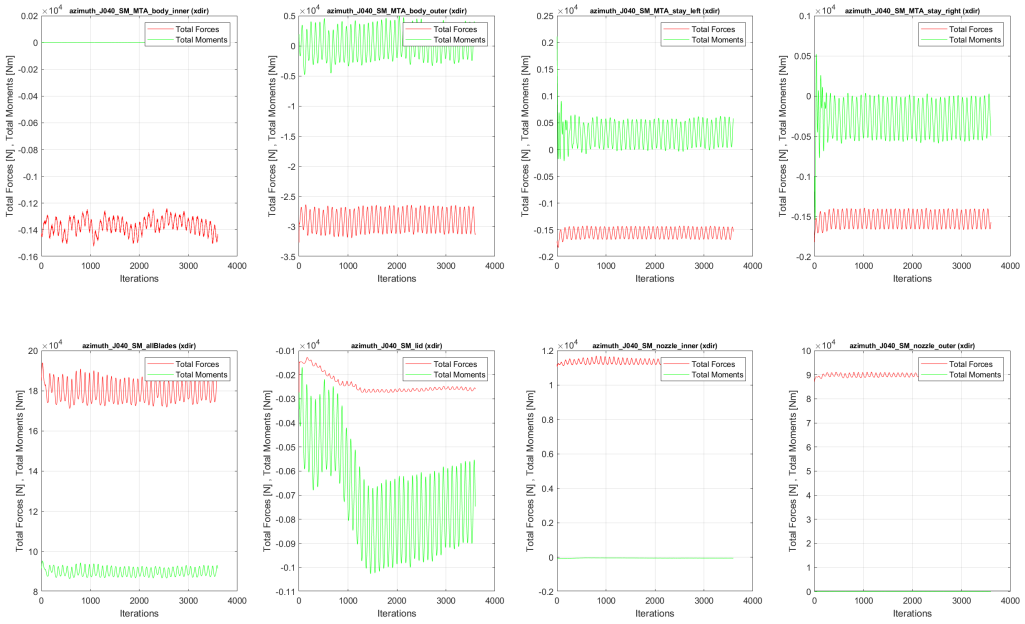

Figure A.45: SMI simulation of Case 2 at $J = 0.40$.

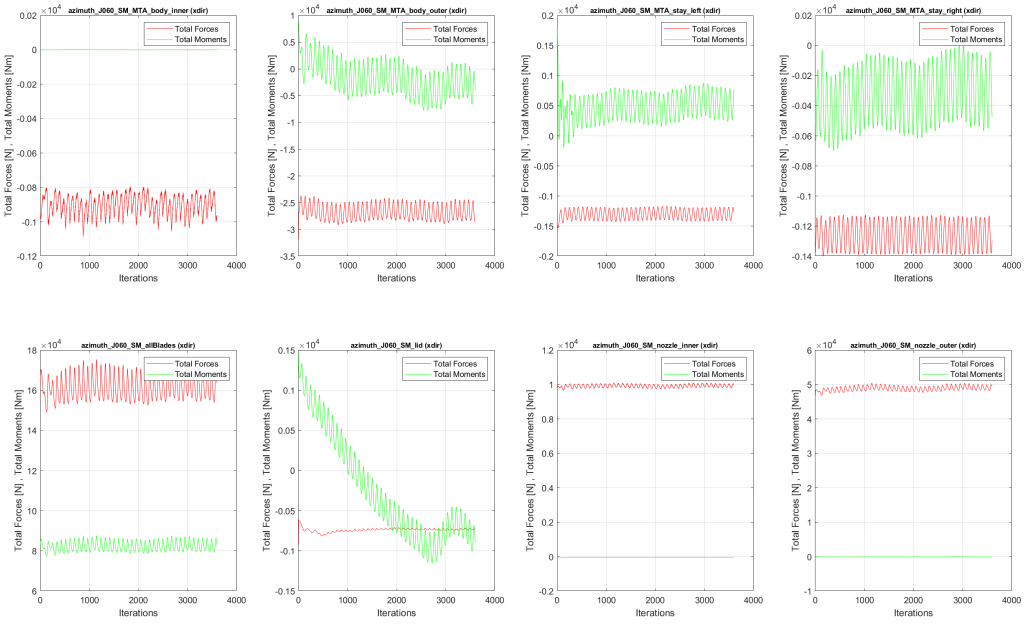

Figure A.46: SMI simulation of Case 2 at $J = 0.60$.

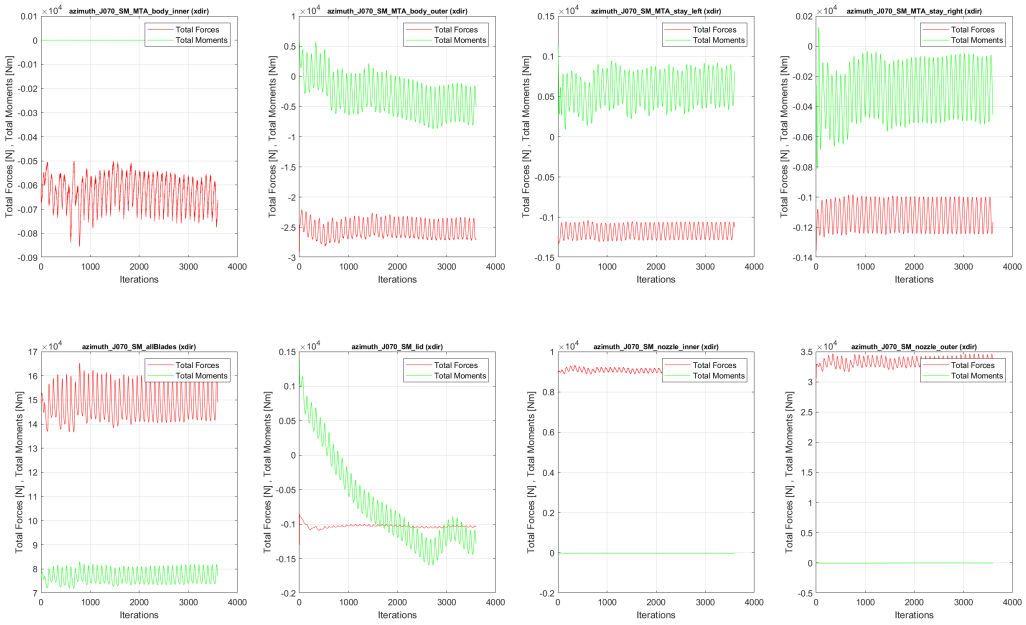

Figure A.47: SMI simulation of Case 2 at $J = 0.70$.

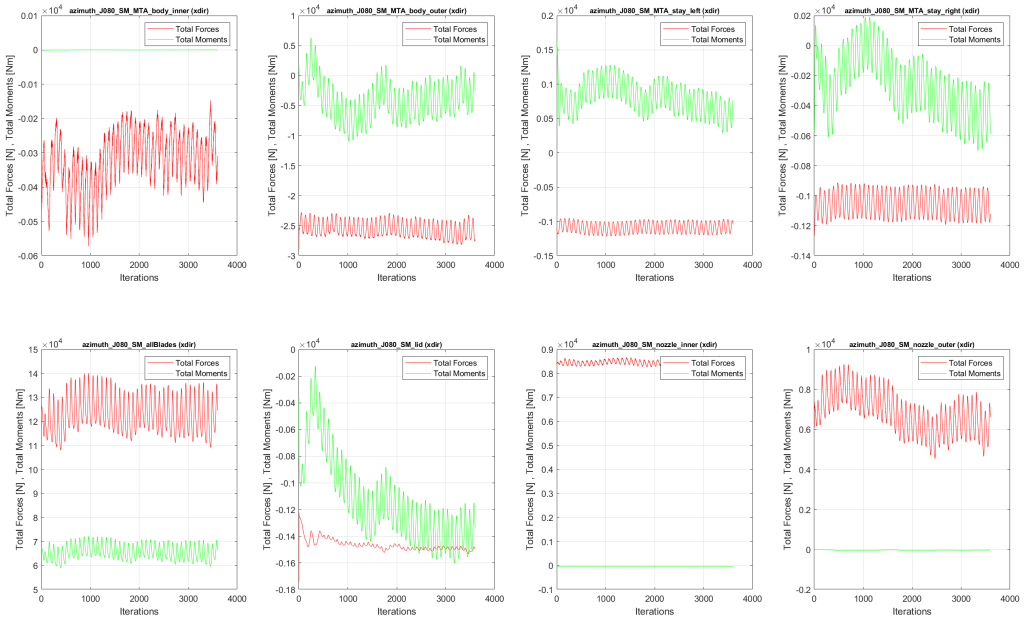

Figure A.48: SMI simulation of Case 2 at $J = 0.80$.

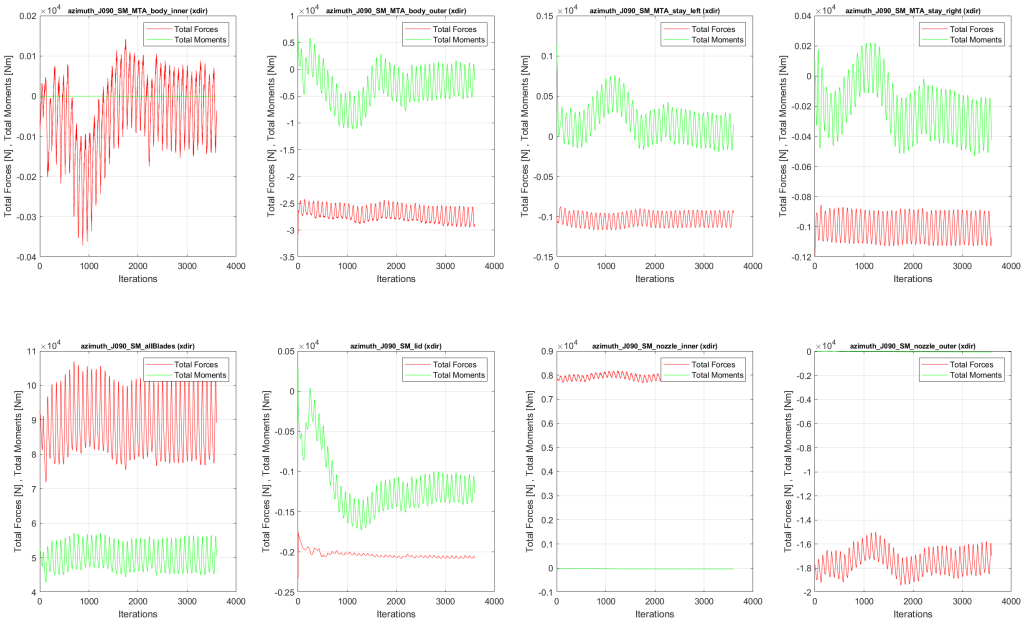

Figure A.49: SMI simulation of Case 2 at $J = 0.90$.

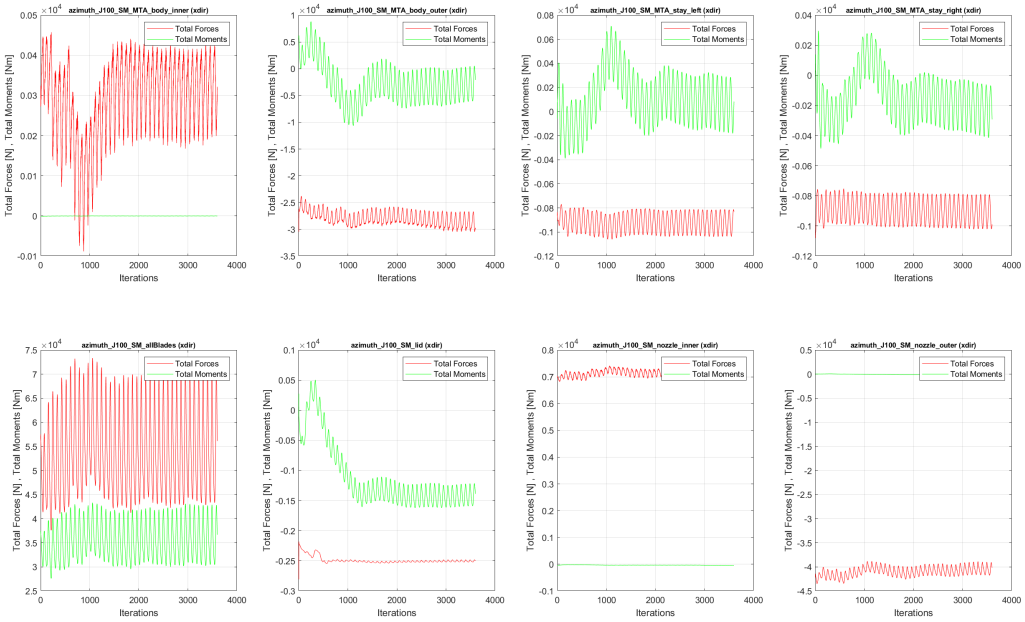

Figure A.50: SMI simulation of Case 2 at $J = 1.00$.

y-dir

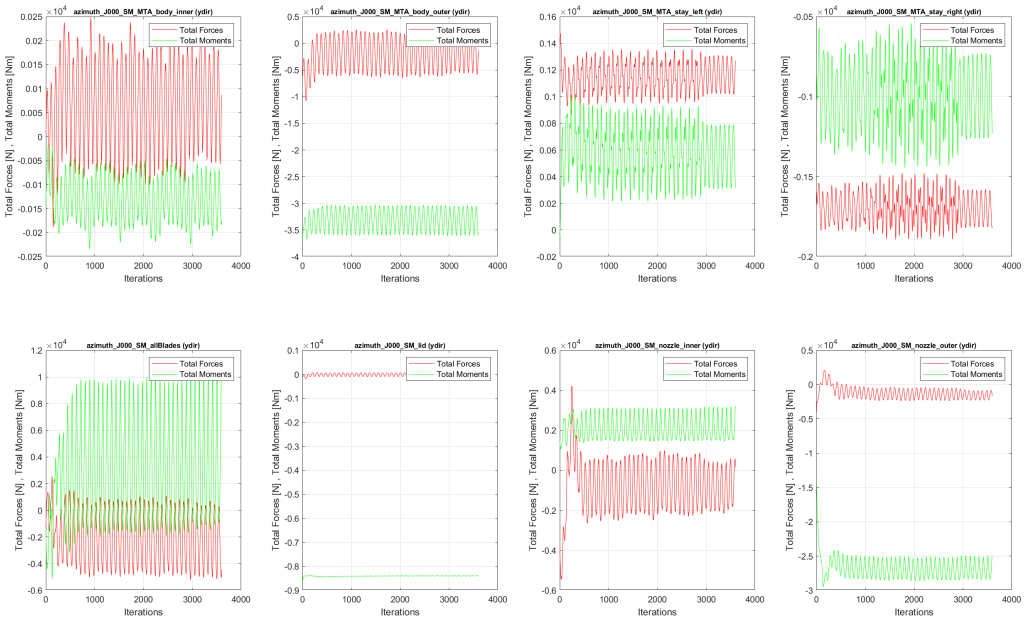

Figure A.51: SMI simulation of Case 2 at $J = 0.00$.

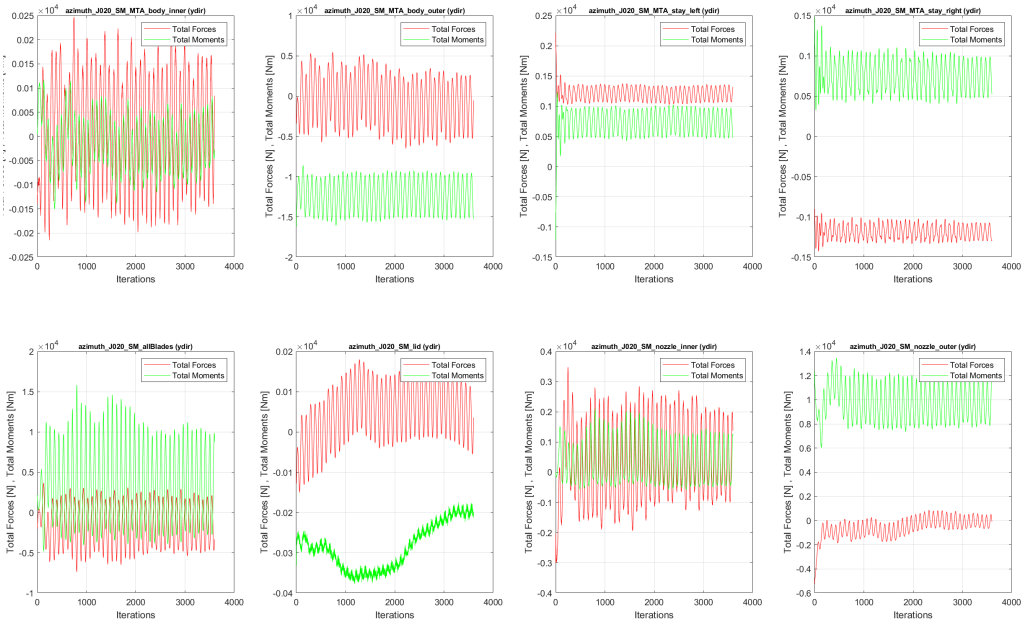

Figure A.52: SMI simulation of Case 2 at $J = 0.20$.

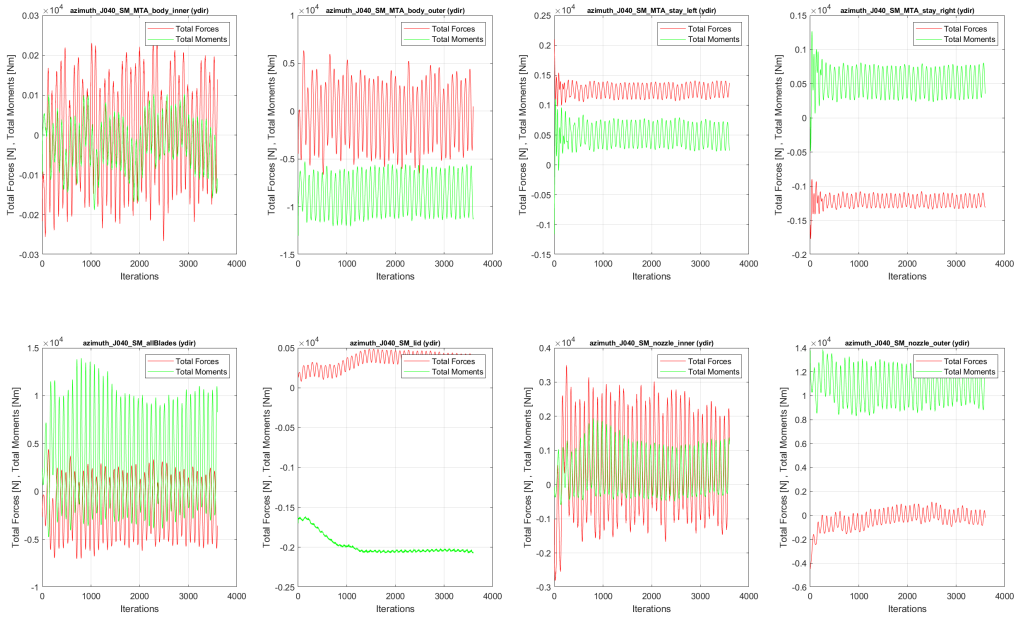

Figure A.53: SMI simulation of Case 2 at $J = 0.40$.

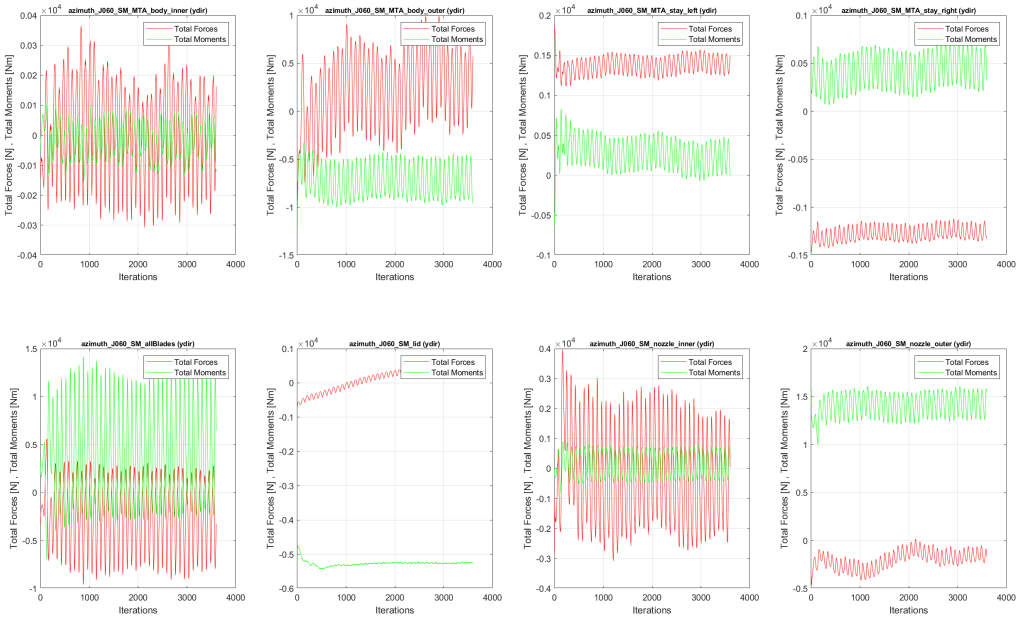

Figure A.54: SMI simulation of Case 2 at $J = 0.60$.

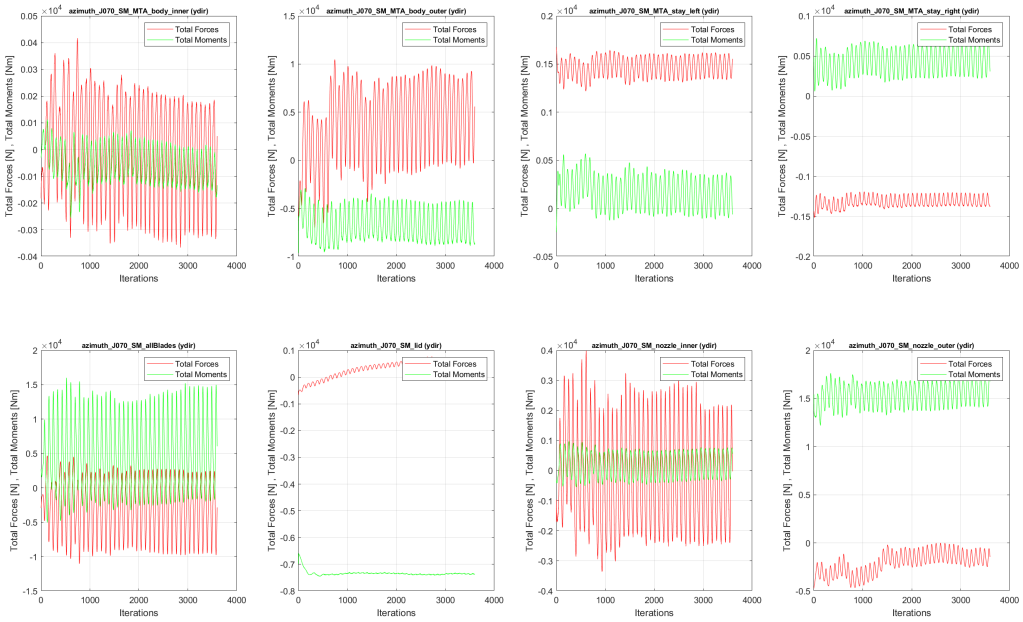

Figure A.55: SMI simulation of Case 2 at $J = 0.70$.

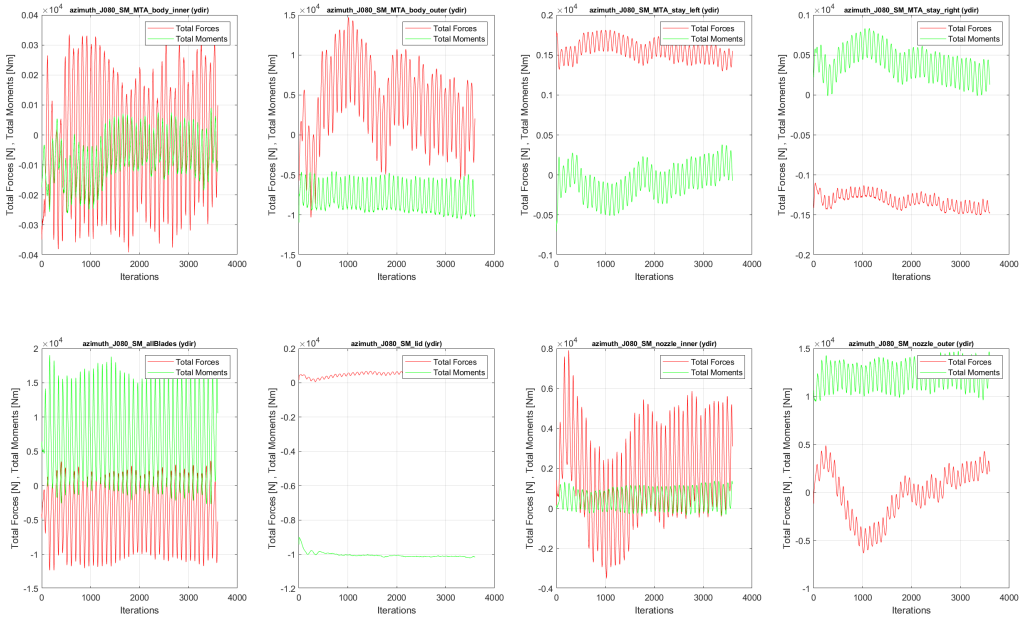

Figure A.56: SMI simulation of Case 2 at $J = 0.80$.

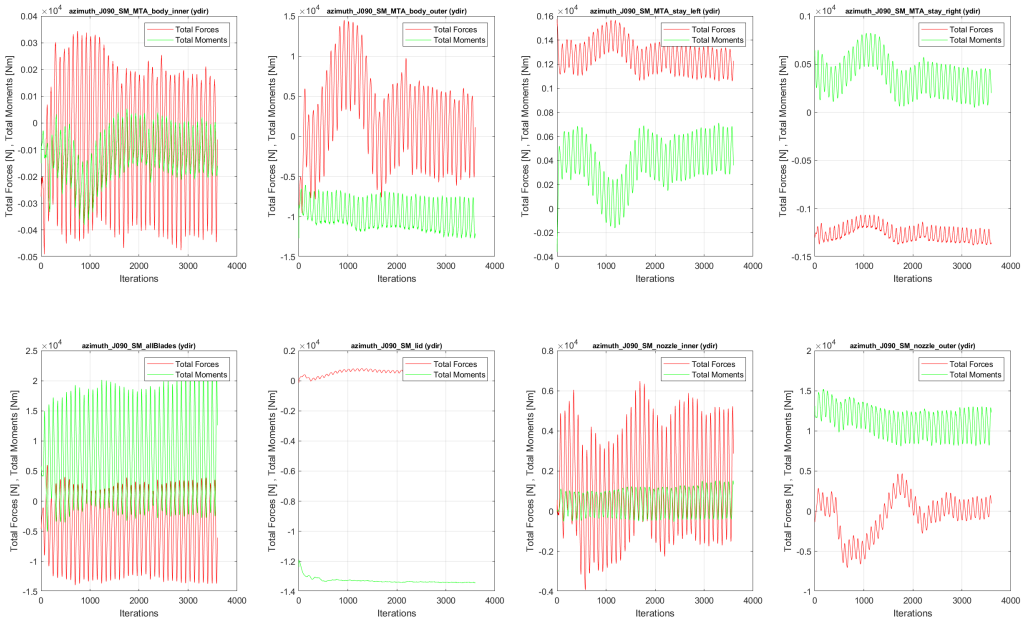

Figure A.57: SMI simulation of Case 2 at $J = 0.90$.

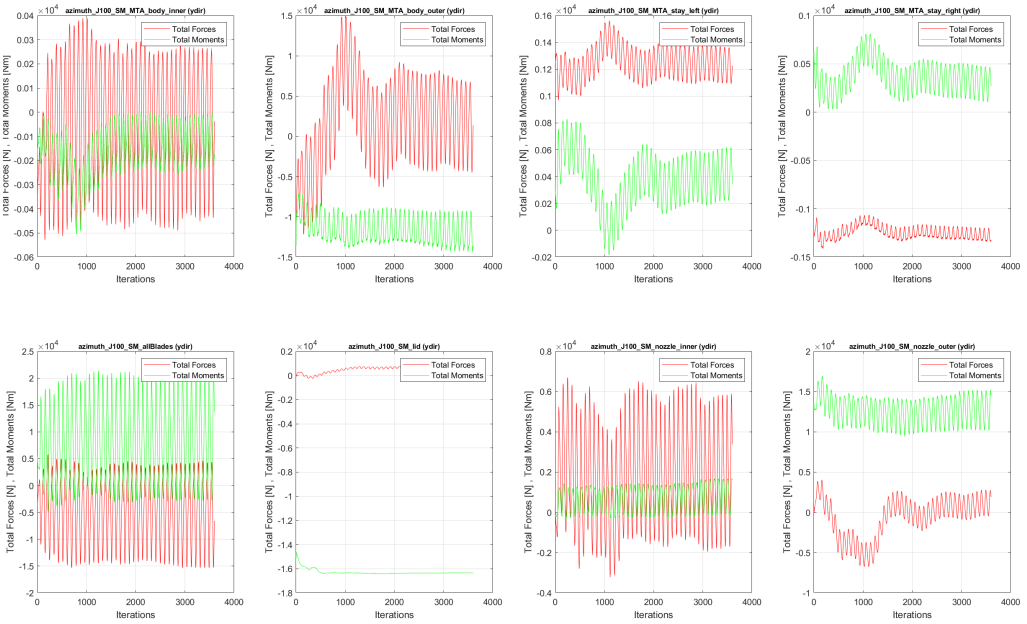

Figure A.58: SMI simulation of Case 2 at $J = 1.00$.

z-dir

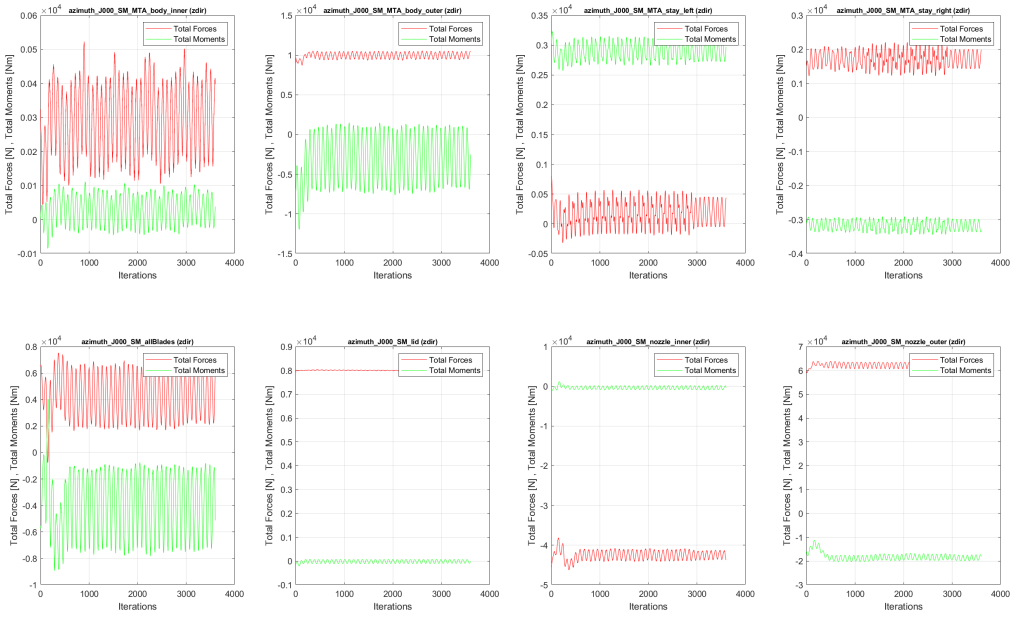

Figure A.59: SMI simulation of Case 2 at $J = 0.00$.

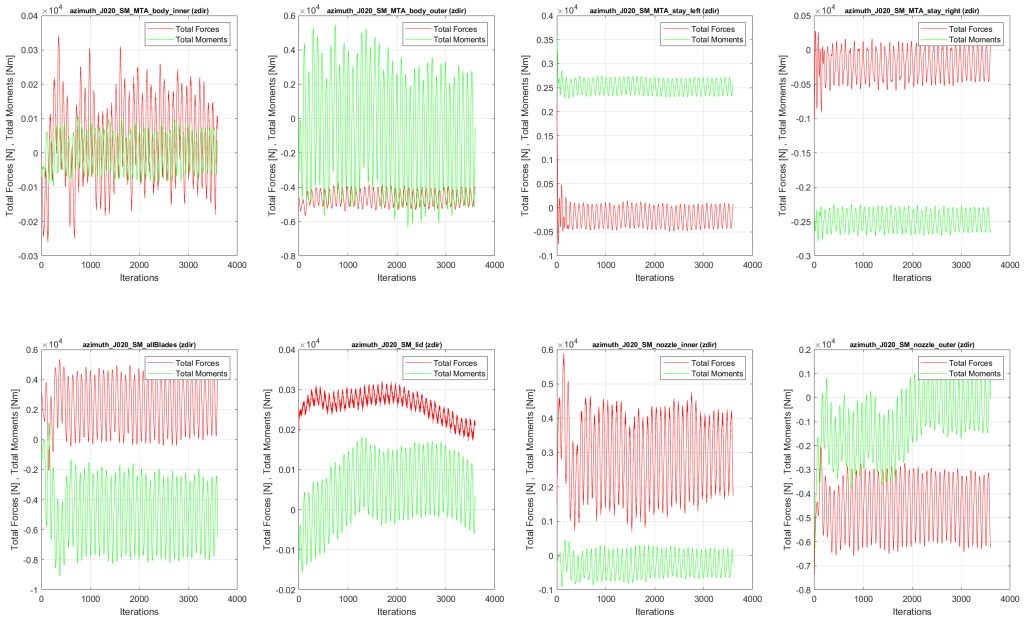

Figure A.60: SMI simulation of Case 2 at $J = 0.20$.

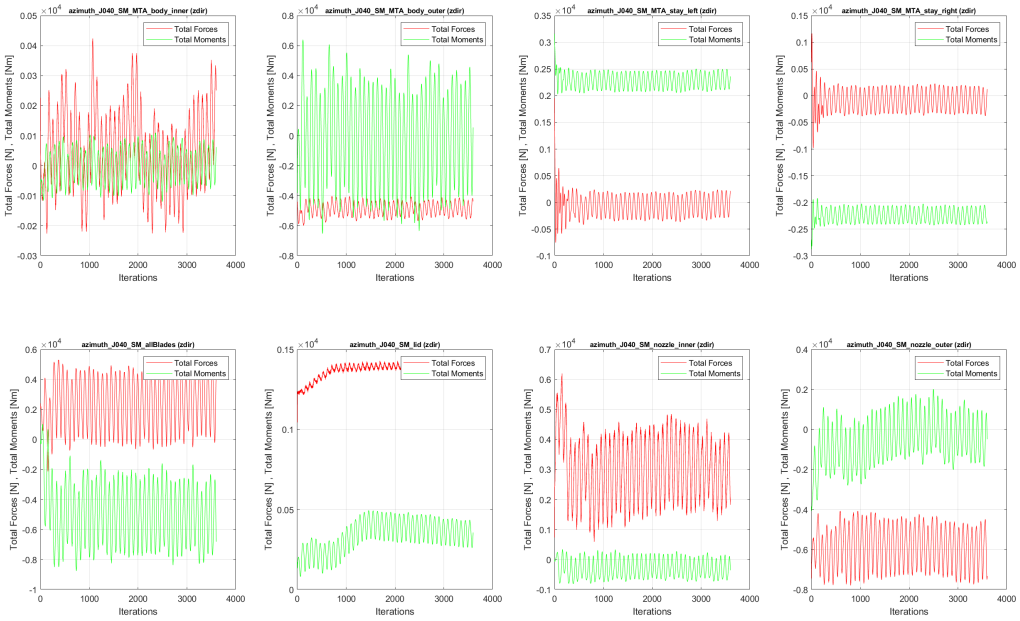

Figure A.61: SMI simulation of Case 2 at $J = 0.40$.

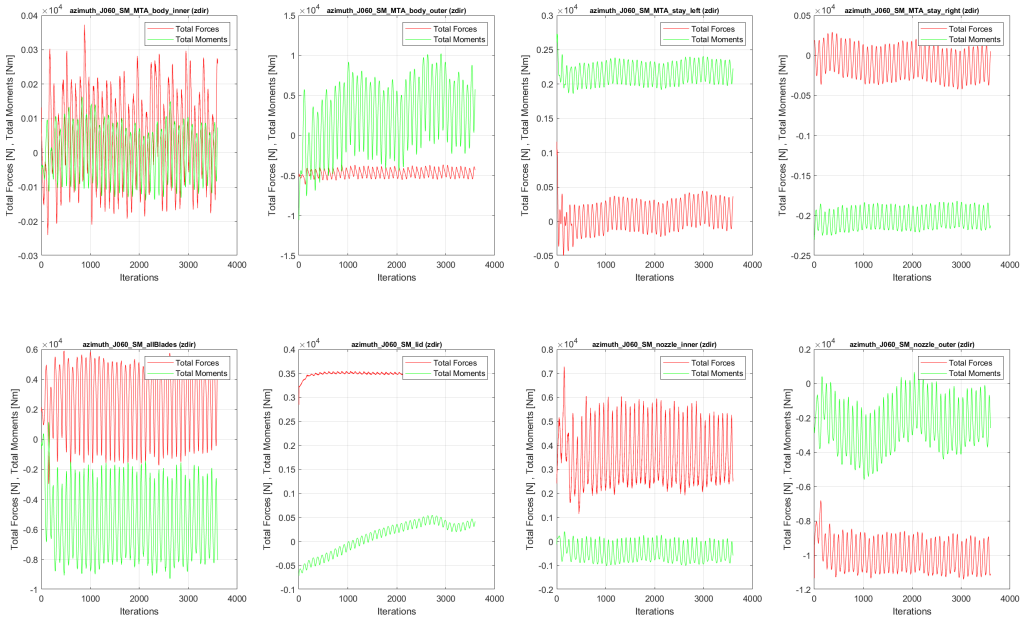

Figure A.62: SMI simulation of Case 2 at $J = 0.60$.

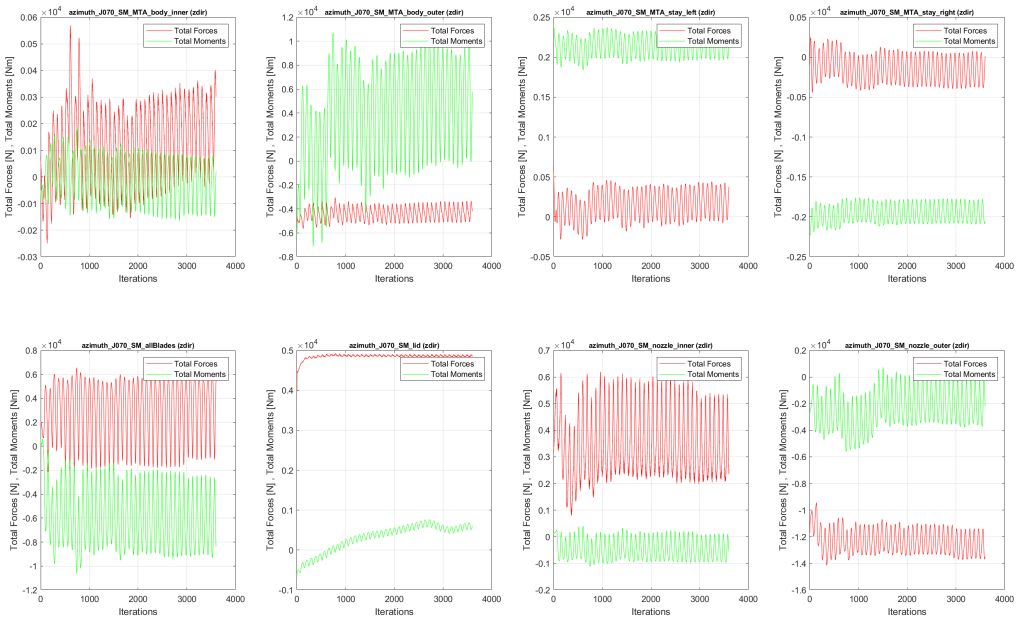

Figure A.63: SMI simulation of Case 2 at $J = 0.70$.

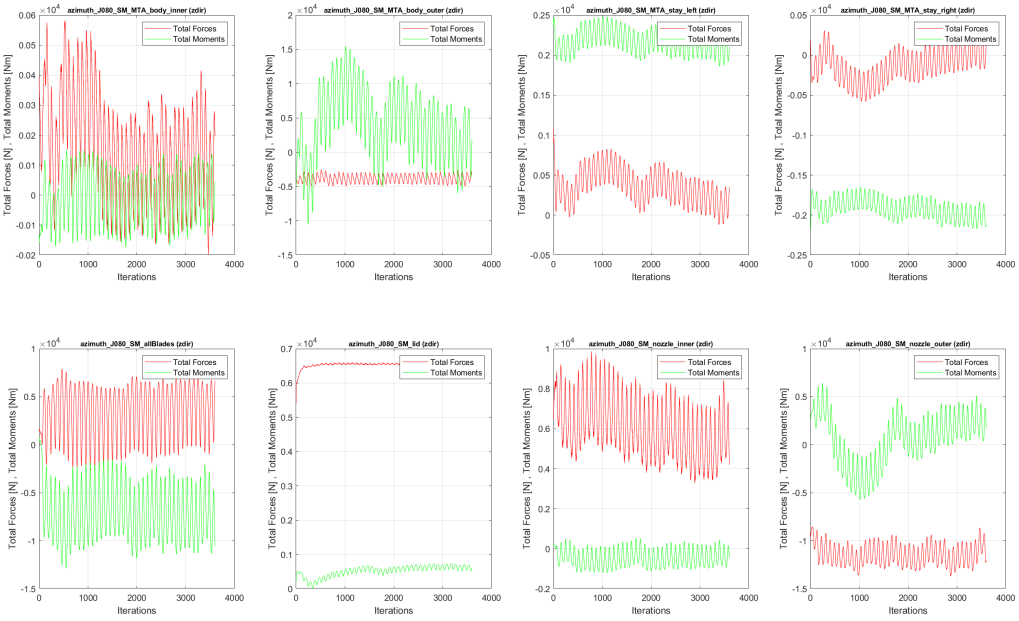

Figure A.64: SMI simulation of Case 2 at $J = 0.80$.

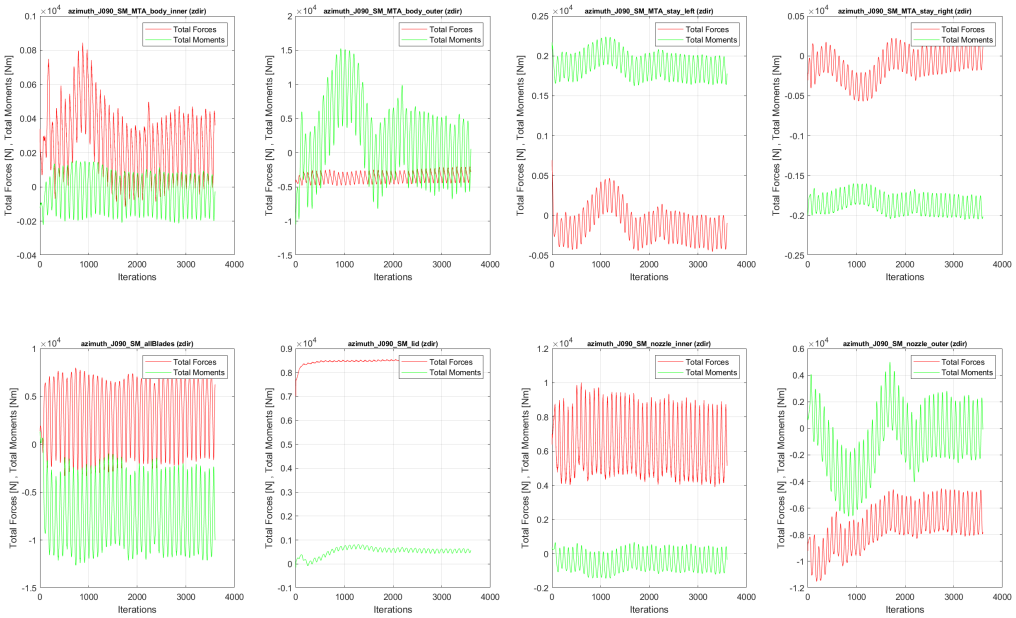

Figure A.65: SMI simulation of Case 2 at $J = 0.90$.

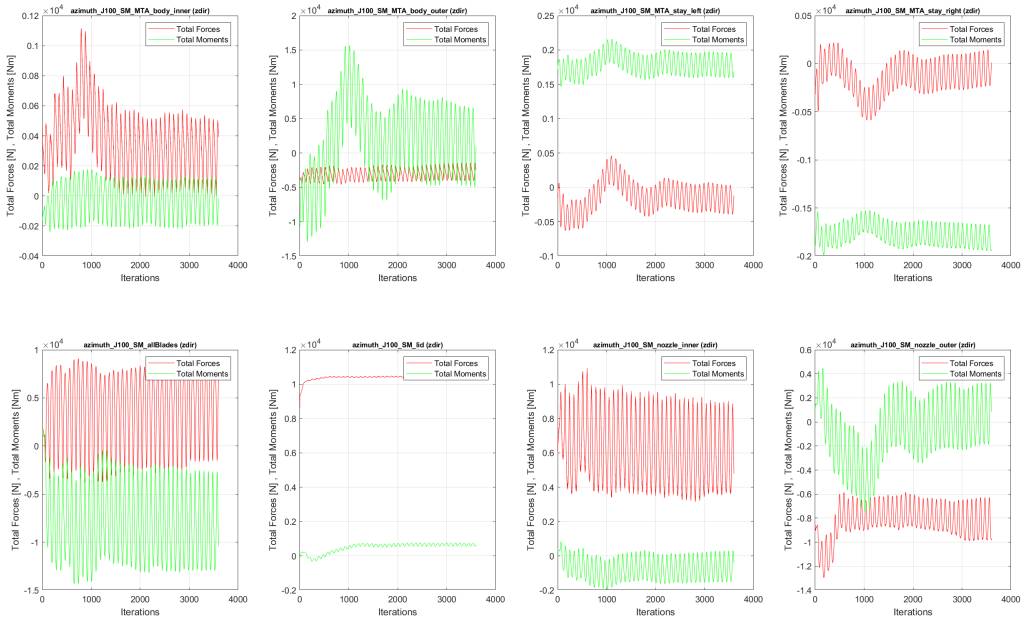

Figure A.66: SMI simulation of Case 2 at $J = 1.00$.

A.3 Convergence plots of Case 3

x-dir

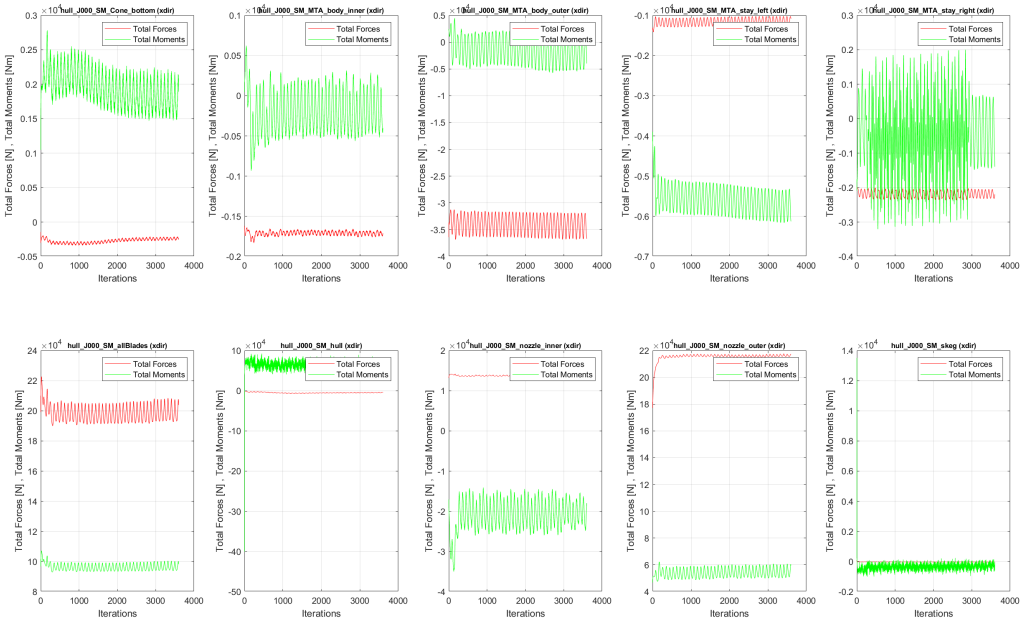

Figure A.67: SMI simulation of Case 3 at $J = 0.00$.

y-dir

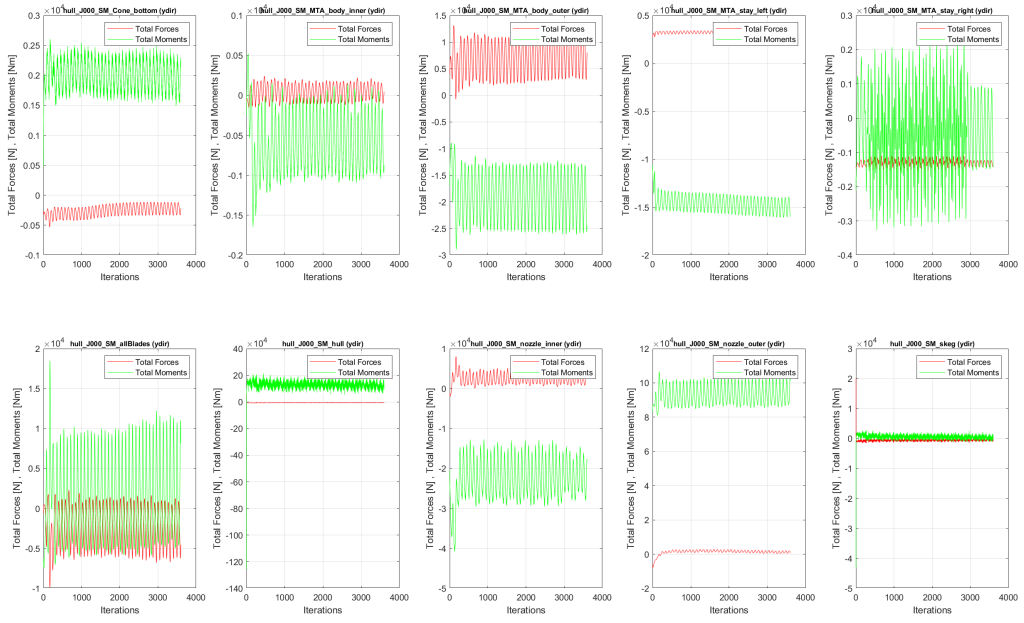

Figure A.68: SMI simulation of Case 3 at $J = 0.00$.

z-dir

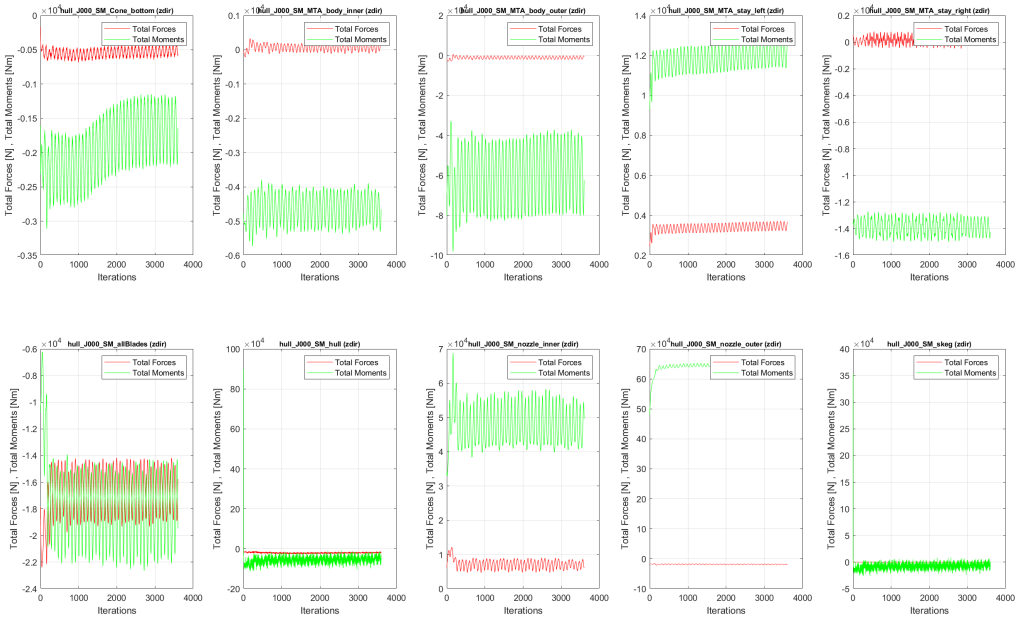

Figure A.69: SMI simulation of Case 3 at $J = 0.00$.

B

Illustration of the different surface mesh grids

In this chapter, all the initial surface meshes used within this study project are presented. First, the general mesh grids that are used in all cases are presented while later on the specific meshes used for each of the three different cases follow.

The definition of the geometry and mesh generation is done in ANSA Pre-processor v.19.0.1. In Section 2.1.2, the grid generation has been discussed. It is worth mentioning in this point that when a geometry is changed, the mesh of this geometry ends up being different as well. Thus, it is really important to acknowledge that the general mesh grids mentioned in Section B.1 are slight different from case to case.

A good example to support the statement above is the hub in Case 1 that has slightly different mesh compared to the hub in Case 2 due to the small geometrical differences that are needed in order to adapt the hub to the shaft in Case 1 (see *Figure B.5*) or to the gear case housing in Case 2 (see *Figure B.7a*). However, it is attempted that consistency of the meshes of the same parts between the different cases is kept, thus the meshes are considered almost identical.

B.1 General mesh grids used in all cases

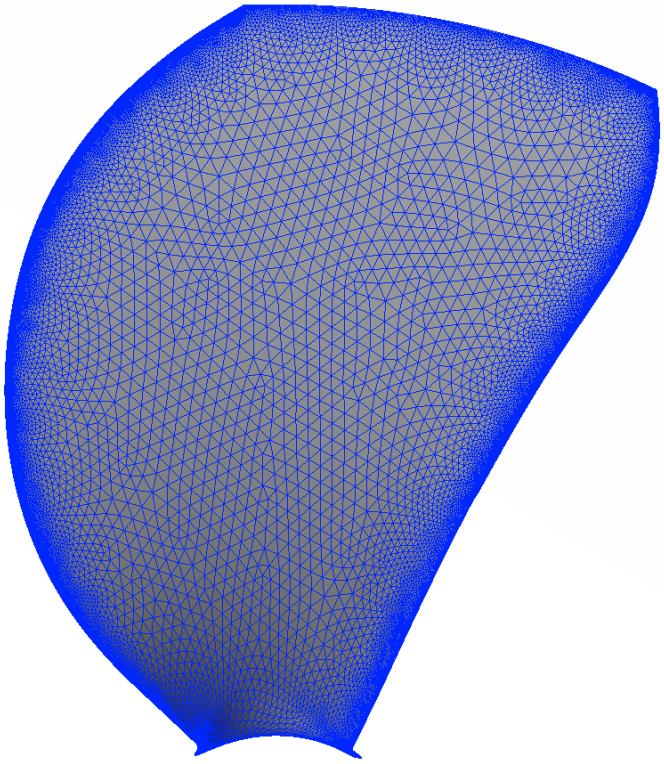

(a) Profile view of the blade.

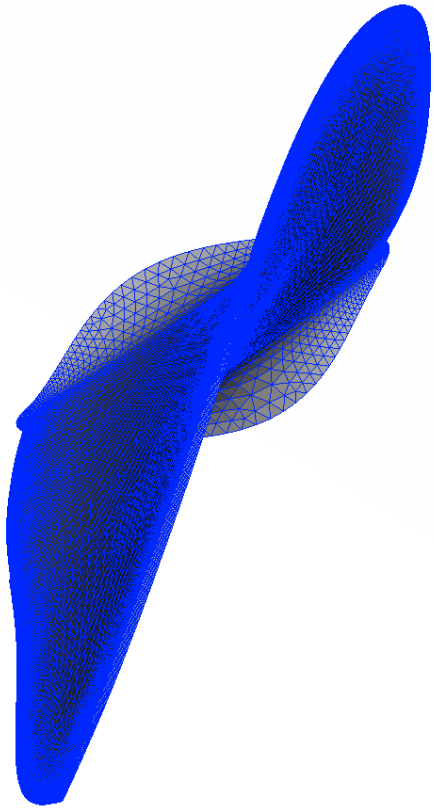

(b) Top view of the blade.

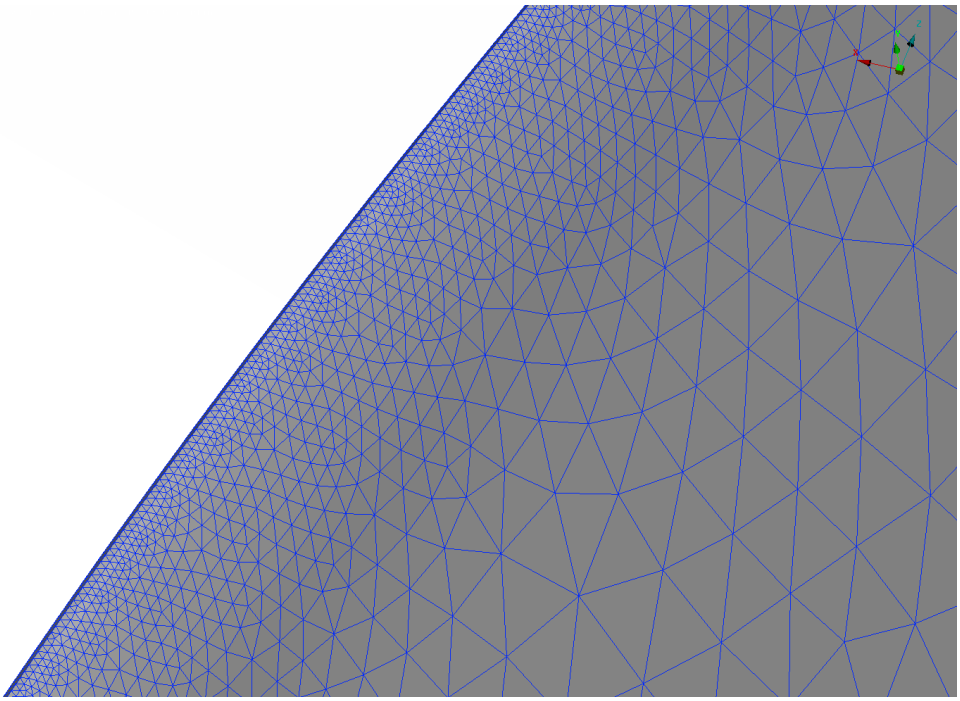

(c) Leading edge of the blade.

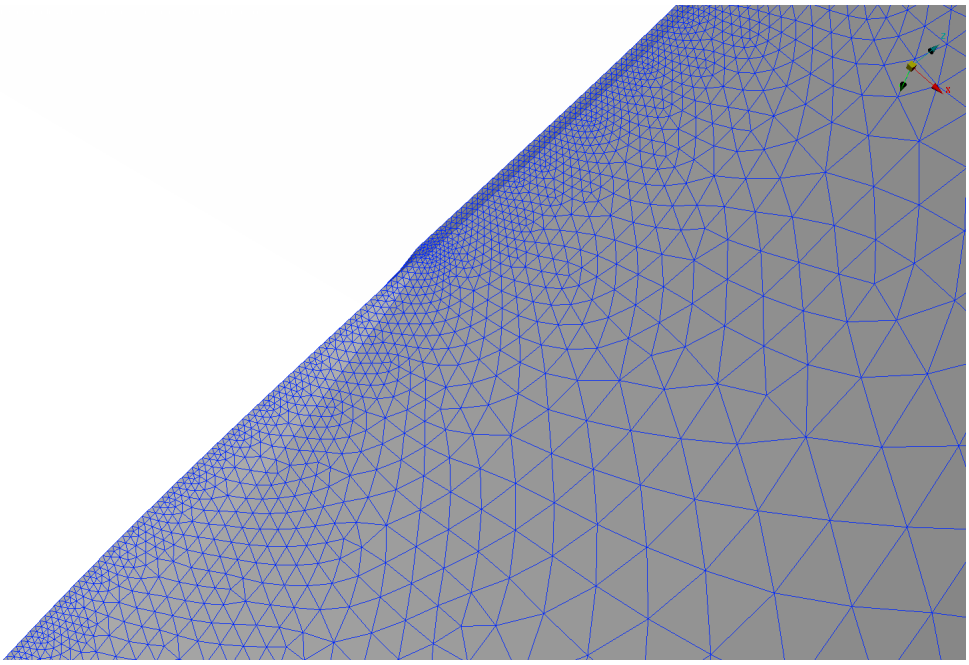

(d) Trailing edge of the blade.

Figure B.1: Blade geometry and its mesh.

Mesh quality	**min [mm]**	**max [mm]**
Fine regions	$0.027\% \cdot D_P \approx 0.75$	$0.060\% \cdot D_P \approx 1.62$
Coarse regions	$0.060\% \cdot D_P \approx 1.62$	$0.920\% \cdot D_P \approx 24.84$

Table B.1: Minimum and maximum cell size at the blades.

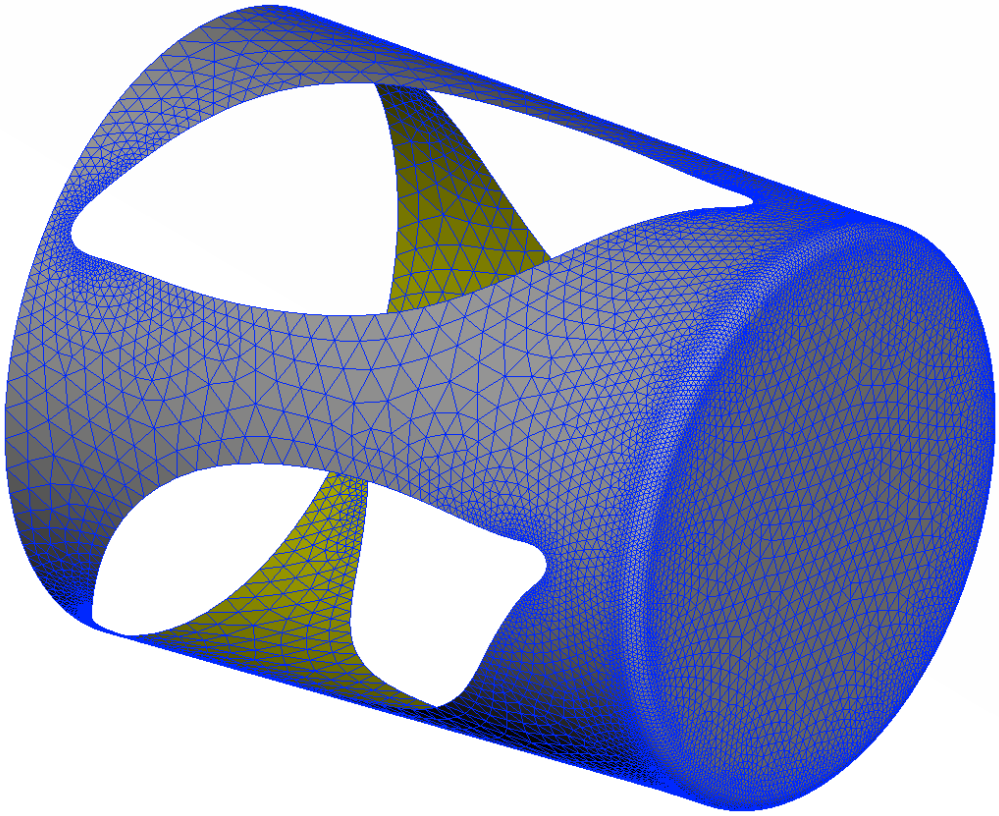

Figure B.2: Hub geometry and its mesh: Isometric view of the hub.

Mesh quality	**min [mm]**	**max [mm]**
Fine regions	$0.140\% \cdot D_P \approx 3.80$	$0.260\% \cdot D_P \approx 7.02$
Coarse regions	$0.260\% \cdot D_P \approx 7.02$	$0.850\% \cdot D_P \approx 22.95$

Table B.2: Minimum and maximum cell size at the hub.

Here it should be mentioned that the domain of the rotating geometries, also known as rotor, is the inner volume that is rotating within the outer volume (i.e. the outer domain). Thus, this configuration is a SMI configuration. The outer boundaries of the rotor are the interfaces (i.e. inlet and outer interface) and a surface attached to the inner part of the nozzle. An Arbitrary Mesh Interpolation (AMI) takes place between the rotor and the outer volume.

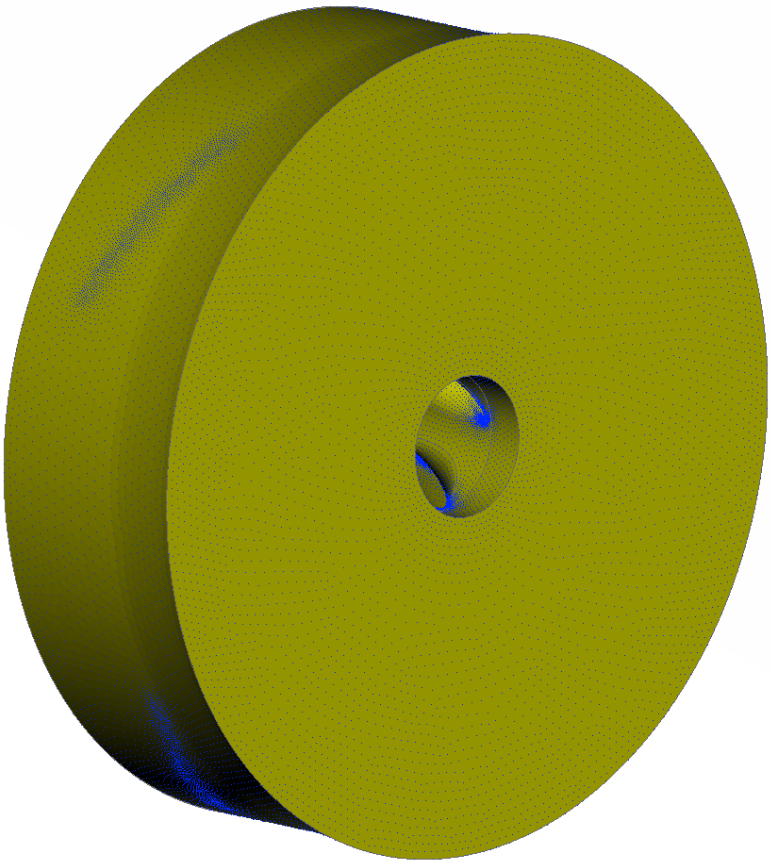

(a) Isometric view of the rotor.

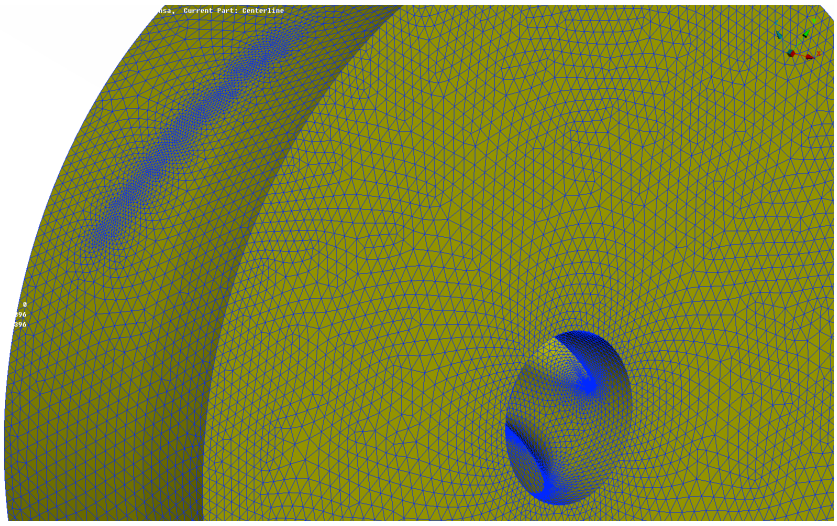

(b) Rotor including the surface attached to the inner part of the nozzle.

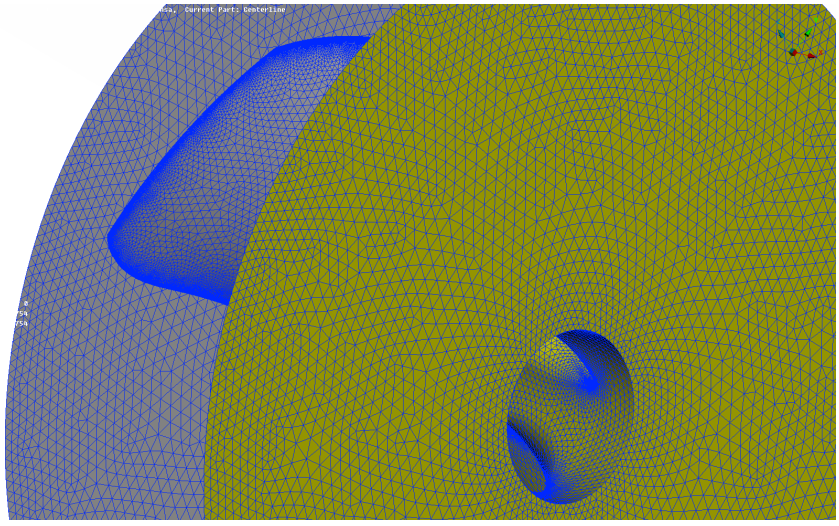

(c) Rotor excluding the surface attached to the inner part of the nozzle.

Figure B.3: Rotor geometry and its mesh.

Mesh quality	**min [mm]**	**max [mm]**
Fine regions	$0.400\% \cdot D_P \approx 10.80$	$1.400\% \cdot D_P \approx 37.80$
Coarse regions	$1.400\% \cdot D_P \approx 37.80$	$1.400\% \cdot D_P \approx 37.80$

Table B.3: Minimum and maximum cell size at the rotor.

B.2 Mesh grids used in Case 1

Here it should be mentioned that part of the inner part of the nozzle (see *Figure B.3a*) is geometrically identical with the surface of the rotor that is attached to the inner part of the nozzle (see *Figure B.4a*). Thus, almost identical mesh is attempted to be achieved. Moreover, this part of the inner part of the nozzle as well as the surface of the rotor that is attached to the inner part of the nozzle are including some refined regions. These refined regions occur at the regions where the tip of the blades is placed.

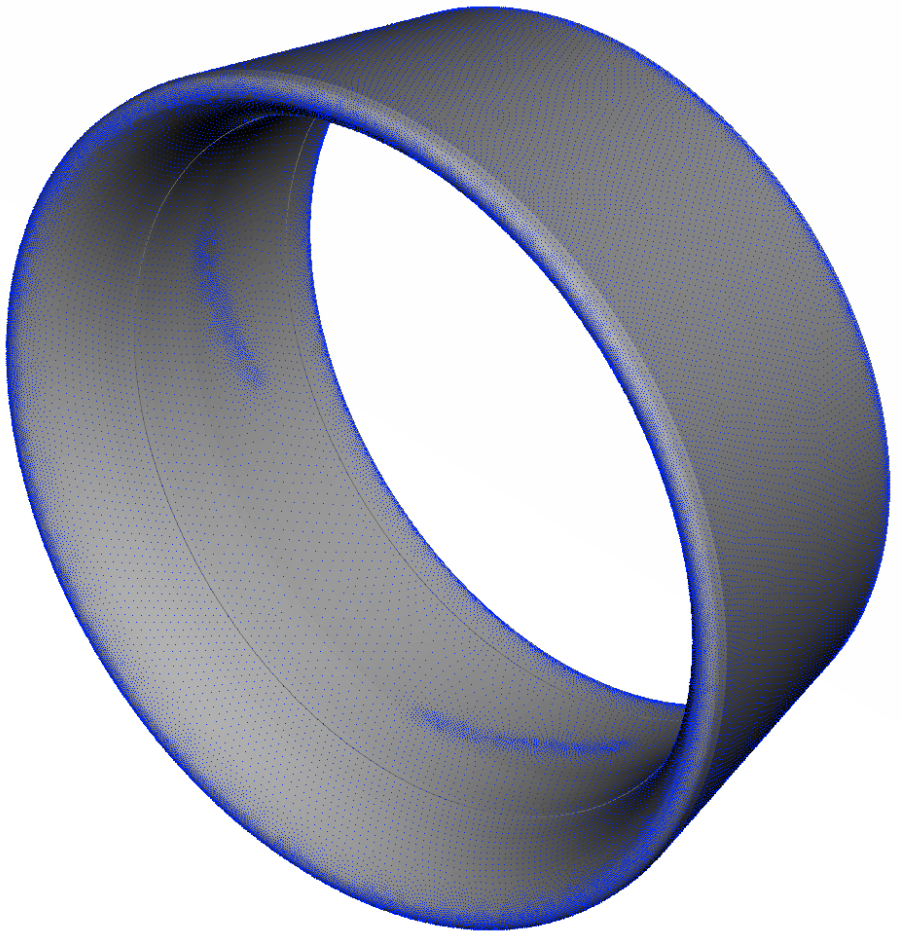

(a) Isometric view of the nozzle.

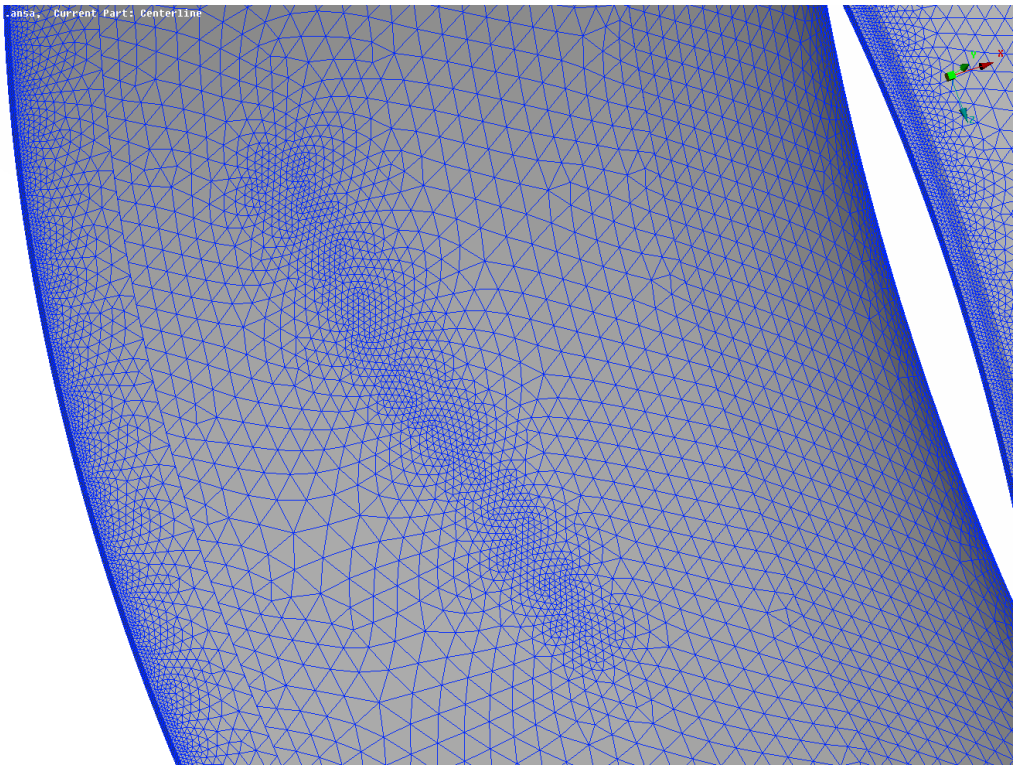

(b) Inner side of the nozzle, focusing on the refined mesh of the inner part of the nozzle.

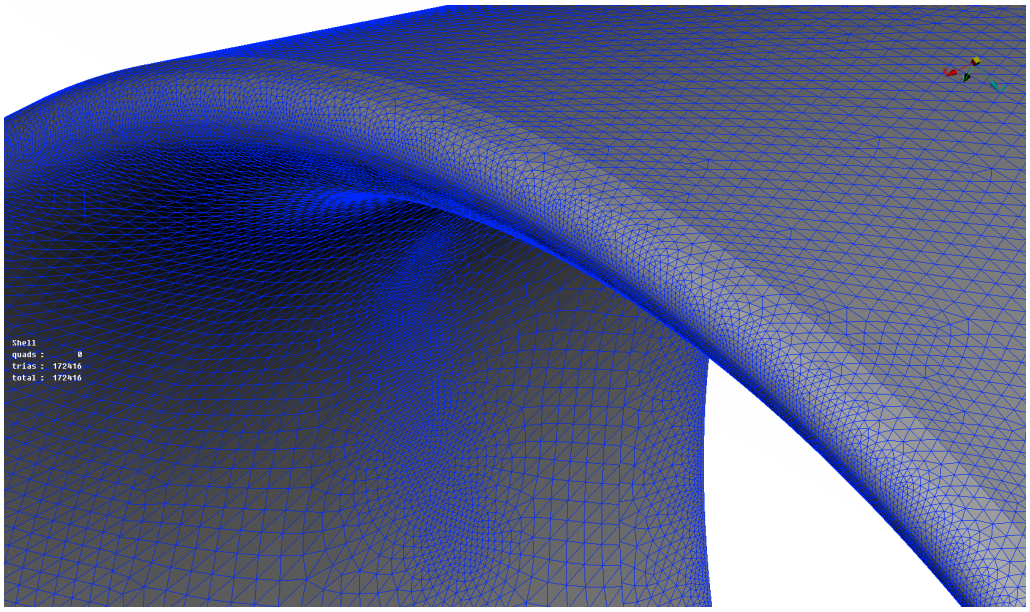

(c) Leading edge of the nozzle.

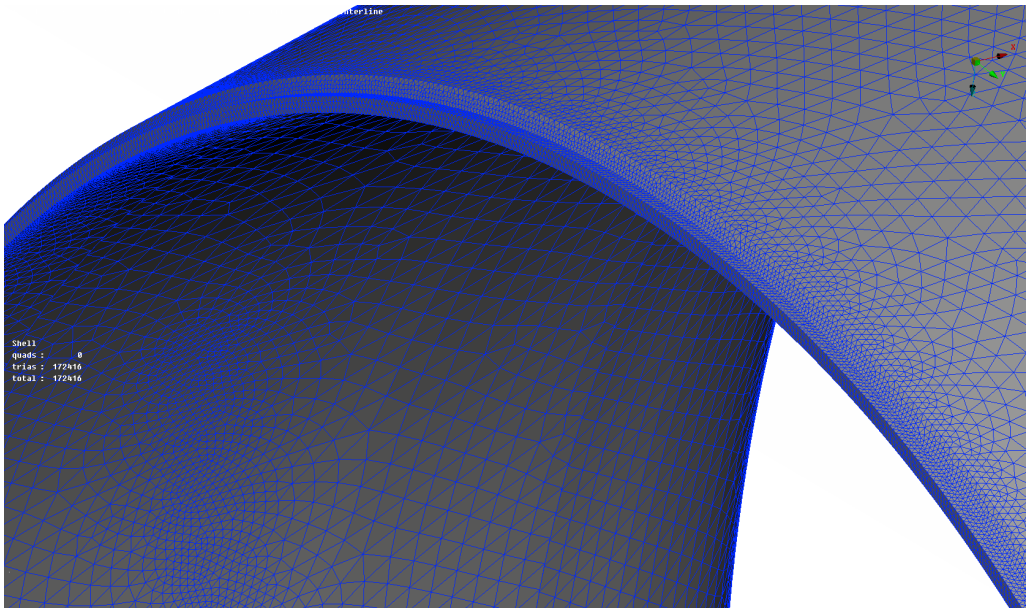

(d) Trailing edge of the nozzle.

Figure B.4: Nozzle geometry and its mesh.

Mesh quality	**min [mm]**	**max [mm]**
Fine regions	$0.240\% \cdot D_P \approx 6.48$	$0.670\% \cdot D_P \approx 18.09$
Coarse regions	$0.670\% \cdot D_P \approx 18.09$	$1.340\% \cdot D_P \approx 36.18$

Table B.4: Minimum and maximum cell size at the nozzle.

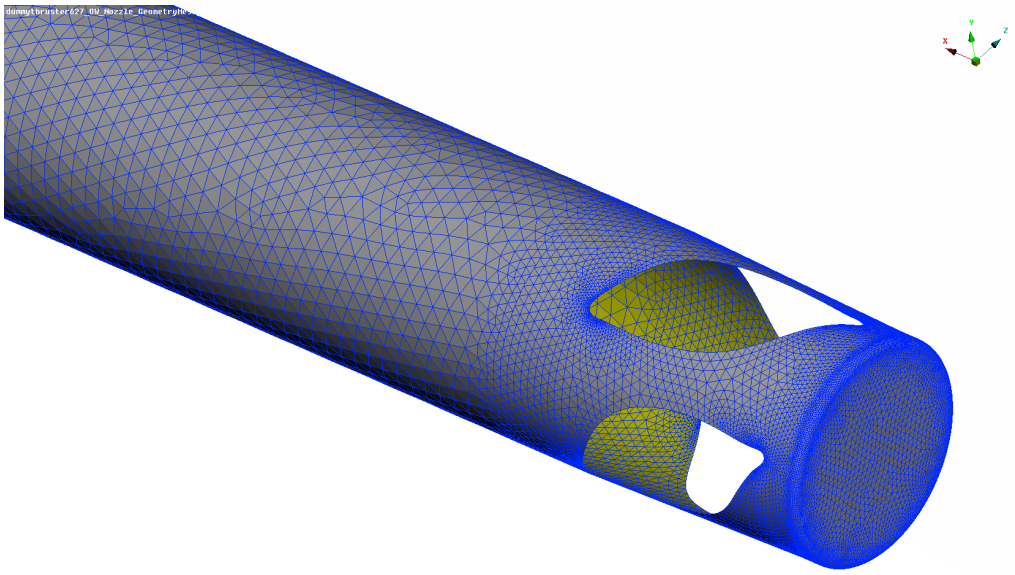

Figure B.5: Shaft-hub geometries and their mesh: Isometric view of the shaft including the hub.

Mesh quality	**min [mm]**	**max [mm]**
Fine regions	$0.690\% \cdot D_P \approx 18.63$	$0.670\% \cdot D_P \approx 18.09$
Coarse regions	$0.670\% \cdot D_P \approx 18.09$	$1.375\% \cdot D_P \approx 37.13$

Table B.5: Minimum and maximum cell size at the shaft.

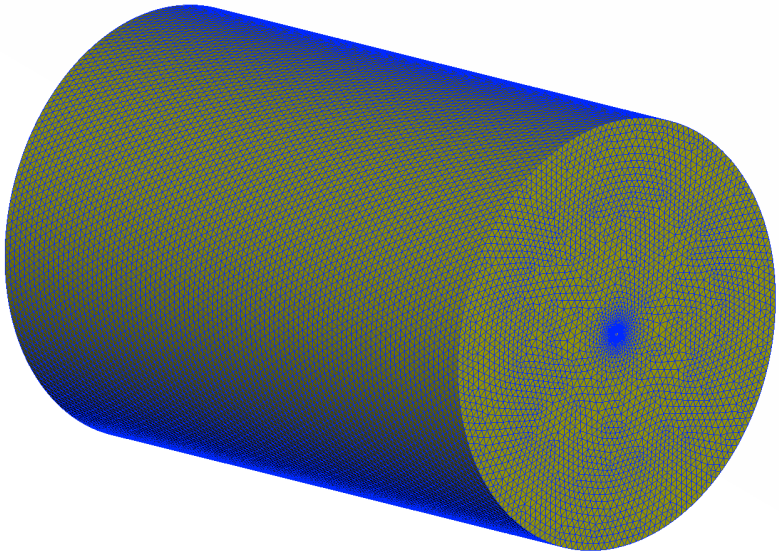

(a) Isometric view of the domain.

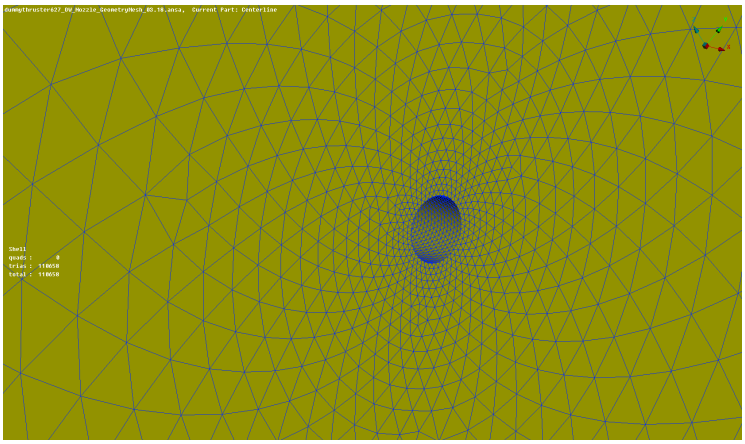

(b) Inlet of the domain including the connection region to the shaft.

Figure B.6: Domain geometry and its mesh.

Mesh quality	**min [mm]**	**max [mm]**
Fine regions	$1.400\% \cdot D_P \approx 37.80$	$38.000\% \cdot D_P \approx 1000$
Coarse regions	$38.000\% \cdot D_P \approx 1000$	$38.000\% \cdot D_P \approx 1000$

Table B.6: Minimum and maximum cell size at the domain.

B.3 Mesh grids used in Case 2

The azimuth unit excluding the blades is presented below. On the top of the gear case housing, a lid has been used during the simulations of Case 2 while in Case 3 the gear case housing is connected directly to the hull.

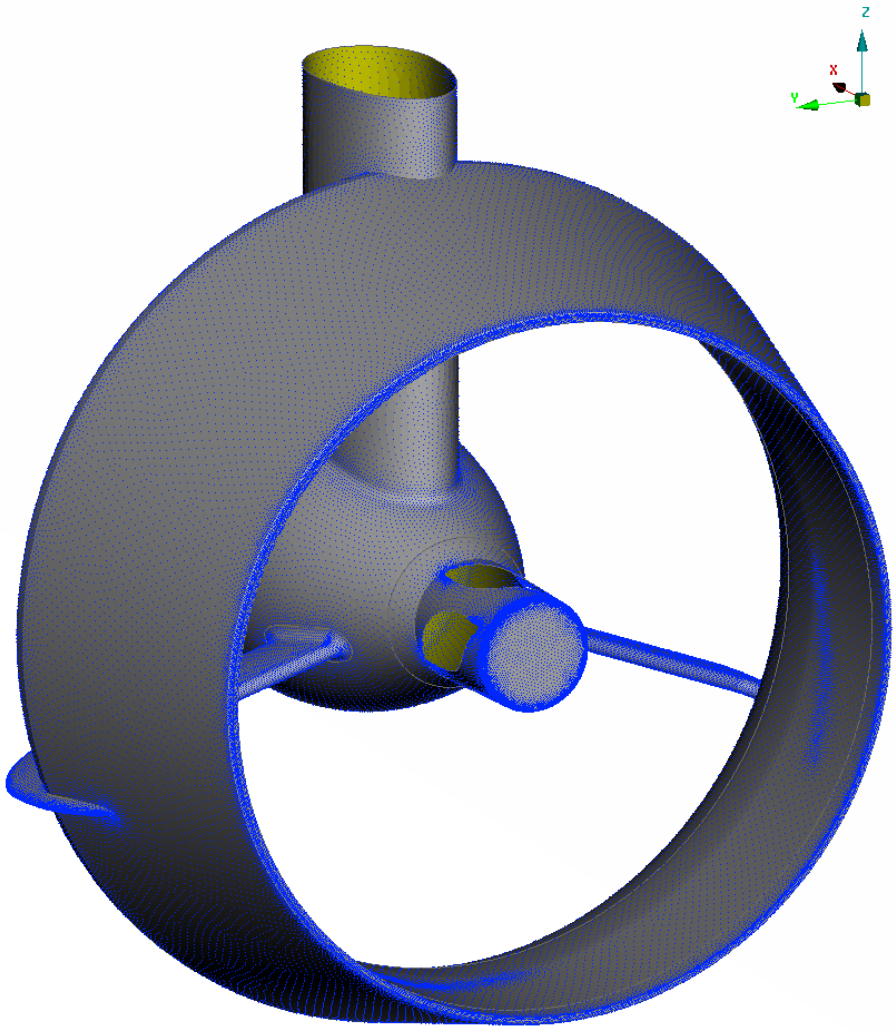

(a) Isometric view of the azimuth unit excluding the blades.

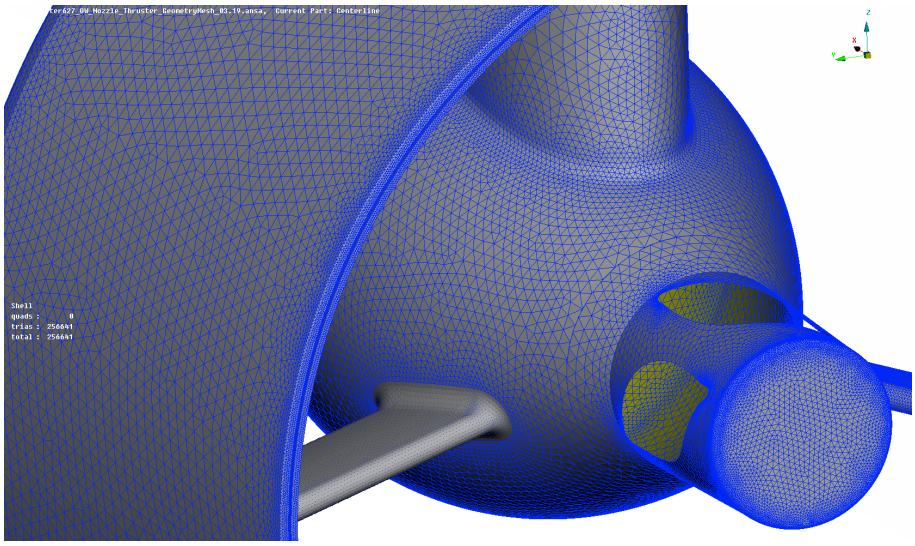

(b) Pressure side of the azimuth unit excluding the blades.

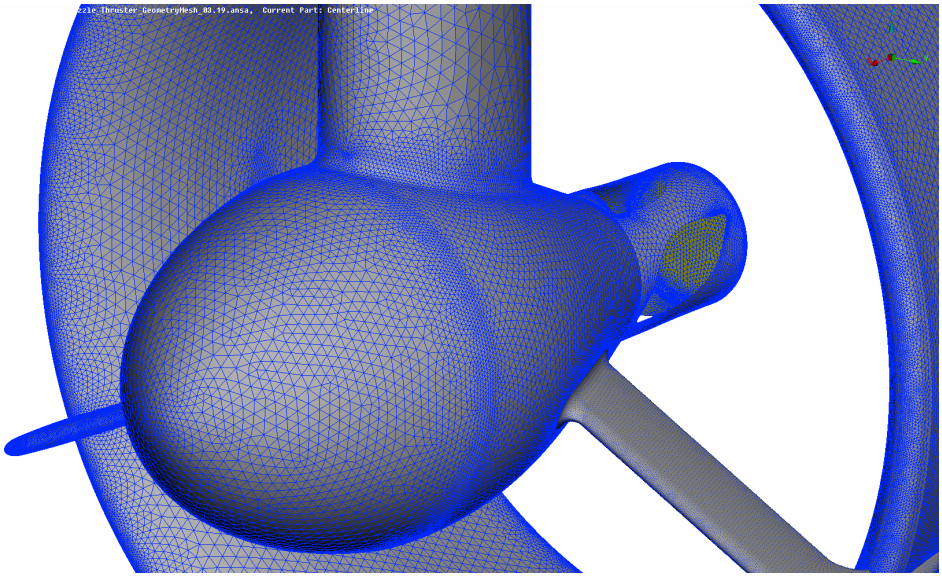

(c) Suction side of the azimuth unit excluding the blades.

Figure B.7: Azimuth unit geometry and its mesh.

Mesh quality	**min [mm]**	**max [mm]**
Fine regions	$0.300\% \cdot D_P \approx 8.10$	$0.5200\% \cdot D_P \approx 14.04$
Coarse regions	$0.5200\% \cdot D_P \approx 14.04$	$2.540\% \cdot D_P \approx 68.58$

Table B.7: Minimum and maximum cell size at the gear case housing.

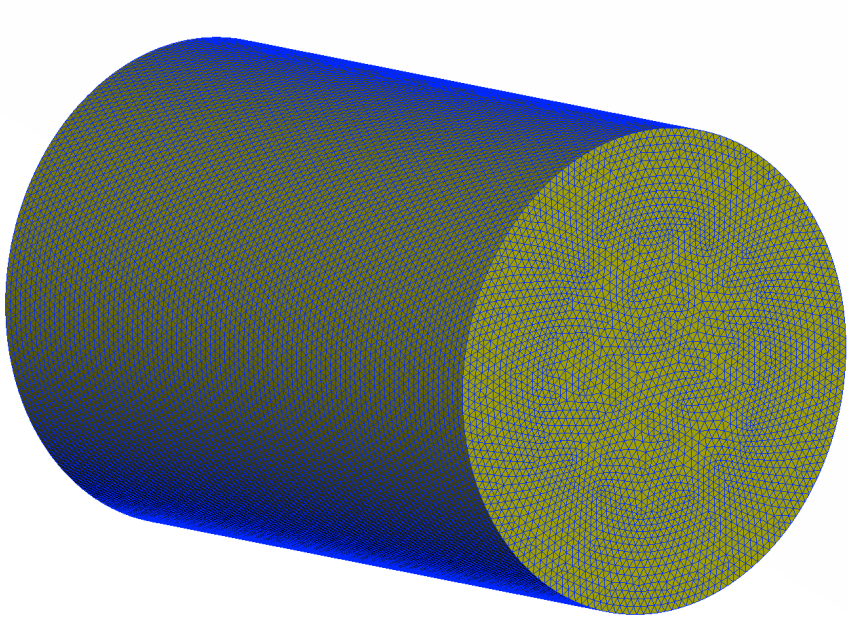

Figure B.8: Domain geometry and its mesh: Isometric view of the domain.

Mesh quality	**min [mm]**	**max [mm]**
Fine regions	$38.000\% \cdot D_P \approx 1000$	$38.000\% \cdot D_P \approx 1000$
Coarse regions	$38.000\% \cdot D_P \approx 1000$	$38.000\% \cdot D_P \approx 1000$

Table B.8: Minimum and maximum cell size at the domain.

B.4 Mesh grids used in Case 3

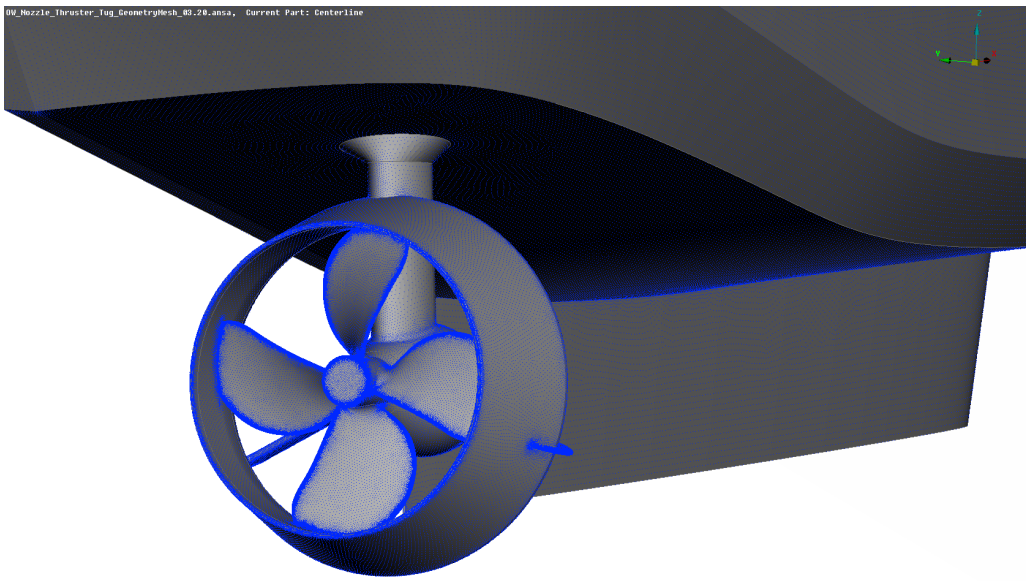

Figure B.9: Hull-azimuth geometries and their mesh: Isometric view of the hull including the azimuth unit.

Mesh quality	min [mm]	max [mm]
Fine regions	$0.370\% \cdot D_P \approx 10$	$2.320\% \cdot D_P \approx 62.64$
Coarse regions	$2.320\% \cdot D_P \approx 62.64$	$2.320\% \cdot D_P \approx 62.64$

Table B.9: Minimum and maximum cell size at the hull.

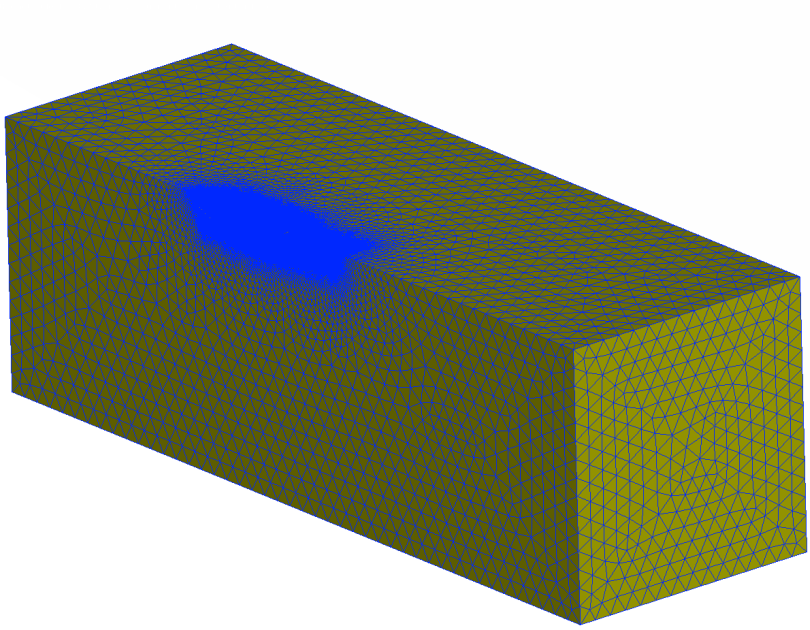

(a) Isometric view of the domain.

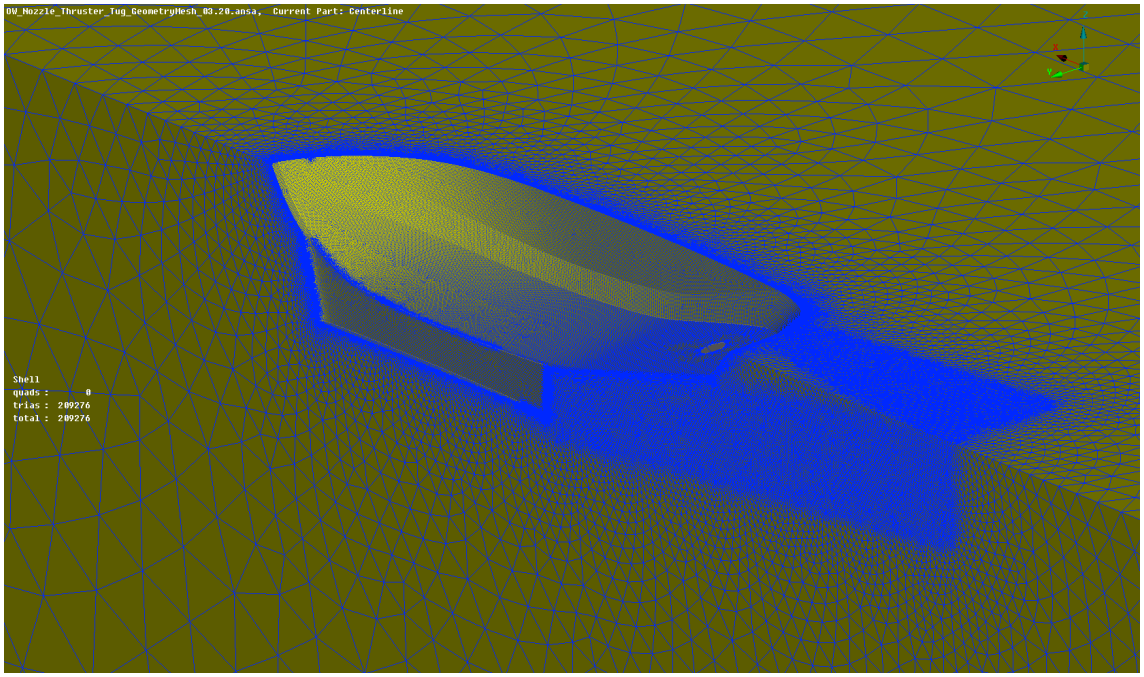

(b) Part of the domain, focusing on the refined mesh of the hull and the wake field behind it.

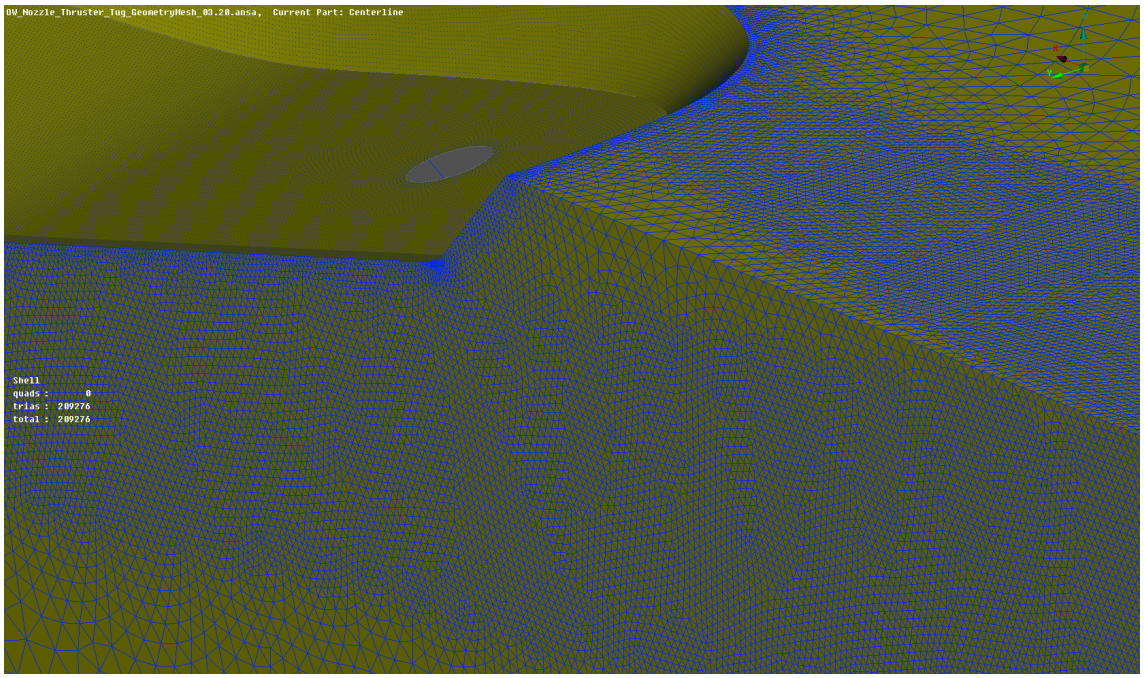

(c) Part of the domain, focusing on the refined mesh of the wake field behind the hull.

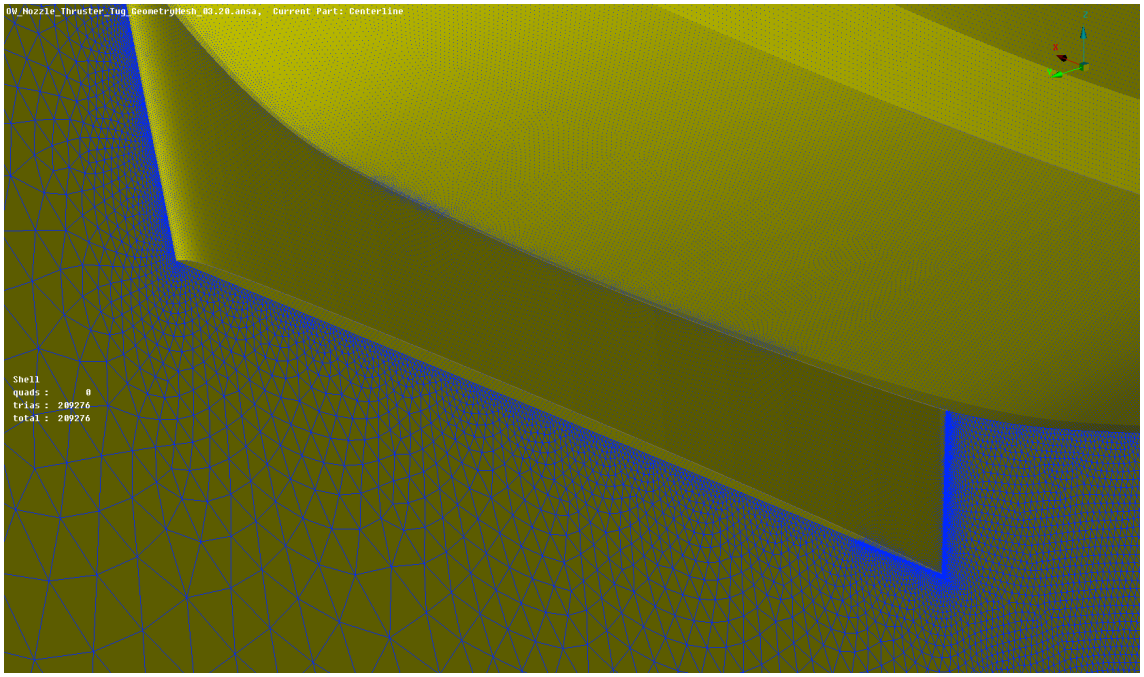

(d) Part of the domain, focusing on the refined mesh of the skeg of the hull.

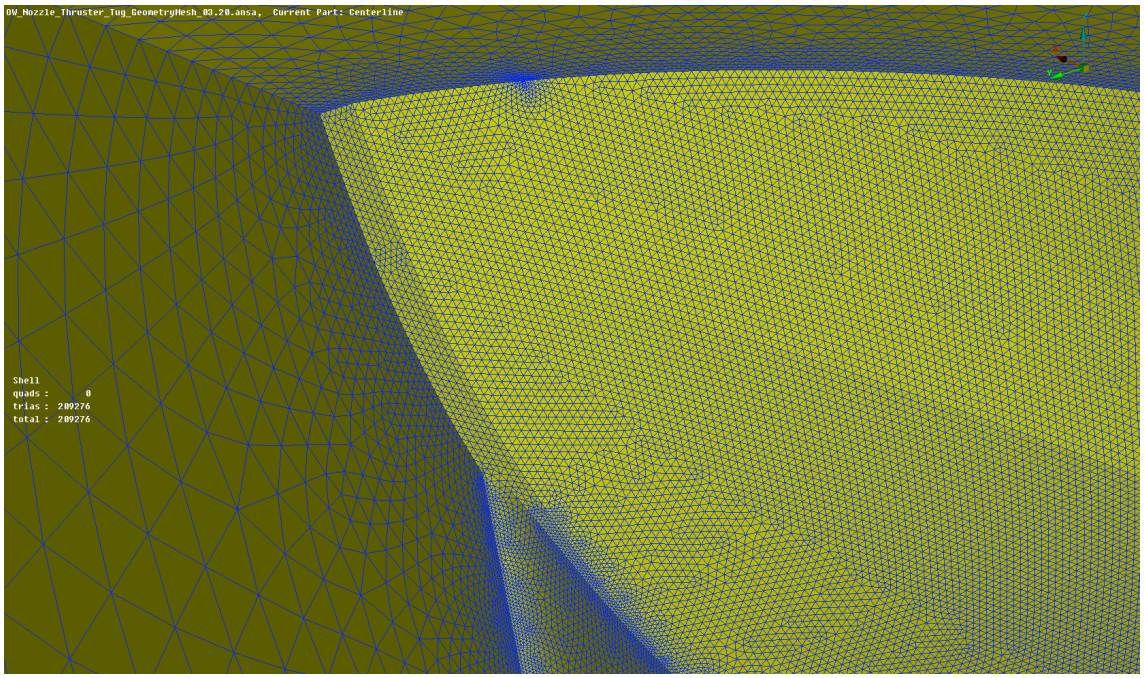

(e) Part of the domain, focusing on the refined mesh of the bow of the hull.

Figure B.10: Domain geometry and its mesh.

Mesh quality	**min [mm]**	**max [mm]**
Fine regions	$2.320\% \cdot D_P \approx 62.64$	$124.000\% \cdot D_P \approx 3348.00$
Coarse regions	$124.000\% \cdot D_P \approx 3348.00$	$124.000\% \cdot D_P \approx 3348.00$

Table B.10: Minimum and maximum cell size at the domain.